

UC Irvine

UC Irvine Electronic Theses and Dissertations

Title

Engineering Transport through Biological and Synthetic Nanopores

Permalink

<https://escholarship.org/uc/item/5p43x1bd>

Author

Buchsbaum, Steven

Publication Date

2016

Peer reviewed|Thesis/dissertation

UNIVERSITY OF CALIFORNIA,
IRVINE

Engineering Transport through Biological and Synthetic Nanopores

DISSERTATION

submitted in partial satisfaction of the requirements
for the degree of

DOCTOR OF PHILOSOPHY

in Physics

By

Steven F. Buchsbaum

Dissertation Committee:
Professor Zuzanna S. Siwy, Chair
Professor Thorsten Ritz
Professor Michael Dennin

2016

Portions of Chapter 3 adapted from ref [1]: © 2013, American Chemical Society
Portions of Chapter 4 adapted from ref [2]: © 2014, American Chemical Society
All other materials: © 2016 Steven F. Buchsbaum

Dedication

To my incredible family, friends and teachers

Table of Contents

List of Figures	vi
List of Tables	viii
Acknowledgements	ix
Curriculum Vitae	xii
Abstract of the Dissertation	xvii
Chapter 1: Nanopores in Nature and the Lab.....	1
Chapter 2: Theoretical Background.....	6
2.1 Nanopore Transport Theory.....	6
2.1.1 Charged Surfaces and the Debye Length.....	6
2.1.2 Nanopore Transport Physics	10
2.2 Electrochemical Setup.....	16
2.2.1 Silver/Silver Chloride Electrodes.....	16
2.2.2 Electrochemical Cell	17
2.3 Coulter Counter	19
2.3.1 The Resistive Pulse Technique.....	19
2.4 DNA Basics	22
2.1.1 Description of DNA	22
Chapter 3: Steric and Electrostatic Effects in Nanopore Translocation	24
3.1 Introduction.....	24
3.2 Theory and Background.....	26
3.2.1 DNA Translocation through α -hemolysin.....	26
3.2.2 Applications of the Coulter Counter Technique	28
3.2.3 DNA Sequencing using Nanopores	30
3.2.4 Statistical Analysis of Translocation Events	32
3.2.5 The Becquerel Function.....	33
3.2.6 Formalism of First Passage time for a Stochastic Polymer	34
3.3 Experimental Setup	37
3.3.1 Nanopore Recordings	37

3.3.2 Peptide-DNA Molecule Preparation.....	38
3.3.3 Molecular Modeling.....	39
3.3.4 Data Analysis.....	41
3.4 Results and Discussion.....	43
3.4.1 Modeling DNA-Peptide Molecules	43
3.4.2 Verification of DNA-Peptide Modification	44
3.4.3 Peptide Modified DNA Translocation Produces Closure Events.....	47
3.4.4 Trends in Translocation Time	49
3.4.5 Formulation of a Biophysical Model	52
3.4.6 Disentangling Steric and Electrostatic Factors	56
3.5 Conclusion	59
Chapter 4: Making Nanopore Gates from Polymer Pores and DNA	61
4.1 Introduction.....	61
4.2 Theory.....	64
4.2.1 Track Etch Technique	64
4.2.2 PET Surface Chemistry.....	69
4.2.3 Characterization of Nanopores	70
4.2.4 Rectification in Conical Nanopores	72
4.2.5 Charge Distribution of DNA.....	74
4.2.6 DNA Confirmations in Solution.....	75
4.2.7 Concentration Profile in a Conical Nanopore	77
4.3 Experimental Setup.....	78
4.3.1 PET Pore Fabrication	78
4.3.2 Conical PET Pore Characterization.....	80
4.3.3 Modifying Pores with ssDNA	80
4.3.4 Data Acquisition and Analysis.....	81
4.4 Results and Discussion.....	81
4.4.1 Competing Steric and Electrostatic Effects from DNA Modification	81
4.4.2 Nano-mechanical Voltage Dependent Gating.....	84
4.4.3 pH Dependent Gating through DNA Mesh Formation.....	87
4.4.4 Switching of the Rectification Direction.....	92
4.4.5 Reversibility of closure	93
4.5 Conclusion	94
Chapter 5: Unraveling Nanofluidic Phenomena in Individual CNTs.....	97
5.1 Introduction.....	97

5.2 Theory	100
5.2.1 Structure of a CNT	100
5.2.2 Electronic Characteristics of CNTs	102
5.2.3 Enhanced Flow in CNTs	103
5.2.4 Limitations of the Continuum Models in CNTs	105
5.3 Experimental Setup	107
5.3.1 Device Fabrication	107
5.3.2 CNT Growth	109
5.3.3 CNT Characterization.....	110
5.3.4 Leak Testing	110
5.3.5 Data Acquisition and Analysis	111
5.3.6 Molecular Simulations.....	112
5.4 Results and Discussion	113
5.4.1 Demonstration of a Successful Device.....	113
.....	116
5.4.2 Ionic Transport in a CNT	117
5.4.3 Evidence of Electroosmotic Flow	120
5.4.4 Simulation Suggests Origin of Electroosmotic Flow.....	123
5.4.5 Interpretations of a Work in Progress	124
5.5 Conclusion	125
Chapter 6: The Future of Nanopore Research	127
Bibliography	130

List of Figures

Figure 1.1 Alpha-hemolysin in a lipid bilayer	2
Figure 1.2 Sodium ion channels	3
Figure 1.3 Synthetic nanopores.....	4
Figure 2.1.1 Electrical double layer	10
Figure 2.1.2 PNP calculation	15
Figure 2.2.1 Electrochemical cell	17
Figure 2.2.2 Electrical model of a cell.....	18
Figure 2.3.1 Resistive pulse	19
Figure 2.4.1 DNA structure.....	22
Figure 3.2.1 Pulling proteins through α -hemolysin	27
Figure 3.2.2 Diameter of ssDNA	29
Figure 3.2.3 DNA sequencing	31
Figure 3.3.1 DNA-peptide coupling.....	38
Figure 3.3.2 Survival function	42
Figure 3.4.1 MD snapshots	43
Figure 3.4.2 HPLC traces	45
Figure 3.4.3 Event traces.....	47
Figure 3.4.4 τ^* vs voltage	51
Figure 3.4.5 Biophysical Model.....	53
Figure 4.1.1 Polymer brushes	62
Figure 4.1.2 DNA gate.....	63
Figure 4.2.1 Thermal spike model.....	65
Figure 4.2.2 Ionization spike model.....	66
Figure 4.2.3 PET pore etching.....	68
Figure 4.2.4 EDC chemistry	70
Figure 4.2.5 Pore sizing	71
Figure 4.2.6 Ionic diodes	73
Figure 4.2.7 ssDNA length	76
Figure 4.2.8 Diffusion through a conical pore.....	78
Figure 4.3.1 GSI beamline	79
Figure 4.4.1 AC-rich modified pore.....	81
Figure 4.4.2 DNA in different size pores	83
Figure 4.4.3 Voltage response vs pore size	84
Figure 4.4.4 Hysteresis from DNA conformations	86
Figure 4.4.5 Formation of electrostatic mesh	87
Figure 4.4.6 Summary of pH gating data.....	88
Figure 4.4.7 pH dependent I-V curves	89
Figure 4.4.8 All base I-V curves	90
Figure 4.4.9 Base side modificaton	91
Figure 4.4.10 Switching rectification direction.....	92
Figure 4.4.11 Reversible closure.....	94
Figure 5.1.1 Horizontal single CNT device	98
Figure 5.2.1 Structure of a CNT	101

Figure 5.2.2 Multi walled CNT	102
Figure 5.2.3 MD simulation inside a CNT.....	106
Figure 5.3.1 CNT Device Fabrication.....	108
Figure 5.3.2 PDMS electrochemical cell	111
Figure 5.4.1 CNT device characterization.....	114
Figure 5.4.2 Translocation through a CNT	116
Figure 5.4.3 Conductance vs pH	117
Figure 5.4.4 Conductance vs KCl concentration.....	119
Figure 5.4.5 Electroosmotic flow	122
Figure 5.4.6 MD simulations of KCl in a CNT.....	123

List of Tables

Table 3.3.1 Number of translocation events	37
Table 3.4.1 HPLC and MS Summary	46
Table 3.4.2 Blockade amplitude	48
Table 3.4.3 Fit parameters.....	58

Acknowledgements

This thesis and the work it represents were only made possible through a huge amount of support from a lot of different people and I consider myself amazingly lucky to have had it.

I want start by thanking Dr. Zuzanna Siwy. She has been a truly fantastic mentor and the successes I have had are in large part thanks to her. When I was first looking for a lab to join, I knew immediately after meeting with Zuzanna and talking to her students that she would be a great advisor. When it comes to teaching, she is encouraging and patient while still allowing the freedom required to grow. In the event of unexpected problems or challenges she was, without exception, willing to set aside time and help in any way she could. It was clear from the start that Zuzanna has the best interests of her students at heart and does everything she can to help them succeed. My time in graduate school has made it clear that a research advisor is the cornerstone of the entire experience and to have Zuzanna play that part for me, I am grateful.

I also want to thank both Dr. Thorsten Ritz and Dr. Michael Dennin. They were excellent committee members and provided me with valuable guidance along the way. They were both genuinely interested in helping me improve my research and were willing to devote their time towards reviewing and discussing it with me. As a result of these discussions both my personal knowledge and research projects have benefited.

Throughout my day to day life at UCI, I have spent a great deal of time in the lab, all of which was made so much better by the amazing coworkers and friends around me. Trevor Gamble, Gael Nguyen, Matt Pevarnik, Matt Davenport, Laura Innes, Matt Schiel, Tim Plett,

Crystal Yang, Justin Menestrina, Preston Hinkle, Yinghua Qiu and Willian Mann are all students who I have had the opportunity to get to know and work with in the Siwy Lab over the years. When I have needed help with problems based in science or otherwise they have always been there for me. Even though some of the previous students in the Siwy Lab were gone before I arrived, their contributions are seen almost everywhere I look. Matt Powell, Ken Kealy, Eric Kalman and Ivan Vlassiousk are all previous members that played instrumental roles in setting up the lab and were always willing to answer questions I had and give useful advice. I also want to thank a few other friends who were not a part of my research lab, but were a significant part of my time in graduate school. Max Wiedmann, Dan Carson, Calvin Patel, Tim Ma, Matt Weiss, Emon Heidari and Greg Zicarelli all made my time at UCI infinitely better and I do not believe I would still be here if it were not for them. They were there to help when things were tough, such as the first year of classes, and have given me a near endless list of good memories since.

Next, I want to thank Dr. Francesco Fornasiero. Starting about a year and a half ago, I was given the opportunity to move to northern California and conduct my research at Lawrence Livermore National Lab. This grew out of a collaboration between Zuzanna and Francesco in which I am very grateful to have been included. Francesco has played the role of mentor during my time at LLNL and has done an excellent job. He is one the most genuine, and thoughtful people I know and was instrumental in helping me make the transition from UCI to LLNL. Francesco is also a uniquely gifted scientist that I have learned a great deal from. We have had countless scientific discussions during which he is always positive and willing to elaborate on anything I might have missed. I look forward to continuing my work with Francesco during my postdoctoral appointment at LLNL.

My time at LLNL was also greatly influenced by the lab members and friends I worked with there on a daily basis. Shirui Guo, in particular has spent a tremendous amount of time helping and teaching me over the last year and a half and for that I am grateful. I would not be in a position to carry on my current project if it were not for him. I also want to thank Eric Meshot, Ngoc Bui and Sangil Kim for the many conversations from which I have learned so much and for making me feel welcome and at home in Livermore.

Next, I want to recognize the help I have received from my family and loved ones. First I want to thank my parents and my sister who have provided me with all of the support and encouragement I could ever ask for - I am very lucky to have them. Second, I am very appreciative of my extended family who have been there, in person or on the phone, to support me at many of the important milestones towards graduation. I also want to say a special thank you to Amy Vo. She has been an unwavering source of support and encouragement and has helped me, maybe more than she knows, arrive at where I am now.

Finally, I want to say thank you to the University of California, Irvine, Lawrence Livermore National Lab and to all of my funding sources, which have made it possible for me to perform the work that is presented in this thesis.

Curriculum Vitae

Steven F. Buchsbaum

Contact Information

Building 3649, Room 1014

Biosecurity and Bionanoscience Group

Lawrence Livermore National Laboratory

Livermore, CA 94550

Voice (office): (925) 424-2161

Voice (cell): (208) 921-7689

E-mail: sfbuchsbaum@gmail.com

Website: <http://www.physics.uci.edu/~zsiwy> and <http://bbn.llnl.gov/node/119.html>

Education

University of California, Irvine, Department of Physics and Astronomy:

Ph.D., Physics, January 2016

- Advisor: Dr. Zuzanna Siwy
- Advanced to Candidacy May 2013

M.S., Physics, March 2012

University of California, Santa Barbara, College of Creative Studies:

B.S., Physics, June 2010

Honors and Awards

Livermore Graduate Scholar Fellowship, LLNL, August 2014

Regents Fellowship, UCI, August 2010

Distinction in the Major, UCSB, May 2010

Research Honors Award, UCSB, May 2010

Student Undergraduate Research Fellowship, UCSB, June 2009

Academic Experience

Lawrence Livermore National Laboratory:

Livermore Graduate Scholar (August 2014 – present)

- Mentor: Dr. Francesco Fornasiero

University of California, Irvine:

Graduate Student Researcher (August 2011 – present)

Graduate Student (September 2010 – present)

Teaching Assistant September (2010 - December 2011)

University of California, Santa Barbara:

Undergraduate Student Researcher (March 2007 - December 2009)

Publications

- 1) Pham, T. A., Mortuza, S. M., Wood, B. C., Lau, E. Y., Ogitsu, T., **Buchsbaum, S. F.**, et al. (in preparation). "Salt Solutions in Carbon Nanotubes: The Role of Cation- π Interactions." *Journal of Physical Chemistry Letters*
- 2) Kuo, C., Li, Y., Nguyen, D., **Buchsbaum, S. F.**, et al. (2015). "Macroscopic Strain Controlled Ion Current in an Elastomeric Microchannel." *Journal of Applied Physics* 117: 174904.
- 3) Innes, L., Gutierrez, D., Mann, W., **Buchsbaum, S. F.**, et al. (2015). "Presence of Electrolyte Promotes Wetting and Hydrophobic Gating in Nanopores with Residual Surface Charges." *Analyst* 140: 4804-4812.
- 4) **Buchsbaum, S. F.**, et al. (2014). "DNA-Modified Polymer Pores Allow pH and Voltage-Gated Control of Channel Flux." *Journal of the American Chemical Society* 136(28): 9902-9905.
- 5) **Buchsbaum, S. F.**, et al. (2013). "Disentangling Steric and Electrostatic Factors in Nanoscale Transport Through Confined Space." *Nano Letters* 13(8): 3890-3896.
- 6) Ferguson, B. S., **Buchsbaum, S. F.**, et al. (2011). "Genetic Analysis of H1N1 Influenza Virus from Throat Swab Samples in a Microfluidic System for Point-of-Care Diagnostics." *Journal of the American Chemical Society* 133(23): 9129-9135.

- 7) **Buchsbaum, S. F.** (2010). "Integrated Microfluidic Platforms Toward Point of Care Pathogenic Nucleic Acid Detection." Honors Undergraduate Research Thesis, Department of Physics, University of California, Santa Barbara.
- 8) Ferguson, B. S., **Buchsbaum, S. F.**, et al. (2009). "Integrated Microfluidic Electrochemical DNA Sensor." Analytical Chemistry 81(15): 6503-6508.

Research Skills

Cleanroom experience with fabrication of nano and micro scale devices including:

- Photolithography
- Chemical vapor deposition (LPCVD, PECVD)
- Physical vapor deposition (sputter coating)
- Reactive ion etching
- Membrane stress testing

Carbon nanotube growth and characterization including:

- CNT growth using CVD techniques
- Characterization using Raman spectroscopy and SEM

Contact angle measurement tool use

Machine shop fundamentals

Spectroscopy experience including UV-Vis and fluorescence based techniques

Patch clamp amplifier operation

Computer Skills

Mathematica: Thorough understanding of programming using Mathematica.

National Instruments Lab View: Can code basic programs and interface with instruments.

Autodesk Inventor: Can create professional 2D or 3D CAD files.

Matlab: Can write intermediate level programs and perform data analysis.

Origin: Experienced with plotting and analyzing data in origin. L-Edit: Can create and design patterns used in photolithography masks.

Microsoft Office: Experienced with Excel, Word and PowerPoint.

Adobe Illustrator/Photoshop: Proficient in creating images and figures.

Adobe Dreamweaver: Proficient in using Dreamweaver/html code to create and maintain webpages.

Abstract of the Dissertation

Engineering Transport through Biological and Synthetic Nanopores

By

Steven F. Buchsbaum

Doctor of Philosophy in Physics

University of California, Irvine, 2016

Professor Zuzanna S. Siwy, Chair

Biological nanopores are an essential element to the success of the lipid bilayer that makes life possible on the cellular level. Protein based pores are responsible for the transport of specific ions and molecules across the bilayer and can accomplish their jobs with incredible variety. Some pores, such as those from bacteria have relatively simple structures and allow for many types of transport. Others, like those found in neurons have very high specificity as well as the ability to respond to different cues in the surrounding environment. The vast number of biological ion channels and their complex structures make it difficult to study and understand the nanofluidic phenomena they exhibit. Inspired by the pores seen in nature, scientists have begun to create their own synthetic versions which are usually simpler in structure. These man made pores have been fabricated through a variety of techniques and materials and provide well controlled systems capable of isolating and testing specific transport phenomena. Additionally, these pores provide the building blocks with which more complicated and truly biomimetic pores can be made.

In this thesis, three very different types of nanopores will be examined. First, an alpha hemolysin pore will be isolated and the physics governing transport time will be studied.

The diameter and charge of single stranded DNA molecule is modified before being electrophoretically driven through the pores inner constriction. These translocation events are monitored via current measurements across the pore and a biological model is formulated to explain the behavior. This work has the potential to improve DNA sequencing technologies which are dependent on slowing down DNA translocation speed for accurate reads. Next, a synthetic conical nanopore etched in a polymer film will be used as the foundation for a biomimetic nanopore gate. Through the attachment of ssDNA to the pore walls, a pH and voltage responsive nanochannel is created. This is done through the careful selection of the DNA sequence to contain protonatable nucleotides which enable the formation of a transport blocking mesh. Synthetic gated channels that can respond to multiple stimuli as well as have a robust and reversible closing mechanism have been historically difficult to design and are essential to advancing the nanopore field. Finally, a different type of synthetic nanochannel is made from the inner volume of a carbon nanotube. We present a platform that allows for the isolation and study of a single nanotube and use it to examine the underlying transport properties. Carbon nanotube based nanochannels show several unique behaviors which the current literature has not been able to completely explain. Several questions such as the magnitude and origin of enhanced flow and even what carries the current remain open, motivating additional studies, such as ours, which aim to help provide much needed answers.

Chapter 1: Nanopores in Nature and the Lab

Separating one thing from another is an essential concept to all types of life and across all size scales. Whether its keeping the cold from the inside of you home, pathogens from getting inside of your body, or keeping the nutrients inside a cell from being washed away, barriers need to be set up and maintained. The problem with such barriers is that they generally can't be absolute. They must allow for the passage of some things while still keeping the rest separate. Doors are needed to enter homes, sweat needs to be able to pass through the skin and cells need to be able to transmit signaling molecules and replenish their nutrients. When looking at micro and nano scale barriers, such as those used in cells, nature utilizes various types of nanopores in order to allow for controlled passage across such barriers.³

A nanopore, at the simplest level is a tiny hole spanning the width of a barrier. It serves as a selective pathway between the inside and outside of a biological entity. Perhaps the most important barrier in which nanopores exist is the cellular membrane. This membrane surrounds and protects an individual cell and is made from two layers of fatty acids. The core molecule of these membranes, the phospholipid, has a hydrophilic head attached to a hydrophobic tail. This causes them, when in an aqueous environment, to organize into two layers with the tails facing each other and the exposed heads facing outwards on both sides of the membrane.⁴

The pores which span these membranes are generally made from proteins that insert themselves into the cell bilayer. These proteins consist of very long chains of amino acids

that fold up into a three-dimensional hollow structure. Once in position, specific molecules are able to traverse the membrane by passing through the protein interior. Most of the simple nanopore proteins come from bacterial cells such as *E. coli* and *Staphylococcus*.⁵ Such pores are described this way because they tend to act as simple holes, allowing anything that can fit to travel through them. Alpha-hemolysin (α -hemolysin) is one such example and has been studied quite a bit in the lab.^{6,7} This particular protein is one reason *Staphylococcus aureus* is so dangerous as α -hemolysin will embed itself into human cell walls leading to cell death.^{8,9}

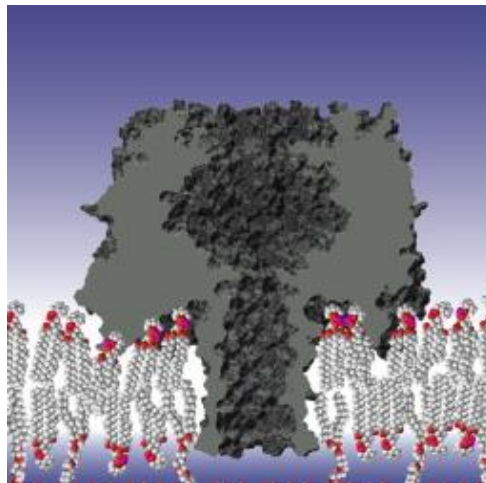


Figure 1.1 Alpha-hemolysin in a lipid bilayer. Supramolecular model of an alpha hemolysin pore inserted into a tethered bilayer membrane. Image taken with permission from Elsevier from McGillivray et al.⁷

Other protein-based nanopores, such as those found in mammals, show much higher levels of complexity. Through more complicated structures they can have abilities such as selectively passing molecules, changing transport properties in response to environmental cues, and actively pumping molecules against a concentration gradient. These types of nanopores are required for a huge host of cellular processes that are happening in humans all of the time. Examples include nucleic acid transfer, protein secretion, viral replication and nerve signaling.³ The last example in particular was one of the first biological

phenomena tied to the presence of nanopores. As early as 1949 Huxley and Hodgkin were able to observe, through applying a voltage across the cell membrane, the action potential in giant squid axons.¹⁰ As one possible explanation, they proposed some sort of selective ion channels through the membrane. This theory was later verified by Roderick MacKinnon who was able to isolate and image potassium ion channels using x-ray crystallography.¹¹

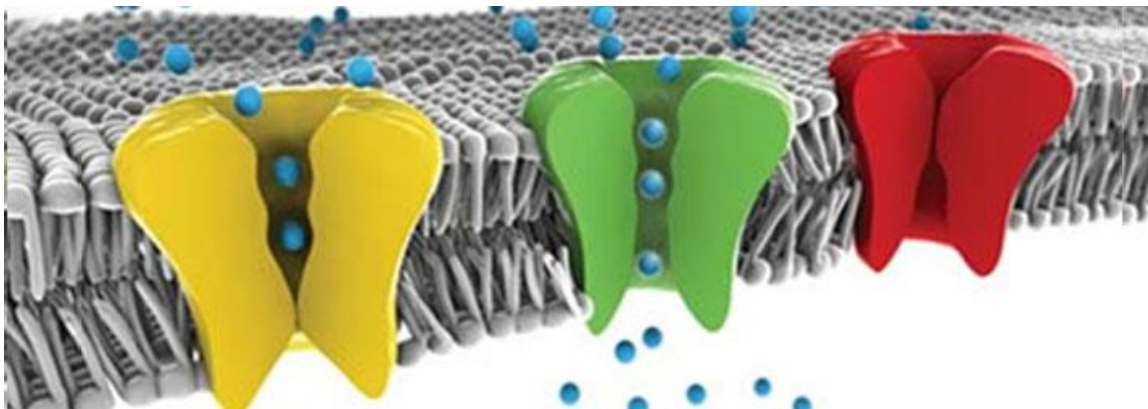


Figure 1.2 Sodium ion channels. An artist's depiction of sodium ion channels imbedded in a lipid bilayer. Channels are shown in both open and closed states. Taken from Rajakulendran et al.¹²

Because nanopores are essential to life, when they fail the results can be catastrophic. The deadliness of many diseases and toxins is the result malfunctioning protein-based nanopores.¹²⁻¹⁵ Through understanding the physics behind how such pores work, and even potentially building our own, many lives can be saved. In the absence of the ability to build and study synthesized nanopores, using those found in nature is a tempting option. One technique that was developed to this end was the Nobel Prize winning patch clamp which was developed by Erwin Neher and Bert Sakmann in the late 1970s and 1980s.¹⁶ This allowed for the isolation of a single biological ion channel, embedded in a lipid bilayer, which could be studied by monitoring the current passing through it. Recently, this line of research has received attention as a potential method to sequence DNA.¹⁷ Researchers have been able to apply a voltage across a membrane containing an α -hemolysin pore and monitor the

current as DNA molecules pass through.¹⁸ The pore occlusion caused by the individual bases translocating the inner constriction results in a current signature unique to each base. From this current trace, the DNA sequence can then be deduced. Techniques such as this one, which are based on biological nanopores, have several benefits. The pore structure is known to high accuracy thanks to the use of crystallography and the consistency of one pore to the next is very high. Additionally, it is possible to chemically modify such pores at specific locations due to exposed reactive chemical groups. The downsides include the fragility of the lipid bilayer membranes which house the pores and the inability to easily change the pore dimensions or core structure, which is generally complex.¹⁹

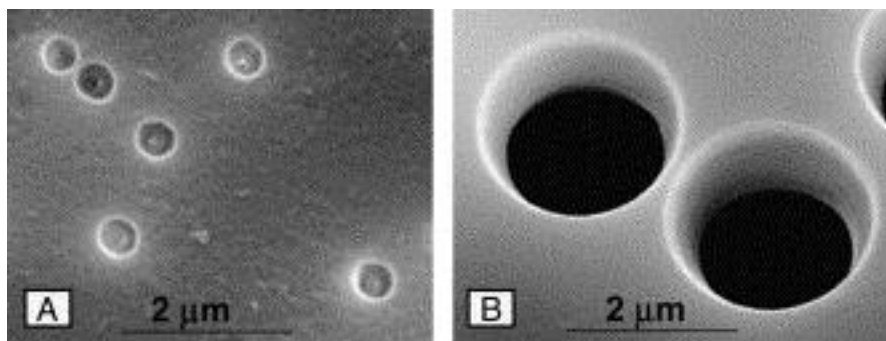


Figure 1.3 Synthetic nanopores. Early versions of synthetic which were made from polymer films. Scanning electron microscope images show the large opening of conical nanopores etched in PET (A) and a polyimide foil (B). Images courtesy of Zuzanna Siwy.

With the advancement of modern technology it has recently become possible to manipulate matter at the nanoscale.²⁰ This has opened up the possibility of generating synthetic nanopores similar to their biological analogs. Many techniques are now used to generate pores in a variety of materials including glass pipettes, SiN membranes, polymer membranes and carbon nanotubes/graphene.²⁰⁻²³ Artificial nanopores allow for two important lines of research to be done. First, these pores have simple sizes, shapes and structures which can be controlled and designed. Along with their ability to withstand a wide range of testing environments this lets pores be used for much needed fundamental

studies on nanofluidic phenomena. Much is still not known about the steric, electrostatic and hydrophobic effects that govern pore behavior at the nanoscale. Second, synthetic pores provide a foundation to modify and build on in order to design more sophisticated pores of our own. The ability to design synthetic pores that have the properties and abilities of nature's protein based pores would be incredibly useful in a variety of fields.²⁰⁻²³

In this thesis, the fundamental workings of three very different types of nanopores will be explored. First, α -hemolysin pores imbedded in a lipid bilayer will be utilized to look at what effects govern the speed of DNA translocation. Second, a polymer pore fabricated through the track-etch technique will be modified with DNA in order to create a synthetic nanopore which exhibits a gating response. Finally, nanochannels are created using the interior of single CNTs and the physics underlying these channels unique transport properties is studied.

Chapter 2: Theoretical Background

2.1 Nanopore Transport Theory

2.1.1 Charged Surfaces and the Debye Length

One unique characteristic of nanopores is the relative influence that surface properties have on overall transport behavior. This is primarily caused by the fact that as the diameter of a pore decreases, the ratio of surface area to volume dramatically increases. As a result, molecules which pass through a nanopore will generally have strong and frequent interactions with the pore walls. For this reason, the physics of charged surfaces submerged in an aqueous solution are vitally important in formulating a complete picture of nanopore transport.

Regardless of the geometry our charged surface has, we can imagine that it begins to appear flat and extend outward to infinity from the perspective of a particle which is very small and close. Making this assumption, we will consider an infinite plane with surface charge σ submerged within a solution containing ions, one of which can be described by its distance, x , away from the surface. The potential felt by our particle will then be the result of both the surface charge and the charge on neighboring ions in solution. In order to write an expression for the density, ρ , of ions near the surface, we can use the common Boltzmann distribution

$$\rho(x, t) = \sum_i z_i F C_i e^{\frac{z_i F \phi(x, t)}{RT}} \quad (2.1.1)$$

with R representing the gas constant, T the solution temperature, F the Faraday constant, ϕ the electric potential, C_i the bulk ion concentration, z the ion charge number and i as an index which sums over all the present ion species. In our system, it will be assumed there are only

two symmetrical ions of opposite charge, such as potassium and chloride. From this, we can write out the density of ions given from Equation 2.1.1 as

$$\begin{aligned}\rho(x, t) &= zFC_0 \left(e^{-\frac{zF\phi(x,t)}{RT}} - e^{\frac{zF\phi(x,t)}{RT}} \right) \\ &= -2zFC_0 \sinh \left(\frac{zF\phi(x, t)}{RT} \right)\end{aligned}\tag{2.1.2}$$

taking advantage of the trigonometric identity for sinh. For the next step, we need to plug the expression for $\rho(x, t)$ into the Poisson equation which is given by

$$\nabla^2 \phi = -\frac{\rho}{\epsilon\epsilon_0}\tag{2.1.3}$$

and tells us the relationship between a given charge distribution and the resulting potential. The ϵ and ϵ_0 in the above equation represent the dielectric constant of our solution and the permittivity of free space, respectively. Continuing with the substitution and dropping the ∇ in favor of a one dimensional derivative relevant to our system as well as dropping the time parameter gives:

$$\frac{d^2 \phi}{dx^2} = \frac{2zFC_0}{\epsilon\epsilon_0} \sinh \left(\frac{zF\phi(x)}{RT} \right)\tag{2.1.4}$$

To further simplify this expression, we can restrict our analysis to cases such that ϕ is much smaller than the product of R and T which allows the sinh function to be approximated by the first term in its Taylor expansion. This gives the now linearized Poisson-Boltzmann equation given below.

$$\frac{d^2 \phi}{dx^2} = \frac{2z^2 F^2 C_0}{\epsilon\epsilon_0 RT} \phi(x) = \frac{1}{\lambda^2} \phi(x)\tag{2.1.5}$$

To solve this equation we need to impose appropriate boundary conditions for our system. The first is that the potential drops off to zero as x approaches infinity and the second is that

the potential is continuous at the surface ($x = 0$). Putting everything together and solving the system of equations gives us the following expression for ϕ :

$$\phi(x) = \phi_0 e^{-\frac{x}{\lambda}} \quad (2.1.6)$$

The constant ϕ_0 in this exponential equation represents the potential at the charged surface. This solution to the potential near a charged surface is called the Debye-Hückel equation and is very useful in understanding nanopore behavior.

Perhaps the most important result of the above derivation is the definition of the parameter λ in Equation 2.1.5 and 2.1.6 which is given explicitly below.

$$\lambda = \sqrt{\frac{\epsilon \epsilon_0 RT}{2z^2 F^2 C_0}} \quad (2.1.7)$$

This term is known as the Debye length and provides a characteristic length scale for determining the importance of surface charge effects on nanopore behavior. Looking at Equation 2.1.6 tells us that a charged surface will attract ions of the opposite charge, artificially increasing the concentration of that ion above bulk behavior. This shielding effect will then die off at an exponential rate until the ion concentration eventually returns to bulk values. The Debye length then, is the distance at which the potential has decreased by a factor of $1/e$. Looking at Equation 2.1.7 also shows that the Debye length is inversely proportional to the square root of the bulk electrolyte concentration. To better see this, we can rewrite the Debye length for the specific case of a monovalent 1:1 set of ions in water at room temperature (25°C) with its concentration expressed in terms of moles/liter.

$$\lambda = \frac{0.304}{\sqrt{C_0}} \quad (2.1.7)$$

The output of this formula gives us the Debye length in the units of nanometers which is convenient when discussing nanopores. It also shows us that at a salt concentration of 1 M

the Debye length is only 0.304 nm which is much smaller than the diameter of most pores used in this thesis. If the same pore is instead measured in a concentration of 10 mM, the Debye length becomes 3 nm which is sufficient to significantly alter the behavior of truly nanoscale pores. For this reason, testing pore behavior across a range of salt concentrations can provide insight into both the pore dimensions and surface charge characteristics.

The unique organization of ions near a charged surface in an aqueous environment is typically referred to as an electrical double layer. The structure of parallel charged layers is where the term double layer comes from and is reminiscent of a traditional parallel plate capacitor. The original idea was discovered by Hermann von Helmholtz who, prior to the formulation done above, realized that ions of opposite charge would adhere to a charged surface in solution. He was also able to show that this phenomenon resulted in a unique type of capacitance.²⁴ What Helmholtz did not include in his formulation is that this capacitance is dependent on an applied potential and ionic concentration. These issues were later accounted for in models worked out independently by both Louis Gouy (1910) and David Chapman (1913).^{25,26} This formulation is now called the Gouy-Chapman model and is essentially what was derived above. It wasn't until 1924 that Otto Stern combined the ideas of Helmholtz with the Gouy-Chapman model.²⁷ This hybrid depiction of the double layer is drawn in Figure 2.1.1 and shows the inclusion of both a Stern layer and diffuse layer.²⁸ The Stern layer is thought of as immobile charges across which the potential drops off linearly while the diffuse layer has ions with some mobility and has a potential which decays exponentially. More modern models of the electrical double layer now exist, accounting for things such as a penetrable Stern layer,²⁹ the interaction of the solvent with the surface interface³⁰ and partial charge transfer between charged electrode surfaces and solutions,³¹

but the improvements they offer are small enough to ignore for the work presented in this thesis.

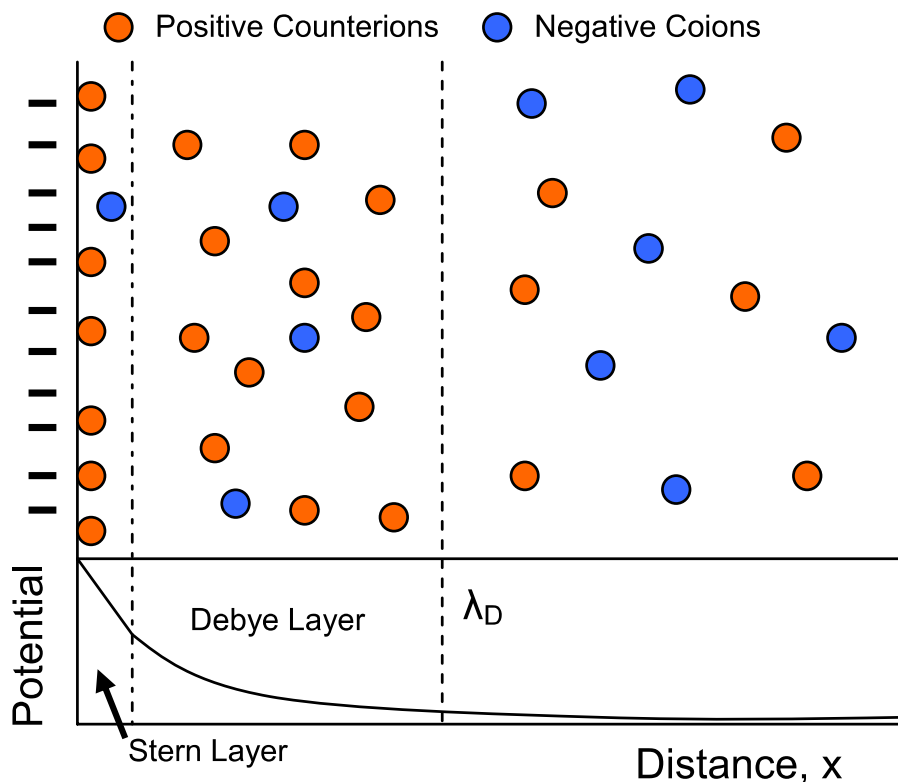


Figure 2.1.1 Electrical double layer. A Model of the electrical double layer shows the different resulting layers. The Stern layer is represented by an immobile layer of ions and has a linear drop in the potential. The Debye or Diffuse layer shows an exponential drop in potential and an increased ion concentration resulting from the charged surface. At distances beyond the Debye length, the potential is reduced by a factor of e or more and the concentrations approaches that of bulk. Figure courtesy of Eric Kalmen.²⁸

2.1.2 Nanopore Transport Physics

Now that we have an understanding of the charge distribution inside of a nanopore, we can begin to look at the overall transport behavior. The source of transport through a nanopore is the presence of a potential energy difference across the pore. There are many different sources for such a potential difference, including pressure, concentration gradients,

temperature gradients and electrostatic potential. The transport resulting from these types of potential differences can be roughly broken up into two types. The first is the movement of individual particle species resulting from electrostatics or concentration gradients while the second is the movement of the bulk solution due to something like an applied pressure gradient. To give a more specific example the case of KCl dissolved in water can be looked at. In the presence of an electrostatic potential it is easiest to study the resulting force on individual ions, assuming that the water around them is stationary. In the presence of an applied pressure however, the volume of water/ion mixture that is displaced needs to be examined. There will also be some amount of coupling between these different types of transport due to the interactions between molecules in solution. The primary mechanism behind this comes from the fact that as the charged particles are moved via electric field, they will induce a drag force on the molecules around them, causing movement in the bulk fluid. We will work through these different types of transport one at a time, excluding heat since all experiments are done at room temperature, and finally put together a more complete picture at the end.

Starting with a single particle located within a potential gradient, we can write out the definition of its so-called mobility, μ , which is the velocity of the particle in response to an applied force.

$$\mu = \frac{v}{F} \tag{2.1.8}$$

Now, we can write out an expression for the flux, J , which is the total number of particles which pass through a cross-sectional unit area (perpendicular to the particles motion), A , during an interval of time, dt , where C represents the concentration of particles.

$$J_e = vC \quad (2.1.9)$$

Assuming that we are dealing with a spherical particle in a constant electric field allows us to make a few substitutions. First, we can say that the force, F , felt by this particle is equal to its charge times the electric field it feels, or qE . Next, we can take advantage of the Einstein relation between the diffusion constant and mobility, given by $D = \mu k_B T$. Finally, thanks to Stoke's law, we know that the mobility of a sphere within viscous flow is given by

$$\mu = \frac{1}{6\pi\eta r} = \frac{D}{k_B T} \quad (2.1.10)$$

where η is the viscosity of the fluid and r is the radius of the particle. Now we can write out in full the expression for flux, adding the position along the pore, x , and time dependence of the electric field and concentration.

$$J_{ep}(x, t) = D \frac{qE(x, t)C(x, t)}{k_B T} \quad (2.1.11)$$

This term describes what is called the electrophoretic induced current. Having arrived at an expression for the flux resulting from an applied electric field, we can next turn to the force created by a concentration gradient. It is well known that particles in areas of high concentration will have a net diffusion towards areas of lower concentration. More specifically, Fick's law of diffusion tells us that flux is proportional to the concentration gradient which is written below.

$$J_d(x, t) = -D \frac{dC(x, t)}{dx} \quad (2.1.12)$$

With electrophoresis and diffusion now described, we can turn to the final piece of the puzzle. We know that particles under the influence of electrophoresis will drag some amount of the surrounding, neutral molecules with them due to friction. Once the system reaches equilibrium this means a velocity can be assigned to the surrounding fluid, u_{eo} . With

this definition, it is then possible to write out the flux of our charged particles which will be a product of u_{eo} and the particle concentration.

$$J_{eo}(x, t) = u_{eo}C(x, t) \quad (2.1.13)$$

This term is generally referred to as electroosmotic current. To complete the picture, we can combine the previous three equations into one expression that describes particle motion due to all three types of transport. Summing the three relevant terms results in the following expression.

$$J_{tot}(x, t) = J_{ep}(x, t) + J_d(x, t) + J_{eo} = D \left(\frac{qE(x, t)C(x, t)}{k_B T} - \frac{dC(x, t)}{dx} \right) + u_{eo}C(x, t) \quad (2.1.14)$$

This equation is a one dimensional version of what is known as the Nernst-Planck equation, with the inclusion of electroosmotic flow. Generalizing to three dimensions, exchanging electric field for the potential and writing in units of Coulombs per meter squared result in the most common form of the Nernst-Planck equation.

$$J = -zFD \left(\nabla C + \frac{zFC}{RT} (\nabla \phi) \right) - u_{eo}C \quad (2.1.15)$$

At this point we have successfully included all relevant types of transport, but we are missing a way in which to find u_{eo} in the above equation. To do this, we need to relate the movement of the solution as a whole to a force which is applied to it. This is precisely what the Navier-Stokes equation describes and it is given in full below.

$$\rho_m \left(\frac{\partial u}{\partial t} + u \cdot \nabla u \right) = -\nabla P + \eta \nabla^2 u + \rho_e \nabla \phi \quad (2.1.16)$$

In this equation, ρ_m represents the mass density, ρ_e represents the charge density, u represents the fluid velocity and P represents an applied pressure. Luckily, we can make several simplifications to this equation when applying it to our system. First, the left hand term, which is referred to as the inertial term can be assumed to be negligible. This is

because we are dealing with a situation where the viscous forces greatly overwhelm the inertial forces. The ratio of these two forces is known as the Reynolds number and will be sufficiently low in our system.³² The second simplification we can make is to remove the time dependency of the equation. This is allowed since any changes to the potential are sufficiently small compared to the kinetics of our fluid particles. Following these assumptions, we can write out what is referred to as the Stokes equation, except with the added force term due to the electric potential.

$$-\nabla P + \eta \nabla^2 u = -\rho_e \nabla \phi \quad (2.1.17)$$

Finally, one more equation must be added which represents the fact that our fluid is both non-compressible and that there is zero total flux in or out of our entire system. This can be done using the following continuity equation for a non-compressible fluid.

$$\nabla \cdot u = 0 \quad (2.1.18)$$

We now have a complete model representing all forms of transport that will be seen in our pores. The Navier-Stokes, Nernst-Planck and Poisson equations (sometimes called the PNPS model) together can be solved to predict the overall ionic current observed in a nanopore. The specific geometry and setup of the nanopore used will decide the corresponding boundary conditions needed. Solutions are generally complex and require the use of computer software such as COMSOL or Matlab. In the nanochannels discussed in Chapter 3 and 4, electroosmotic current is known to be very low allowing for simplification of the analysis.³³ In this case, the term containing u_{e0} in the Nernst-Planck equation can be dropped and as a result the Navier-Stokes equation is not required. This is called a PNP formulation and has been solved for many different pore geometries. An example solution is given in Figure 2.1.2 and shows that in a conical nanopore with a negative surface charge,

the data match the prediction well.³⁴ The pores used in this PNP model are very similar to those used in Chapter 4 of this work and the nonlinear behavior will be discussed further there. In Chapter 5, the pores used were found to have very high electroosmotic flow resulting in the need for a full PNPS set of equations.

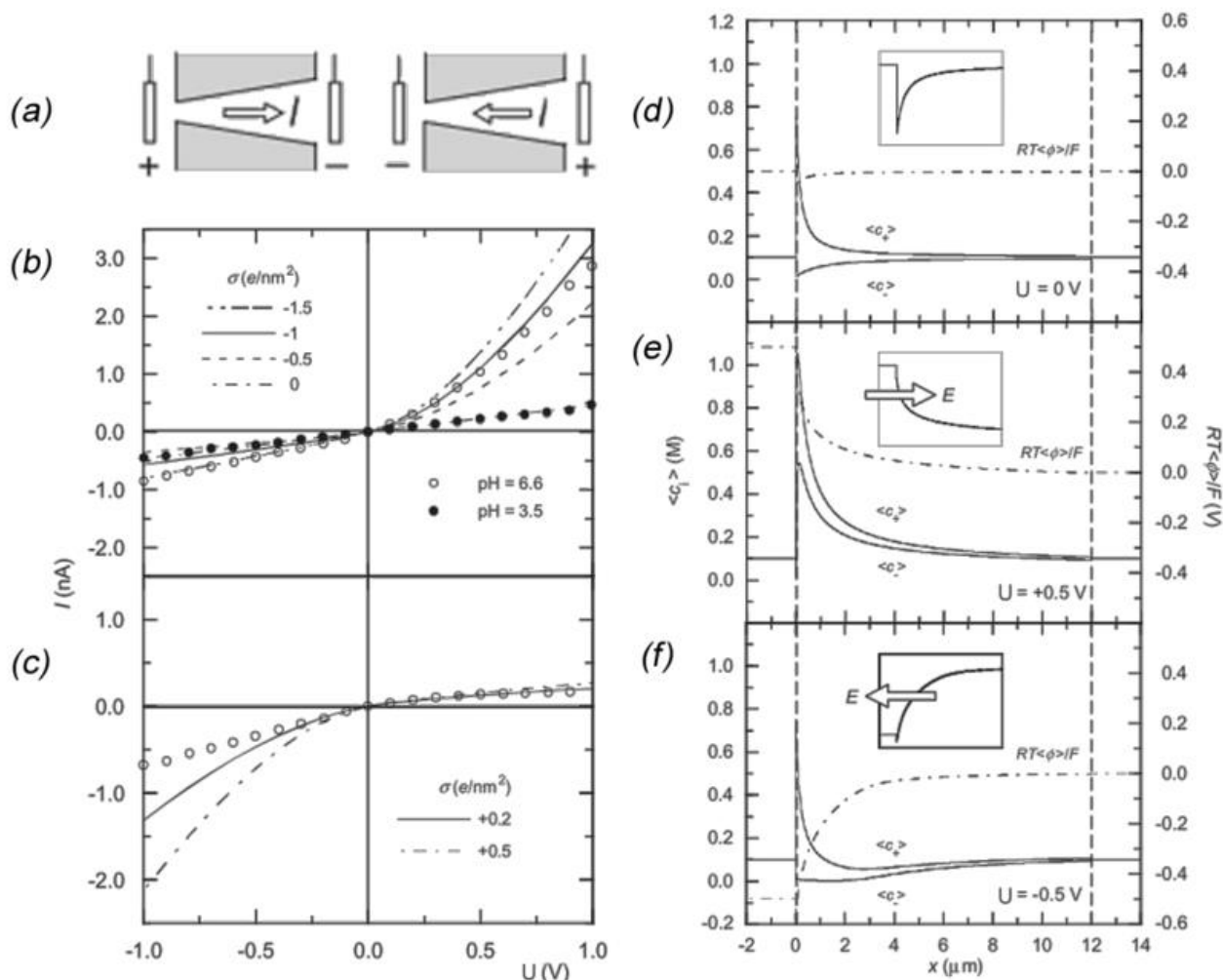


Figure 2.1.2 PNP calculation. Results from numerical PNP calculations for the ion current profiles and total ionic current for a conical nanopore with negative surface charge. (a) Electrode configurations are shown for the currents shown in (b) and (c). The negative surface charge comes from carboxyl groups, which become protonated around pH 3. Concentration profiles along the pore are shown in (d)-(f) for several applied voltages. Insets show results zoomed in near the tip of the pore. Figure taken with permission from EDP Sciences from Cervera et al.³⁴

2.2 Electrochemical Setup

2.2.1 Silver/Silver Chloride Electrodes

Directly measuring the ionic current through any type of nanopore can be difficult due to the fact that standard electronics are electron based. In order to interface a nanopore in ionic solution with a standard ammeter the ionic current needs to be converted into electrons. This is typically done through an electrochemical setup where some type of electrode placed in solution undergoes a chemical reaction absorbing an ion and releasing an electron, or vice versa. It is important to understand the details of this reaction to properly interpret the observed electronic current through our nanopores.

The chemistry selected for this work was that of Silver (Ag)/Silver Chloride (AgCl) electrodes. These are very common reference electrodes used throughout the chemistry community and even in medical applications such as electrocardiography.³⁵ The Ag/AgCl electrode works through a redox reaction between the pure silver and its salt form. In a system which is made of two Ag/AgCl electrodes which are used to apply a voltage across a salt solution, such as KCl, Cl⁻ ions are exchanged with electrons through the following chemical equation.



It can be seen that at one electrode an electron is absorbed, releasing a Cl⁻ into solution. On the other electrode, the opposite reaction occurs with a Cl⁻ being incorporated into the electrode and an electron being released into the electronic system.

Due to the frequency of use, Ag/AgCl electrodes have been heavily characterized and are very useful in this work for a few reasons. The first is that the redox reaction has been found to have very fast electrode kinetics.³⁶ At the currents used here, it can be assumed

that the conversion from ions to electrons happens with 100% efficiency. Next, the electrodes are very stable across a wide range of pH values allowing for pH based nanopore characterization. Finally, the electrodes are safe, and easy to acquire via commercial ordering or making them from silver wire.

2.2.2 Electrochemical Cell

When two Ag/AgCl electrodes are placed on either side of a membrane, such as in the electrochemical cell shown in Figure 2.2.1 the resulting potential will be given by the Nernst equation.

$$E_{cell} = E_{cell}^0 - \frac{RT}{nF} \ln(Q) \quad (2.2.2)$$

Here, E_{cell} represents the potential across the membrane, E_{cell}^0 represents the potential resulting from differences in electrode makeup, R is the gas constant, T is the temperature, F is the Faraday constant, n is number of moles of electrons and Q is the reaction quotient

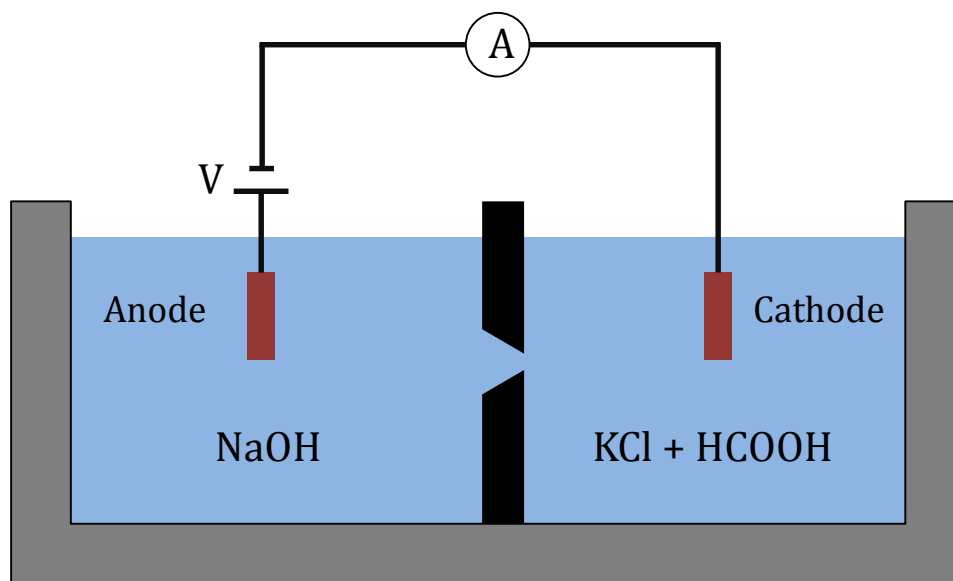


Figure 2.2.1 Electrochemical cell. Diagram of one electrochemical cell that was used in this work.

which is given by the ratio of ion concentration on each side of the membrane. It can be seen then, that so long as the KCl concentration and electrodes are kept identical on each side, there will be no resulting potential difference. We can then attach a voltage source and apply a potential difference directly across the electrodes in order to measure the ionic current through the membrane.

It is important to remember that any potential gradient applied between the electrodes is actually spread out across the whole system, of which the nanopore is just one element. The system can be thought of as many different resistance elements in series with each other. Each resistance in the circuit is also in parallel with a capacitance resulting from the formation of the electric double layer discussed earlier. This is represented by Figure 2.2.2 and includes the electrode resistance, bulk solution resistance, and pore resistance. At the size scales we are making our pores however, it turns out that the rest of the system can

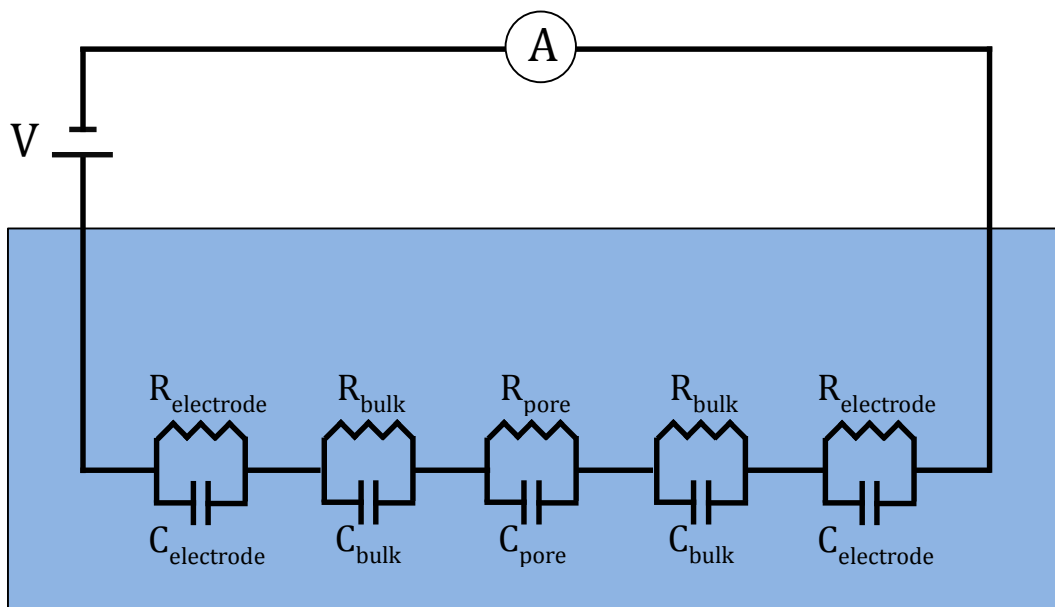


Figure 2.2.2 Electrical model of a cell. The equivalent electrical circuit for a pore in an electrochemical cell is shown. Due to the nanopore being many orders of magnitude smaller than the rest of the system (gigaohm resistance values), it is safe to assume the entire voltage drops across the pore alone.

be ignored. The resistance of Ag/AgCl electrodes is known to be lower than 10 Ohms,³⁷ while the resistance of the bulk solution depends on the geometry. In the cells used in Chapter 3 and 4, the bulk solution resistance at 1 M is roughly 4 Ohms, while in Chapter 5 a smaller cell is used with a resistance of around 10^3 Ohms. In either case, these resistance values are many orders of magnitude below that of our nanopores, which is in the range of 10^9 Ohms. This means we can assume that any applied voltage is felt entirely across our pores which makes data analysis much easier.

2.3 Coulter Counter

2.3.1 The Resistive Pulse Technique

The coulter counter technique is based on the simple idea that when a particle passes through a pore, it will temporarily change its resistance.³⁸ A schematic showing the resistive pulse technique is shown in Figure 2.3.1. This is a technique that can be used to learn various

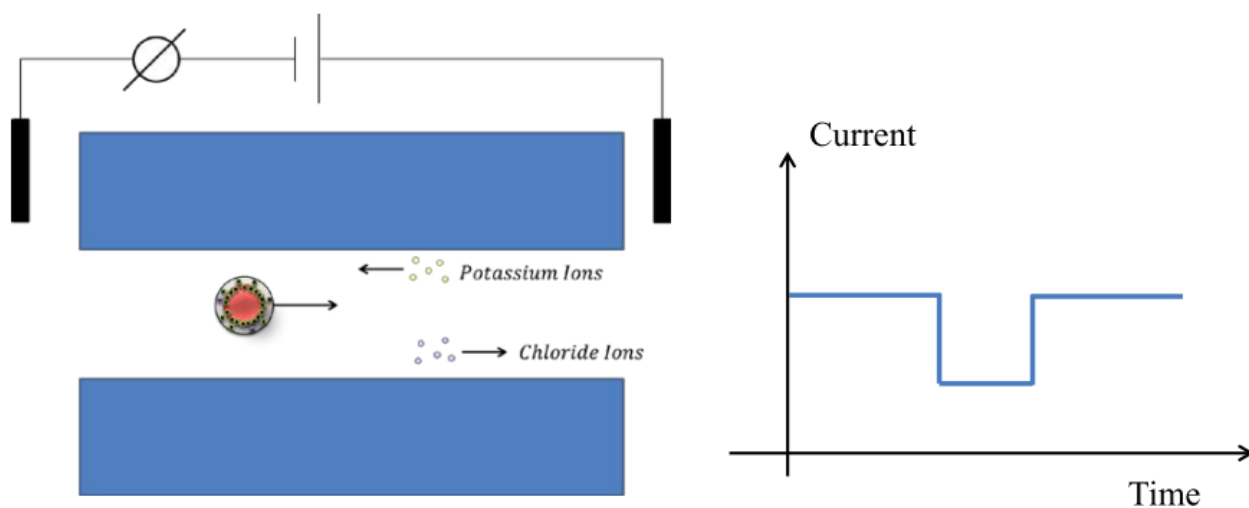


Figure 2.3.1 Resistive pulse. Schematic of a resistive pulse generated from a particle passing through a nanopore. While the particle is inside the pore, it changes the ionic resistance and produces a pulse in a plot of the current as a function of time. Figure courtesy of M. Pevarnik.⁴³

types of information about a particle, such as its size and charge if the characteristics of the channel are known (or the other way around).³⁹ In this thesis, the coulter counter is used, mostly qualitatively, with several different types of pores as proof of particle translocation. As a result, only a simple model of how the current amplitude can be modulated will be discussed. A more complete description, especially for very small pores and particles, is still not completely agreed upon, but a good summary is given by Davenport et al.⁴⁰

Assuming we start with a cylindrical ion channel with radius r and length L which has ohmic behavior, we can write out its resistance as

$$R_0 = \int_{-L/2}^{L/2} \frac{1}{A(x)} dx = \frac{4L}{\kappa\pi D^2} \quad (2.3.1)$$

where L is the pore length, A is the cross-sectional area and κ is the bulk ion conductivity. Now, as a particle enters the pore it will change the cross sectional area of the pore over the region it blocks pore transport. To find the new value of R for the pore we have to integrate over this new region which now holds the particle and add it to the sections of the pore which are still empty, if they exist. It is also important that we assume the particle is roughly the same size (within a factor of 10) as the pore diameter so that we can assume a constant current density across the channel, otherwise, budging electric field lines at the pore wall must be accounted for.^{41,42} If we assume a spherical particle with diameter d translocating the pore we can break up our total pore resistance as

$$R_1 = \int_{-L/2}^{L/2} \frac{1}{A(x)} dx = \frac{4(L-d)}{\kappa\pi D^2} + \int_{-d/2}^{d/2} \frac{1}{\kappa A(x)} dx \quad (2.3.2)$$

where the final term still requires an expression for the cross-sectional area through the region with the sphere in it. This can be written as

$$A(x) = \frac{\pi D^2}{4} - \frac{\pi d^2}{4} + \pi x^2 \quad (2.3.3)$$

With a little bit of work, we can plug this in and solve for the change in resistance and current due to our particle being inside the pore.⁴³

$$\frac{R_1 - R_0}{R_0} = \frac{I_0 - I_1}{I_1} = \frac{D}{L} \left(\frac{\sin^{-1}\left(\frac{d}{D}\right)}{\sqrt{1 - \left(\frac{d}{D}\right)^2}} - \frac{d}{D} \right) \quad (2.3.4)$$

A more general approach was calculated by Sung Kim et al. which describes a system with both an arbitrarily shaped pore and particle, defined by their radial functions $f(x)$ and $g(x)$ respectively.⁴⁴ The equation giving the resistance of the pore with a particle inside is given by

$$R = \frac{1}{\pi\kappa} \int_{-L/2}^{L/2} \frac{1}{f^2(x) - g^2(x)} dx \quad (2.3.5)$$

where the only restriction is that both the pore and particle have symmetry around the x axis.

It is worth noting that this approach only looks at the volume-restricting element which changes resistance. In different setups, it is also possible for the charge of the particle to influence the pulse resulting from its translocation. If the particle charge density is large enough then it can bring additional charges with it into the pore, which can compete with the steric blockage effects. In fact, in using extremely charge particles and specific pores, it is possible to produce current increases during translocation instead of blockades. An example of this can be seen by Golovchenko's group where they looked at DNA translocation through solid state nanopores and were able to see both current spikes and blockades depending on the system conditions.⁴⁵

2.4 DNA Basics

2.1.1 Description of DNA

DNA stands for Deoxyribonucleic acid and is made up of repeating units of a monosaccharide and phosphate backbone along with a nucleobase. DNA found in nature is generally in what is called the double stranded (dsDNA) form. This means that there are two polynucleotide chains joined with each other in a double helix formation. The unique ordering of bases is what nature uses to encode the information needed to create the building blocks of all life. The four nucleotides found in DNA are adenine (A), cytosine (C), guanine (G) and thymine (T). Each base has a unique chemical structure such that they bond in pairs – A is opposite and bonded to T and C is paired with G. DNA can also exist in what is called the single stranded form (ssDNA) which means that the double helix has been stripped in half, splitting

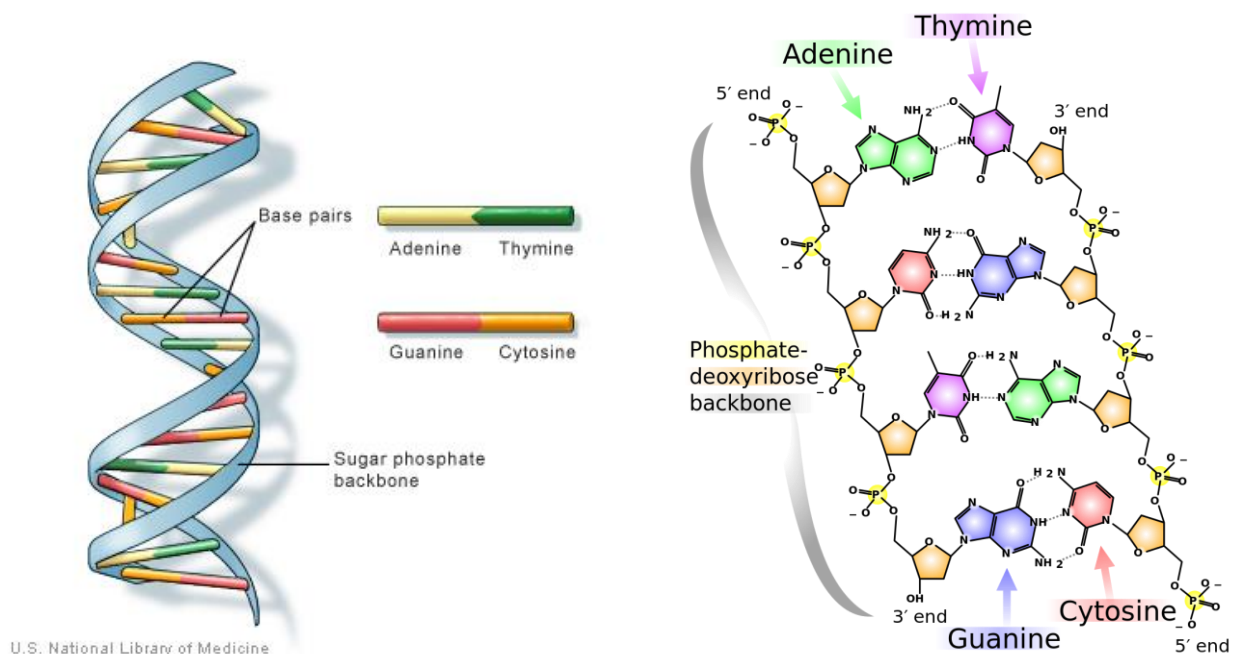


Figure 2.4.1 DNA structure. Cartoon drawings show the structure of DNA. Image on the left shows the double helix structure of dsDNA and the image on the right shows the bonds holding complimentary nucleotides together. These Images are reprinted with the courtesy of US National Library of Medicine and Madeleine Ball.

up and exposing the inner nucleotides. Each strand of ssDNA still encodes the same amount of information and the strands are said to be complimentary to each other. Under the right conditions, each single strand of DNA can reform a new double stranded DNA molecule, doubling the original amount of DNA. This process is called polymerase chain reaction (PCR) and is used in both the lab and in nature to replicate DNA. Figure 2.4.1 shows the structure of a double helix DNA molecule.

Chapter 3: Steric and Electrostatic Effects in Nanopore Translocation

3.1 Introduction

Perhaps the most fundamental characteristic of a nanopore is its ability to transport molecules from one side of a membrane to the other. Different types of pores found throughout nature have taken this concept and expanded on it, resulting in all sorts of different control mechanisms governing this transport. Specific groups of biological pores however, have remained fairly simple in design and purpose. Many of these pores originate and are produced by bacterial cells. While the three-dimensional structures composed of amino acids are complex compared to synthetic versions, the resulting pores are relatively easy to understand. Due to this, many such pores have attracted the attention of scientists for use in studying nanopore physics as well as for applications in biotechnology.

Of the long list of bacterial pores in nature, there exist a small handful that have spent the most time in the spotlight. Included in this group is gramicidin, which is produced by a type of bacteria called *Bacillus brevis* which is found in soil, *Mycobacterium smegmatic* porin A (MspA) which is produced by various bacteria in the *Mycobacterium* genus, and α -hemolysin which comes from the potentially dangerous *Staphylococcus aureus*. Of these three, the latter two are currently being used in the search for fast and accurate DNA sequencing technologies.⁴⁶⁻⁵⁰ One particularly noteworthy example comes from a company called Oxford Nanopore Technologies. They have recently released a portable DNA sequencing device, based on a modified α -hemolysin pore, which is amazingly not much larger than a standard USB flash drive (and plugs into your computer just like one).⁵¹ These types of technologies are possible because of the size and structure of such bacterial pores.

As previously mentioned, α -hemolysin comes from the *Staphylococcus* genus and is highly toxic to most animal cells. The pore has the ability to incorporate itself into the lipid bilayer which, when combined with its transport properties, can cause a lot of problems. α -hemolysin essentially acts like an unrestricted channel, allowing transport of any molecule that can fit through its internal diameter. As molecules required by cells to live are allowed to exit, and unwanted outside molecules are allowed to enter, cell death eventually occurs, typically through lysis.^{8,9} The same reasons that make the pore so toxic to cells, however, make it a great model pore to work with.

The structure of α -hemolysin is known thanks to having been solved using X-ray crystallography techniques.⁵² The entire molecule is roughly 10 nm long and looks a little bit like a mushroom with a cap that sits on the lipid membrane and a stem which is inserted to the other side. The interior channel is largest at both the entrance and exit tapering down to a minimum aperture close to the center. This internal central constriction is only about 1.3 nm in diameter and is responsible for most of the pores usefulness. Somewhat surprisingly, with a little bit of nudging (most often in the form of an applied voltage) both modeling and experimental studies have verified that DNA is easily capable of being transported through this small channel.⁵³ Only single stranded DNA (ssDNA) can accomplish this, which happens to be ideal since the exposed nucleotides make sequencing much easier. The details of how this sequencing is accomplished will be elaborated on in the next section.

Due to its promising structure and prevalence in the DNA sequencing industry, α -hemolysin was selected for use in this study. We aim to model the translocation of DNA and DNA like molecules through one of these pores in order to elucidate on some of the underlying physics governing transport. One specific question relates to the rate of DNA

transfer since it is directly tied to the throughput of future technologies. Higher transport is directly tied to the rate at which samples can be processed, but only up to a limit. If the translocation occurs too quickly, the interpretation of the data becomes more difficult and accuracy decreases. It is for these reasons that the ability to accurately control and balance the movement speed of DNA through a nanopore is essential.^{54,55} In the following chapter we modify DNA with additional peptide tags which, verified through molecular modeling, change both the DNA's effective radius and charge density. We can then monitor the translocation speed and interpret the relative importance of steric and electrostatic effects on transport speed. Studies of this type are essential to unlocking the full potential of nanopore based sequencing and the results can be applied to pores of any type.

3.2 Theory and Background

3.2.1 DNA Translocation through α -hemolysin

As mentioned in the introduction, α -hemolysin has an internal constriction with a diameter of roughly 1.3 nm. Comparison to the width of a double helix strand of DNA, which is about 2.3 nm, makes it clear that dsDNA is unlikely to pass through the pore. When the DNA is in its single stranded form however, is it sufficiently small to feed through α -hemolysin. It is important to note that this requires the ssDNA to enter single file. This is typically a desirable characteristic since ssDNA is known to fold up into various

confirmations, based on free energy considerations, which can make further analysis difficult.

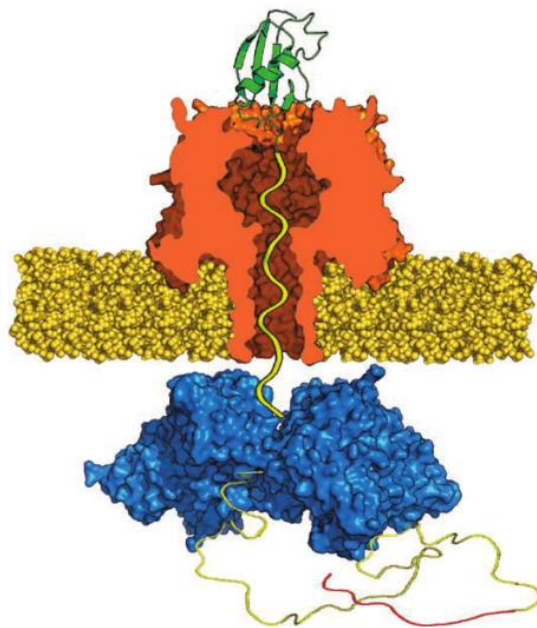


Figure 3.2.1 Pulling proteins through α -hemolysin. Schematic showing an α -hemolysin pore imbedded in a lipid bilayer which also has the addition of an ClpX unfoldase protein. A DNA tag that is attached to a Smt3 domain is threaded through the pore using an applied voltage. Fueled by ATP hydrolysis, the ClpX pulls on the tail and causes unfolding and translocation of the Smt3 domain. Figure reprinted with permission from Macmillan Publishers Ltd from Nivala et al.⁵⁶

Due to the size difference between ssDNA and α -hemolysin being so small it is typically required that the ssDNA be pushed through. This has been accomplished a few different ways including the addition of proteins near the α -hemolysin which feed the DNA through (Figure 3.2.1) as well as through the use of an electric field.^{55,56} In the latter case, an electrochemical cell is used to maintain a voltage across a membrane containing an α -hemolysin pore. Due to the large negative charge present on DNA it can be electrophoretically driven along this potential. If the DNA is placed on the proper side of the membrane, this driving force will eventually cause it to encounter the α -hemolysin pore. The initial opening of the pore is large enough to contain folded ssDNA strands, but upon

threading into the internal constriction, the ssDNA is then transported through in a straight line. In this manner, the electrostatic characteristics of the DNA make it possible to gain some control over the rate and frequency of ssDNA translocation events. Even at low voltages however, DNA can move through the pore quickly, with rates of 1 to 5 μs per base, which may be faster than desired for the purpose of data analysis.^{55,57} As a result, both more advanced recording systems and methods to slow down the DNA are required. Some progress has been made on the former need with at least 3 μs resolution reported and the latter challenge is the focus of this work.⁵⁸ One key method which can be used to control translocation rate would be to alter the relative diameters of the ssDNA and inner constriction of the α -hemolysin. It has previously been shown that DNA can be modified with chemical tags, impacting its translocation behavior.⁵⁹ By increasing the ssDNA diameter and altering its charge, its movement through the pore can be significantly slowed, which is the motivation for the work done in this chapter.

3.2.2 Applications of the Coulter Counter Technique

The coulter counter technique, which is discussed in Chapter 2, can be used to identify the passage of DNA molecules through an α -hemolysin pore. As a ssDNA strand enters and occludes the channel, the pore resistance is increased, creating a pulse in the ionic current. The amplitude of the resistive pulse is dependent on the volume occluded by the molecule and is therefore largest when translocation through the internal constriction is occurring. Due to the similarity in size between the channel diameter and modified ssDNA molecule the current is expected to drop almost to zero during a translocation event. According to MD simulations, ssDNA naturally has a diameter around 1.4 nm but under confinement can

increase the angle between bases to achieve an effective diameter below 1.25 nm (see Figure 3.2.2).⁶⁰ As a very rough calculation, the pore and ssDNA can be modeled as cylinders of radius 1.3 and 1.25 nm respectively. Assuming the pore is entirely filled, which is reasonable since our ssDNA is much longer than the inner constriction of α -hemolysin, it can be seen that the occluded volume is roughly 93 percent.

$$1 - \frac{\pi(1.25)^2 - \pi(1.25)^2}{\pi(1.3)^2} = 0.93 \quad (3.2.1)$$

It also makes it clear that if the diameter of a ssDNA molecule increases, so does the amplitude of the pulse. In this work, we will be examining ssDNA molecules which have had their effective diameters increased through chemical modification. Using the resistive pulse technique, it is then possible to easily distinguish between the two molecules based on the

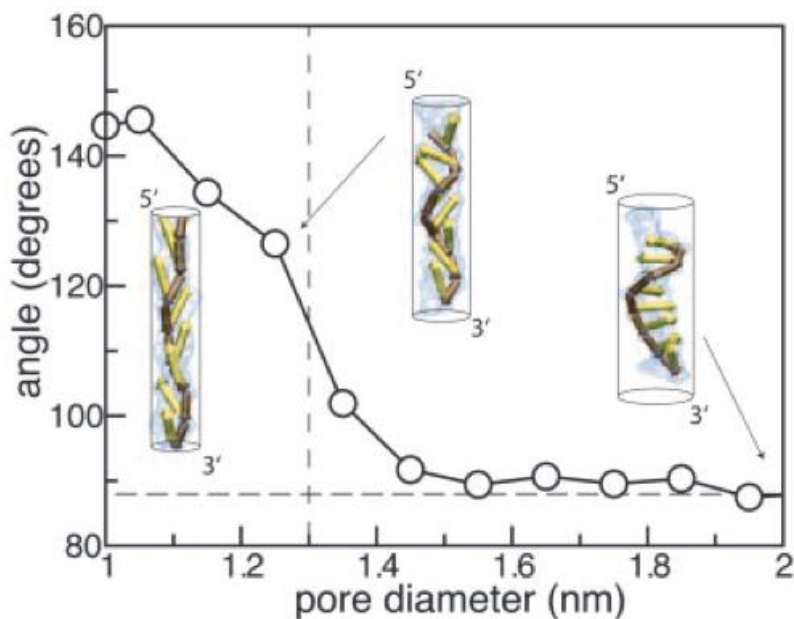


Figure 3.2.2 Diameter of ssDNA. Molecular dynamic simulations show the alignment of ssDNA under confinement in a cylindrical volume. Snapshots from left to right are taken at a radius of 1, 1.25 and 3 nm. The dashed vertical line represents the diameter of the inner constriction of α -hemolysin. The horizontal dashed line represents the angle between nucleotides when the ssDNA is unconstrained. Figure courtesy of Mathe et al.⁶⁰

recorded amplitude of the ionic current change. Additionally, the pulse amplitude can be used as an estimate of the ssDNA strand diameter, giving evidence that we have correctly synthesized the molecule. It is important to point out that this simple geometrical based model is an over simplification of the system since the behavior at this scale can be counter intuitive and is still being studied.⁴⁰ Even still, since the focus of this work is to study translocation duration, this model is sufficient for our needs.

3.2.3 DNA Sequencing using Nanopores

The goal of DNA sequencing is to correctly identify all of the nucleotides in a DNA molecule. To be useful, it is required that both the type and position along the strand are identified. In an ideal system, each correctly ordered nucleotide is sent through an appropriately sized channel while the channel resistance is monitored. In order to distinguish one nucleotide from another, it is required that they each have a unique size/shape/charge and therefore a corresponding unique current trace as they pass through the pore. While the difference in structure between nucleotides is small, it has been shown that they can be successfully distinguished. A schematic is shown in Figure 3.2.3.

The idea of nanopore based DNA sequencing has been around for at least 20 years with one of the first examples published in 1996 by Kasianowicz et al.⁴⁶ Generally, an electric field is used to drive ssDNA through an isolated biological or synthetic nanopore. In most methods, the intact ssDNA strand passes through the pore but alternative methods have been used, such as cleaving the nucleotides and sending them through individually.⁶¹ The characteristics of the nanopore are important and the diameter and length must be carefully selected. First, the diameter must be larger enough to allow ssDNA to enter but not so large

that the ssDNA can pass through in non-single file conformations. Second, the diameter of the pore must be small enough such that the small changes in nucleotide structure are sufficient to adequately detect. Finally, the pore length must be sufficiently short so that it is on the same scale as a single or a few nucleotides. If the length is greater than this, the current trace will be an average of all bases inside the pore at that instant and therefore harder to identify. In some technologies however, several bases are examined at once intentionally to introduce more redundancy into the system.⁵⁵ Various types of both biological and synthetic pores have been used although α -hemolysin seems to be a popular choice and is the pore focused on here. The inner constriction of this pore meets most of the above criteria which is why it is used so often.

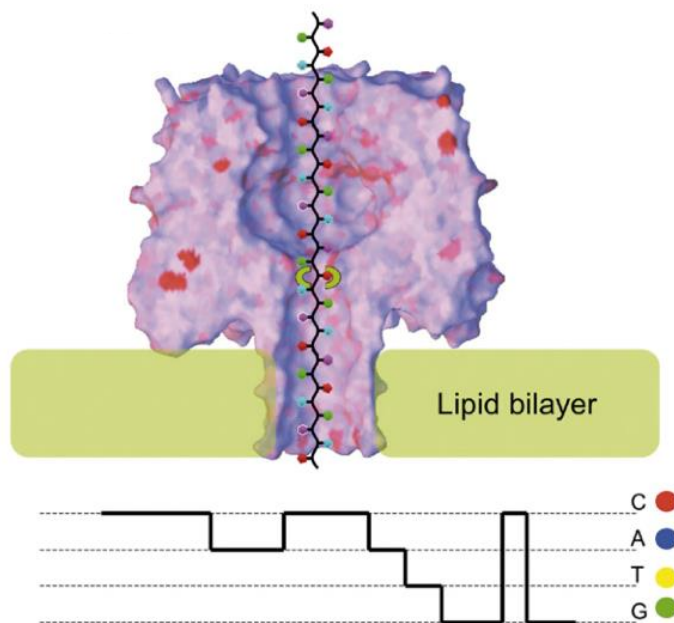


Figure 3.2.3 DNA sequencing. Model showing the resistive pulse technique used as a method for sequencing DNA. ssDNA is driven through an alpha hemolysin pore and the nucleotide specific current pulses are read and converted into the correct sequence. Image reprinted with permission from Elsevier from Hagen Bayley⁵⁵

3.2.4 Statistical Analysis of Translocation Events

The nature of DNA translocation behavior in α -hemolysin requires that large numbers of events are statistically analyzed to draw useful conclusions. In the case of this work, step like modulations in the ionic current were identified and the duration of the events were recorded. To understand what mechanics govern the rate of translocation, the distribution of these event durations was examined.

Before going further, it is useful to definition of the survival function $S(t)$. This function represents the probability that an event is at least as long as time t . In order to predict the form of the survival function, certain assumptions must be made about the system. If it is assumed that a ssDNA strand threaded into the pore exits through one dimensional diffusion against an applied potential, the one-dimensional Fokker-Plank equation can be used. This system can be modeled where $f(x,t)$ is the probability density function, t is time and x is the distance the ssDNA has moved along the pore from its initial position.

$$\frac{\partial}{\partial t} f(x, t) = D \frac{\delta^2}{\delta x^2} f(x, t) - \frac{\partial}{\partial x} \frac{F(x)}{\gamma} f(x, t) \quad (3.2.2)$$

D in the equation above is the diffusion coefficient, γ represents the coefficient of friction and $F(x)$ is the force term which includes terms from the applied voltage and entropic considerations. The survival function would then be the integral of $f(x,t)$ over the entire ssDNA molecule. Following the work of Wiggin et al. it can then be shown that in this case, the expected form of the survival function would be exponential at long times.⁵⁷ This is independent of the energy barrier the ssDNA is facing, so long as it is constant throughout the process. It is somewhat surprising then, that throughout the literature, and in the data

shown in the rest of this chapter, an exponential fit provides a poor match to the data, especially at long times.^{57,62,63}

The mismatch between a Fokker-Plank based model and the data, suggests that there are important considerations being left out. Most likely this includes interactions between the pore and ssDNA which are time and position dependent. In order to account for this, several alternate fits were used to interpret the survival probability data including a double exponential, stretched exponential and Becquerel function. When compared to our data, the best fit turned out to be from the latter option which is what we used for the remainder of the calculations.

3.2.5 The Becquerel Function

The Becquerel function was originally used in 1861 by Edmond Becquerel to model phosphor-luminescence decay rates.⁶⁴ More recently, it has been used to describe kinetics of CO binding to myoglobin at low temperatures.⁶⁵ In the context of this work, it was selected because it seems to most accurately match the interactions governing the exit time for ssDNA in an α -hemolysin pore. Unlike the formulation in the previous section, which only considers a single energy barrier facing the ssDNA, the Becquerel function allows for an energy barrier distribution. Equation 3.2.3 gives the survival function associated with the Becquerel function.

$$P_{survival}(t) = \left(1 + \frac{t}{\tau_0}\right)^{-\beta} \quad (3.2.3)$$

The symbol τ_0 represents a constant with dimensions of time and β is a dimensionless constant which controls the spread of the timescale distribution and can vary from 1 to infinity. This function has a known Laplace transform which can be used to express the

energy barrier distribution. Taking advantage of the Arrhenius relation, $\tau = e^{E_b/k_B T}$, this can then be written in terms of τ and is shown in Equation 3.2.4.

$$G(\tau) = \frac{(\tau_0/\tau)^\beta e^{\tau_0/\tau}}{\Gamma(\beta)k_B T} \quad (3.2.4)$$

We can then define the characteristic time, τ^* , which is associated with the peak of the energy distribution. Taking a derivative of Equation 3.2.4 with respect to τ and then setting it equal to zero leads to the definition of τ^* which is given below.

$$\tau^* = \frac{\tau_0}{\beta} \quad (3.2.5)$$

Arriving at the same conclusion as the work done by Wiggin et al. it is then this characteristic time constant which is most useful in characterizing the translocation of ssDNA through an α -hemolysin pore.⁵⁷ In order to analyze the data presented in this chapter, this Becquerel survival function is fitted to the raw dwell time data in order to extract τ_0 and β . These constants are then used to calculate τ^* for a particular sample.

3.2.6 Formalism of First Passage time for a Stochastic Polymer

Later in this chapter, a model describing the transport of ssDNA through an α -hemolysin pore will be described. The bases of this model comes from the stochastic process of a chain moving in one dimension. The formalism used to arrive at an expression for first passage time will be discussed here so that it can be utilized later in the chapter.

The system which will be analyzed consists of a chain that is broken up into N discrete segments and is restricted to movement in one dimension. This chain is trapped in a pore and we are interesting in the time it will take to escape. The position of the chain in the pore can be defined as the number of segments that have entered the pore, starting at 0. Lastly,

to distinguish the two ends of the pore, we can call the side on which the chain starts the *cis* side, and the opposite end the *trans* side. The system can now be described using the backwards master equation given below, where $P(n,\tau|m)$ represents the probability that the ssDNA will be in position n after time duration τ has elapsed if it started in position m .^{66,67}

$$\begin{aligned} \partial_t P(n, \tau|m) = & k_+(m)P(n, \tau|m - 1) + k_-(m)P(n, \tau|m + 1) \\ & - [k_+(m) + k_-(m)]P(n, \tau|m) \end{aligned} \quad (3.2.6)$$

In the above equation, k_+ and k_- represent what is called the hopping rates. These functions describe the rate at which the chain is shifting either one segment forward (+) or one segment backwards (-). The time derivative of $P(n,\tau|m)$ will then give $\rho(\tau,m)$ which is the probability distribution function for exiting the pore out of either the *cis* or the *trans* end. $\rho(\tau,m)$ is written for each end of the pore here.

$$\begin{aligned} \rho_{trans}(\tau, m) &= \partial_t P(N, \tau|m) \\ \rho_{cis}(\tau, m) &= \partial_t P(0, \tau|m) \end{aligned} \quad (3.2.7)$$

Integrating $\rho(\tau,m)$ from 0 to infinity gives the total probability of a strand exiting the pore through the appropriate side. This is defined as $w(m)$ and can be written specifically for the *trans* side.

$$w_{trans}(m) = \int_0^{\infty} \rho_{trans}(\tau, m) d\tau \quad (3.2.8)$$

In order to arrive at a solution, it is easiest to now rewrite Equation 3.2.6 in terms of $w(m)$ instead of $P(n,\tau|m)$.

$$0 = k_+(m)[w(m - 1) - w(m)] + k_-(m)[w(m + 1) - w(m)] \quad (3.2.9)$$

We are interested in solving this equation for the *trans* side only which will impose the following boundary conditions.

$$w_{trans}(0) = 0 \quad (3.2.10)$$

$$w_{trans}(N) = 1$$

$$w_{trans}(m) + w_{cis}(m) = 1$$

Solving Equation 3.2.9 using the boundary conditions given above is now possible and will produce an expression for $w_{trans}(m)$.

$$w_{trans}(m) = \frac{1 + \sum_{l=1}^{m-1} \prod_{j=1}^l \frac{k_-(j)}{k_+(j)}}{1 + \sum_{l=1}^{N-1} \prod_{j=1}^l \frac{k_-(j)}{k_+(j)}} \quad (3.2.11)$$

The goal of this procedure is to arrive at an expression for average passage time $\langle t \rangle$ which is not currently possible because $\langle t \rangle$ does not have boundary conditions for both $m = N$ and $m = 0$. To avoid this problem, we can instead solve for $\vartheta(m)$ which will be defined as the following product.

$$\vartheta(m) = w(m)\langle \tau(m) \rangle \quad (3.2.12)$$

We now have boundary conditions that apply to both the *cis* and *trans* side, which are shown below.

$$\vartheta(0) = 0 \quad (3.2.13)$$

$$\vartheta(N) = 0$$

Using this expression the master equation can be rewritten one final time.

$$-w(m) = k_+(m)[\vartheta(m-1) - \vartheta(m)] + k_-(m)[\vartheta(m+1) - \vartheta(m)] \quad (3.2.14)$$

Finally, it is now possible to solve for the average passage time $\langle t \rangle(m)$ as a function of both the hopping rates and exit probability.

$$\langle t \rangle(m) = \sum_{l=1}^{N-1} \sum_{i=1}^l \frac{w_{trans}(i)}{k_+(i)} \prod_{j=i+1}^l \frac{k_-(j)}{k_+(j)} - \frac{1}{w_{trans}(m)} \sum_{l=1}^{m-1} \sum_{i=1}^l \frac{w_{trans}(i)}{k_+(i)} \prod_{j=i+1}^l \frac{k_-(j)}{k_+(j)} \quad (3.2.15)$$

3.3 Experimental Setup

3.3.1 Nanopore Recordings

Single-channel current recordings were performed by using a planar lipid bilayer apparatus. A bilayer of 1,2- diphytanoyl-sn-glycero-3-phosphocholine (Avanti Polar Lipids) was formed on an aperture (80 μm in diameter) in a Teflon septum (Goodfellow Corporation, Malvern, PA) separating the *cis* and *trans* chambers of the apparatus. Each compartment contained 2 M KCl, 50 mM Tris-HCl, pH 8.0. Gel-purified heptameric α -hemolysin protein (final concentration 0.01–0.1 ng/ml) was added to the *cis* compartment to achieve insertion of a single channel into the bilayer. Subsequently, DNA samples that had been stored at 4°C after preparation were added to the *cis* chamber with a final concentration of approximately 1 μM . Peptide-modified DNA strands that had been stored in dry ice and freshly thawed on ice were not used for the analysis since they gave rise to unusually long translocation durations which might be caused by the formation of electrostatically bound dimers of arginine-tagged DNA strands. Transmembrane currents were recorded at a holding potential ranging from +100 mV to +180 mV (with the *cis* side grounded) by using a patch-clamp amplifier (Axopatch 200B, Axon Instruments, Union City, CA). For analysis, currents

	100 mV	120 mV	140 mV	160 mV	180 mV
R3	2182	2788	3565	5378	4369
R5	1968	2598	3305	3419	3145
R7	318	992	1619	1787	1211
D6	670	660	880	1641	N/A

Table 3.3.1 Number of translocation events. Number of events used in dwell time analysis for each voltage and modification

were low-pass filtered at 10 kHz and sampled at 50 kHz using a Digidata 1200 A/D converter (Axon Instruments). The number of events analyzed per peptide tag and per voltage was on average 250 for amplitude histograms and 1600 for dwell-time histograms. The detailed numbers of events per condition for the dwell-time analysis are provided in Table 3.3.1.

3.3.2 Peptide-DNA Molecule Preparation

Peptides with the sequence HOOC- Arg_n-Cys-NH₂ (n = 3, 5, 7) and HOOC-Asp₆-Cys-NH₂ were synthesized using standard Fmoc solid-phase peptide synthesis on a Syro automated system using pre-loaded Wang resin and HBTU coupling chemistry, followed by purification using high-performance liquid chromatography and chemical identification using ESI-MS. For the coupling of peptides to DNA, a synthetic oligonucleotide with the sequence 5'-ACA TTC CTA AGT TCT GAA ACA TTA CAG-3' (25 μL of a 1 mM ODN solution in 10 mM Tris, 1 mM EDTA, pH 8.0 buffer) carrying an amine-modified thymidine analogue at an internal position (underlined) was first reacted with the heterobifunctional cross-linker

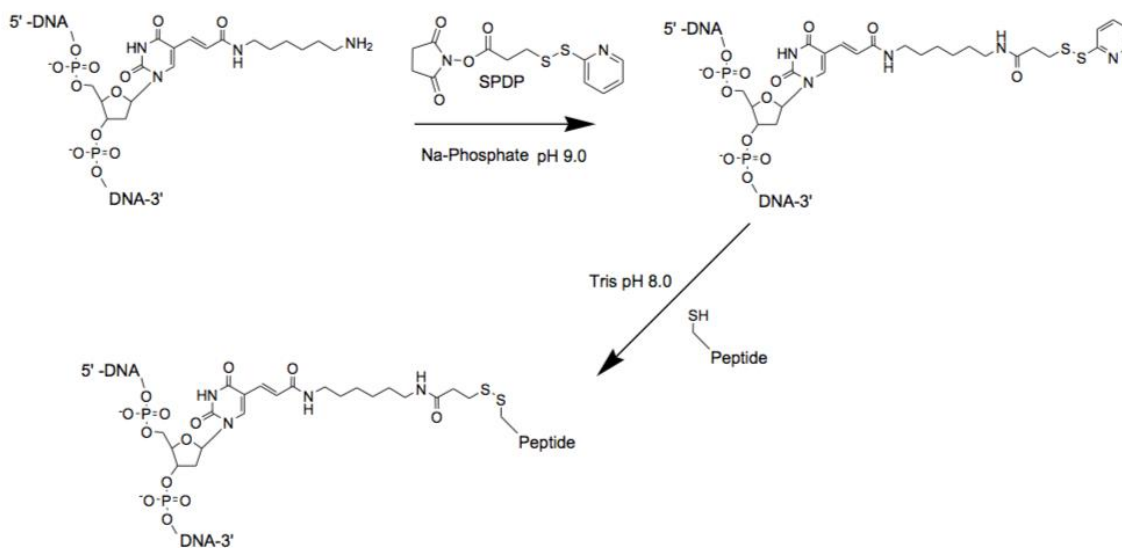


Figure 3.3.1 DNA-peptide coupling. Chemical scheme illustrating the chemical coupling steps to prepare oligo-arginine- tagged and oligo-aspartate-tagged DNA oligonucleotides.

N-succinimidyl 3-(2-pyridyldithio)-propanoate (10 μ L of a 250 mM solution in DMSO) in 0.1 M NaHCO₃, 50 mM NaCl, pH 9.0 (see Figure 3.3.1). The excess small molecule was separated from the ODN via automated size exclusion chromatography on an AKTA purifier. The added, thiol-reactive 2-pyridyldithio group was then coupled to a cysteine-bearing HOOC-Arg_n-Cys-NH₂ or HOOC-Asp₆-Cys-NH₂ peptide to form a disulfide bond (Figure 3.3.1). The resulting peptide-tagged DNA strands were purified and analyzed using anion-exchange chromatography (Resource Q column on an AKTA system) and MALDI mass spectrometry. The methods used here are similar to those used by Mitchell et al.⁵⁹

3.3.3 Molecular Modeling

The α -hemolysin crystallographic structure coordinates were taken from Protein Data Bank (PDB) entry 7AHL. Atoms missing from the PDB file (residues dLys-30, gLys-30, aLys-75, dLys-240, fLys-283, and aArg-66) were reconstructed using 'psfgen', which is part of the NAMD2 structure building module.⁶⁸ The protein was inserted into a patch of 150 \AA x 150 \AA pre-equilibrated and solvated 1- palmitoyl-2-oleoyl-sn-glycero-3-phosphocholine (POPC) lipid bilayer using the VMD plug-in 'membrane', aligned to the *xy*-plane. The center of mass of the hydrophobic belt of α -hemolysin (residues 118-126 and 132-142) was aligned with the center of mass of the lipid bilayer. Lipid and water molecules overlapping the protein were removed. The system was solvated in a water box of pre-equilibrated TIP3P water molecules⁶⁹ using the VMD plug-in 'solvate' with a 2.4 \AA buffer distance applied between water molecules. The aqueous solution was set at 1 M NaCl using the VMD plug-in 'ionize'. The dimensions of the lipid membrane and water box were chosen to minimize interactions between periodic images of the molecules, due to the use of three-dimensional

periodic boundary conditions. The polynucleotide and peptide molecules were too large to simply insert into the constriction, therefore they were steered into the constriction after insertion into the α -hemolysin vestibule. The 25 base poly(dC) molecule was constructed using the AMBER module 'nucgen'.⁷⁰ A double stranded conformation of the nucleic acid polymer was first built, the coordinates of which were derived from fiber diffraction studies.⁷¹ A selected strand of the double helix was then removed from the PDB file, while the remaining single stranded nucleic acid polymer was charge neutralized with sodium counter-ions using the AMBER module 'xleap'.⁷⁰ The nucleic acid polymer was then orientated as necessary using the VMD module 'orient'⁷² and the molecule was inserted into the α -hemolysin vestibule with the C3'-carbon atom of the leading residue aligned with the center of the alpha carbon atoms of protein residue 111. The 7 unit arginine peptide was generated using 'Swiss PDB Viewer'⁷³ and inserted into the α -hemolysin vestibule alongside the polynucleotide. Water molecules that were overlapping the inserted polymers were removed. The leading atom of the arginine peptide was constrained to the z-axis position of the leading C3'-carbon of the polynucleotide using a strong adaptive biasing force, which acts to approximate a linker molecule connecting the two polymers.

The final model consisted of 328,000 atoms, while the dimensions of the simulation cell were 145 Å x 145 Å x 154 Å. Simulations were performed using the molecular dynamics simulation package NAMD version 2.6.⁶⁸ The CHARMM forcefield⁷⁴ was applied using all-hydrogen parameter files for CHARMM22 proteins and CHARMM27 lipids and nucleic acids. Periodic boundary conditions were applied and the Particle Mesh Ewald method⁷⁵ was used to calculate electrostatic forces with a dielectric constant of 1, computed over 128 Å x 128 Å x 128 Å grids. Van der Waals energies were calculated with a smooth 10 to 12 Å cut-off.

Constant temperature was maintained at 295 K using a Langevin thermostat.⁷⁶ Constant pressure was maintained by Nosé-Hoover Langevin piston pressure control at 1.01325 bar.⁷⁷ A 2 fs timestep was used, with SHAKE turned on. In order to eliminate high-energy atom clashes, models were energy minimized for 2 ps until the gradient tolerance was below 20. The temperature was raised by 5 K every 50 fs for 3 ps to a final temperature of 295 K. Prior to insertion of the polymers, the α -hemolysin model was equilibrated in the NpT ensemble for 1.3 ns with the backbone of the protein constrained, and for a further 4 ns without constraints. After insertion of the polymers, the model was equilibrated in the NpT ensemble for 4 ns with the alpha carbons of the protein constrained and the ribose unit's C3' atom of the leading residue of the nucleic acid molecule fixed. After the molecules were equilibrated, the polynucleotide was steered into the constriction using constant velocity-steered molecular dynamics, the peptide molecule was dragged along with it due to the adaptive biasing force constraint. Once the peptide molecule was half way through the constriction, the system was equilibrated for 4 ns. The average positions of the atoms in the model were calculated from an additional 4 ns equilibration, which was used to calculate the distances and conformations referred to in this chapter.

3.3.4 Data Analysis

The characteristic timescale τ_{off} for the events was obtained by plotting survival probability (P_{survival}) versus time. To extract the characteristic timescales, P_{survival} was fitted to the Becquerel decay function (from section 3.2) because a single-exponential decay gave a poor fit. The characteristic time (from section 3.2), τ^* is used as a parameter for kinetic analysis. Extracting τ^* from the fits to the dwell time distributions yielded plots of τ^* vs.

arginine tag length and applied potential. Plots of the survival function for each of the R_n-DNA molecules as well as the different fits are shown in Figure 3.3.2.

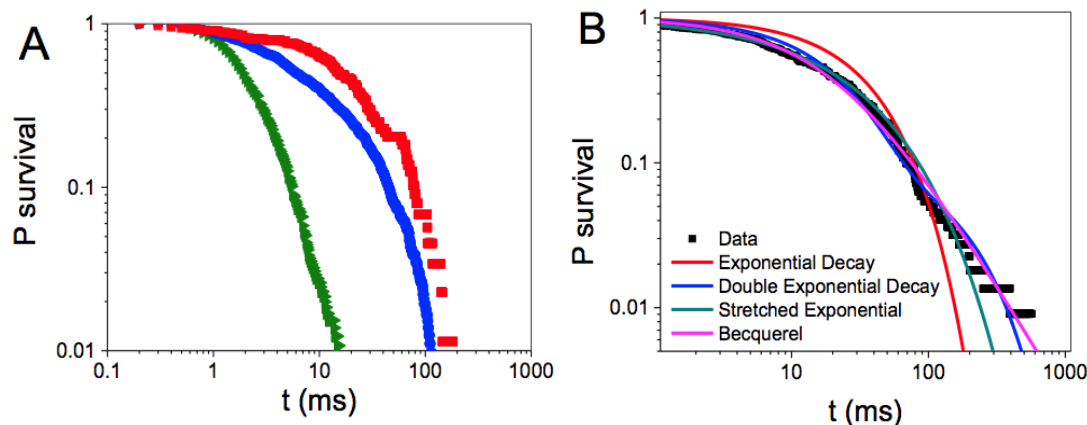


Figure 3.3.2 Survival function. (A) Event time distributions for R3-DNA (green triangles), R5-DNA (blue circles) and R7-DNA (red squares) at 100 mV. (B) Fits to the event time distribution for R7-DNA at 120 mV applied potential.

The biophysical model used was formulated and solved using Mathematica. The mathematical expression for τ^* was generated and then used to find the best fit to the entire R_n data set with the NonLinearModel fit function built into the Mathematica software. The values of electric charges for unmodified and modified parts of the DNA oligomer, q_1 and q_2 , respectively as well as the threading rate k_2 were found and used to calculate the resulting τ^* . Survival probability distributions were fitted to 5 different mathematical expressions using Mathematica's EstimatedDistribution function and the quality of the fits were compared. Using the most accurate fit, the Becquerel distribution, the characteristic time scale was then computed.

3.4 Results and Discussion

3.4.1 Modeling DNA-Peptide Molecules

Due to the fact that detailed experimental data is not available, molecular modeling of our synthesized DNA-peptide strand was performed prior to synthesis. The primary goal was to estimate the size and charge of the central region containing both peptide and ssDNA as it is threaded through the internal constriction of an α -hemolysin pore. Known X-ray coordinates for α -hemolysin were used and the structure of R7-DNA (27 nt ssDNA molecule

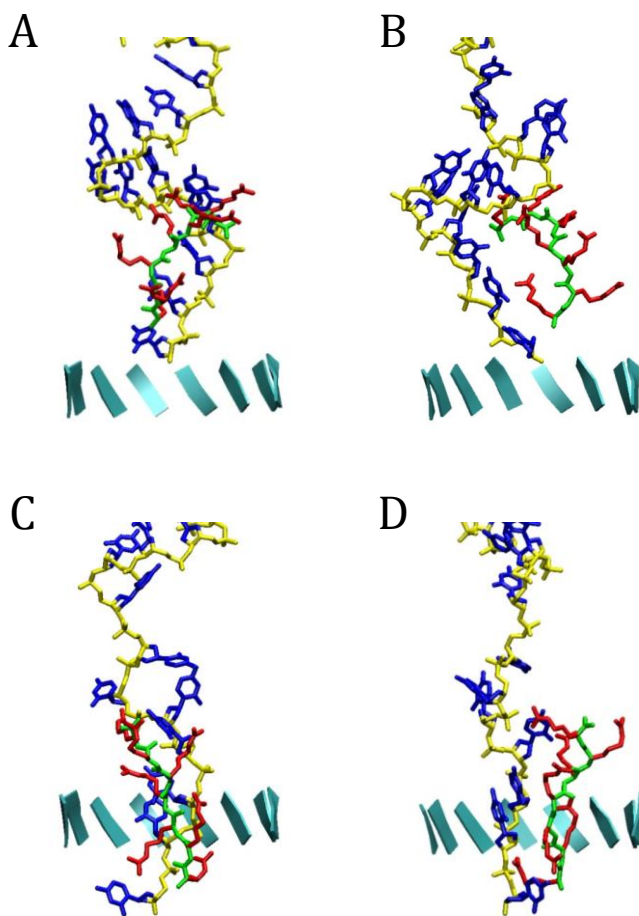


Figure 3.4.1 MD snapshots. Snap-shots of the computer simulations on the R7-DNA conjugate threaded inside the inner constriction of α HL. The conjugate was threaded into the pore via constant velocity-steered molecular dynamics simulations followed by equilibration for 4 ns to obtain an energetically representative structure. (A, B) snap shots for the pre-pulling state and (C, D) after pulling and 4 ns equilibration from two points of view differing by 90 °C. Teal-colored stripes represent residues 112, 113, 146 and 147, indicating the position of the constriction.

covalently bonded to seven residues of oligoarginine) was generated based on previously known monomer dimensions and results from molecular modeling software. It was found that the diameter of the molecule at the central region was 1.63 nm which is notably larger than the 1.3 nm diameter of the inner constriction found in α -hemolysin. Through adding an applied voltage the molecule was steered towards an α -hemolysin pore and was successfully threaded through the internal constriction. The results from this simulation are shown in Figure 3.4.1 as snapshots of the α -hemolysin while the translocation event is occurring. It was found that when inserted, the diameter of the arginine-DNA conjugate shrinks to 1.39 nm, which matches fairly closely the diameter of α -hemolysin. The model also provided an estimate of the charge on our molecule. When inside the constriction of α -hemolysin, the arginine peptide formed a helix structure with a pitch of 0.29 nm while the ssDNA maintained a larger pitch of 0.52 nm. Due to each having the same charge per residue, this resulted in a small net positive charge of 0.8e per DNA residue. From these simulations we conclude that our peptide-DNA conjugate will translocate through an α -hemolysin pore, but both the positive charge and increased diameter should reduce its movement speed. The control sample D₆-DNA was not directly modeled, but was assumed to have a similar diameter as the arginine, with a negative charge.

3.4.2 Verification of DNA-Peptide Modification

In order to make sure that the ssDNA molecules were successfully modified, a two step method was used. First, anion exchange high performance liquid chromatography (AE-HPLC) purification was done on the sample following the modification step. In AE-HPLC, the solid phase is positively charged which will cause negatively charged molecules to travel

through the column at a slower rate, increasing the retention time. As a result, it is expected that the most negative molecule, D₆-DNA, will correspond to the longest elution time, while the R₇-DNA has the smallest. Taking advantage of known ultra-violet absorption wavelength of DNA, 260 nm, spectroscopy can be done to detect the exit of the peptide-ssDNA molecules from the column.⁷⁸ The results are shown in Figure 3.4.2 with the y-axis showing absorption percentage and the x-axis showing elution volume. Although it is labeled on the figure, it is important to note that at this point in analysis, it is not known which peak corresponds to which molecule.

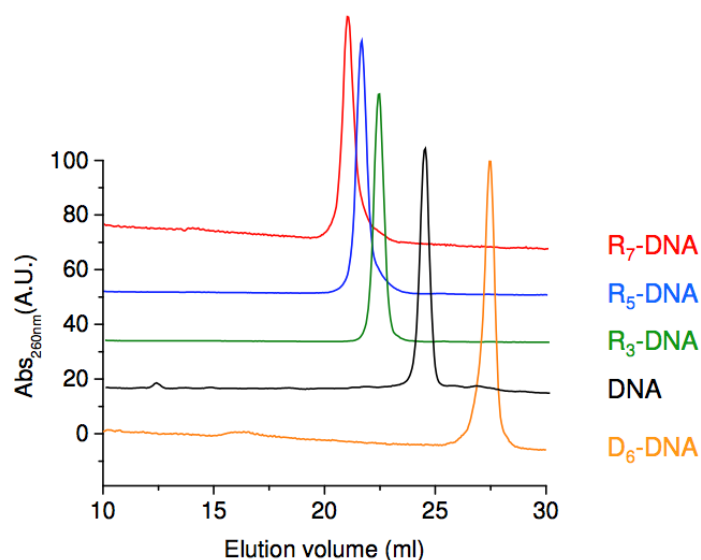


Figure 3.4.2 HPLC traces. Traces from AE-HPLC for non-modified and R₃-DNA, R₅-DNA, R₇-DNA and D₆-DNA. Elution volume and therefore molecule net charge can be seen to follow the expected order based on the peptide modification done, providing evidence of successful peptide-DNA conjugation.

In order to identify the output of AE-HPLC, mass spectroscopy (MS) was done on the now purified samples. Through ionizing the sample, accelerating it through an electromagnetic field, and measuring the deflection, the ratio of mass to charge (m/z) can be found. Samples containing both the peptide alone and the peptide-DNA conjugates were sent

through the MS step, allowing for a direct comparison of the two. Based on the known structure of the peptides and ssDNA used, a theoretical m/z ratio can be calculated and compared against the values found experimentally. The evidence of successful modification is then threefold. First, it can be seen in Table 3.4.1, which summarized the characterization results, that the experimental and theoretical m/z values match very well for all molecules. Second, with the identification of each molecule through MS, it is now possible to return to Figure 3.4.2 and label each peak. As expected, the samples exit the column in order of net charge accounting for the peptide modification. Finally, the HPLC retention times for a peptide and the corresponding peptide-DNA conjugate can be compared with a proper shift

Name	Oligo-nucleo-tide ^[a]	Peptide				Oligonucleotide-Peptide-Conjugate		
		Sequence ^[b]	Mass [m/z] ^[c]		HPLC retention time [min] ^[d]	Mass [m/z] ^[e]		AEC retention time [min] / purity [%] ^[f]
			Theory	Found		Theory	Found	
DNA	27	n.a.	n.a.	n.a.	n.a.	8380.6	8379.4	25.5 / 99
DNA-D ₆	27	G ₁ D ₆ G ₁ C ₁	925.21	926.15	11.5	9391.8	9401.2	27.45 / 99
DNA-R ₇	27	G ₁ R ₇ C ₁	1271.52	636.55 ^[g]	13.1 ^[h]	9738.6	9737.9	21.3 / 99
DNA-R ₅	27	G ₁ R ₅ C ₁	959.15	480.48 ^[g]	12.5	9426.2	- ^[i]	21.8 / 90
DNA-R ₃	27	G ₁ R ₃ C ₁	646.8	647.49	11.5	9113.9	- ^[i]	22.5 / 96

Table 3.4.1 HPLC and MS Summary. Summary of the AE-HPLC and MS characterization that was done to insure successful peptide-DNA modification. Samples were first subjected to AE-HPLC for purification followed by MS for characterization. The ratio of m/z for the peptide alone and peptide-DNA conjugate matches the theoretical value in all cases. Successful modification is also suggested by the shift in AE-HPLC retention time which is dependent on the specific peptide modification done.

indicating successful modification. As an additional control, the purity of each sample is calculated during the MS step, ensuring that the purification step was successful and the MS results are accurate.

3.4.3 Peptide Modified DNA Translocation Produces Closure Events

Before DNA-peptide molecules were added to the system, single α -hemolysin pores were characterized to get a baseline current. It was found that over four independent measurements, the conductance of a single pore was 1.93 ± 0.19 nS which matches what is recorded in the literature at 100 mV in a solution of 2 M KCl, 12 mM MgCl₂ and 5 mM Tris-HCl (pH 7.4).¹⁸ Following this control test, the arginine modified DNA strands, with 3, 5 and 7 residues and the DNA attached to 6 residues of aspartate were added to the *cis* side of the pore and driven towards the other side via an applied voltage between 100 and 180 mV. Clear high amplitude current blockades were then observed. Various event types and behaviors were recorded, which will be elaborated on below. We believe that the majority of these events correlate to individual ssDNA-peptide molecules passing through the α -hemolysin pore.

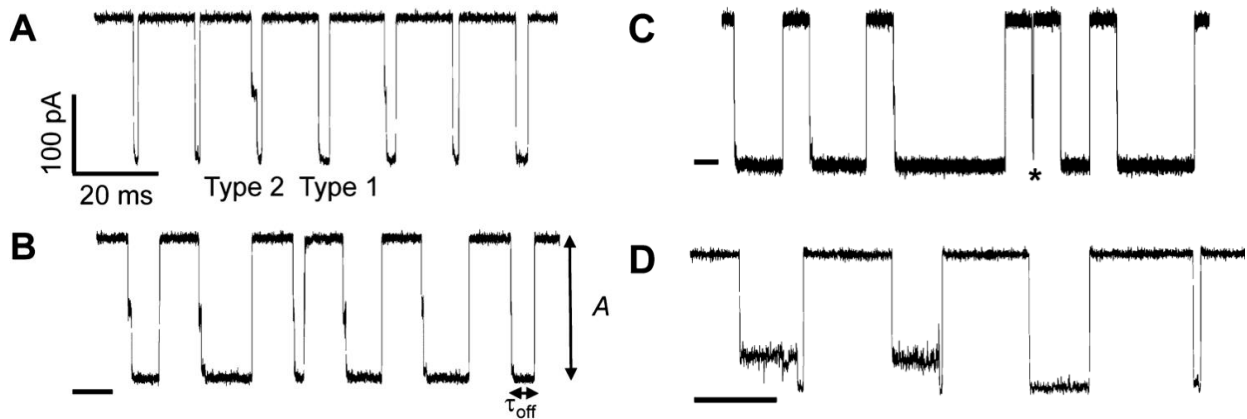


Figure 3.4.3 Event traces. Representative single-channel recordings of aHL with (A) R₃-DNA (B) R₅-DNA (C) R₇-DNA and (D) D₆-DNA at 100 mV in 2 M KCl 20 mM Tris, pH 8 solution. Intermittent stretches with open channel current are omitted.

Figure 3.4.3 shows the several different types of events that were observed. The first and simplest event type (type 1) is a step like current reduction with a single level. The current reduction from these events was almost complete with an all-point histogram producing the values given in the table below.

Molecule Type	Blockade Amplitude (%)
R3-DNA	98.2 ± 0.5
R5-DNA	98.7 ± 0.5
R7-DNA	99.3 ± 0.4
D6-DNA	97.4 ± 1.43

Table 3.4.2 Blockade amplitude. Summary showing the percentage of current reduction resulting from the blockade of the pore by different peptide-DNA molecules.

The shape and magnitude of these events most likely suggests that they are generated by DNA-peptide molecules which are aligned in parallel before being electrophoretically driven towards the *trans* side of the α -hemolysin pore. The immediate blockade suggests that the molecule is quickly threaded into the internal constriction and once through, quickly leaves the pore. The near 100% reduction in current for each event also suggest that they are due to translocation through the internal constriction, based on the model generated size estimates from the previous section. It is also reassuring that the current blockades were larger than those seen in unmodified ssDNA molecules (91.7%)⁵⁹ supporting the claim that our peptide modifications successfully increase the diameter of ssDNA.

The second most common type of event was characterized as having two current levels, an initial partial blockade state, followed by a complete closure similar to that seen in type 1 events. We believe that this may be caused by strands being misfolded as they enter the α -hemolysin pore. This results in them occupying the larger pore entrance for some time

before successfully being threaded into the inner constriction where they produce a complete blockade. As evidence of this is the fact that the final current reduction in type 2 events matches the single current reduction of type 1 events. Additionally, the partial blockade state was only ever observed to occur before the full closure and not after which would be expected in this case.

The final type of event was much shorter than the previous two events and an example can be seen in Figure 3.4.3 part C, identified with the asterisks. We believe that these events represent approaches of DNA-peptide molecules towards the α -hemolysin pore that did not result in translocation. This is based on the much shorter duration of these events and the more seemingly varied amplitude. An alternative explanation could be that these events represent ssDNA molecules which were not successfully modified with a peptide chain. If this is the case however, it would be expected that the events would be consistent with an event depth matching previous experiments. These types of events were rare, with roughly 98% of all events being long duration, so collecting useful statistics was not possible. Regardless of the cause for different event types, they were not included in the analysis presented in the rest of this chapter. We restricted examination to type 1 events in order to help eliminate unknowns and to provide more accurate data analysis.

3.4.4 Trends in Translocation Time

In order to look at how peptide modification impacts translocation time, the characteristic duration of type 1 events was studied. As described in section 3.2 of this chapter, this was done through analyzing roughly 2500 events at each condition and fitting to a Becquerel decay function. The characteristic average time τ^* was then found and is

plotted. From the results there are several conclusions that can be drawn, specifically regarding how τ^* depends on both steric and electrostatic effects.

The first relationship that can be observed is between peptide tag length and characteristic translocation time. At 100 mV τ^* for R₃-DNA, R₅-DNA and R₇-DNA was found to be 2.4 ± 0.3 , 10.9 ± 1.2 , and 19.1 ± 7.8 ms, respectively. Figure 3.4.4 part A shows similar data plotted at a voltage of 140 mV (ignoring the black line for now). The first thing this suggests is that the modified ssDNA is in fact passing entirely through the pore. If this were not the case, a much weaker dependence, if present at all, would be expected as the entirety of the modification would potentially never see the internal constriction of the pore. Next, it is clear that the tags themselves are in fact slowing down the translocation of the molecules they are attached too. When compared to unmodified ssDNA of similar length, which has a translocation time of about 0.12 ms⁵⁹, the durations seen in modified strands are one to two orders of magnitude larger. Additionally, we can clearly see that as arginine tag length increases, so does translocation time. This is as expected, but the root cause, electrostatics vs sterics, is not yet clear.

The first potential cause of longer duration events stem from electrostatic effects. Due the relative size of α -hemolysin's internal constriction, the majority of an applied voltage will be concentrated across it. As a particle is threaded in, this effect is further enhanced due to the decreased effective pore size. What this means is that the electrostatic force on a translocating molecule will be greatly affected by the charges located in the internal constriction. In the case of the arginine modified DNA, the net positive charge can even result in a force pushing against the translocation direction which acts on the modified region. This effect is verified through comparison of the R₅-DNA and the D₆-DNA conjugates. Despite

having similar size and structure, the D₆-DNA conjugate, which retains its negative charge at all points along the strand, had a translocation time of 2.0 ± 0.2 ms. This is almost an order of magnitude higher than the value give for the R₅-DNA.

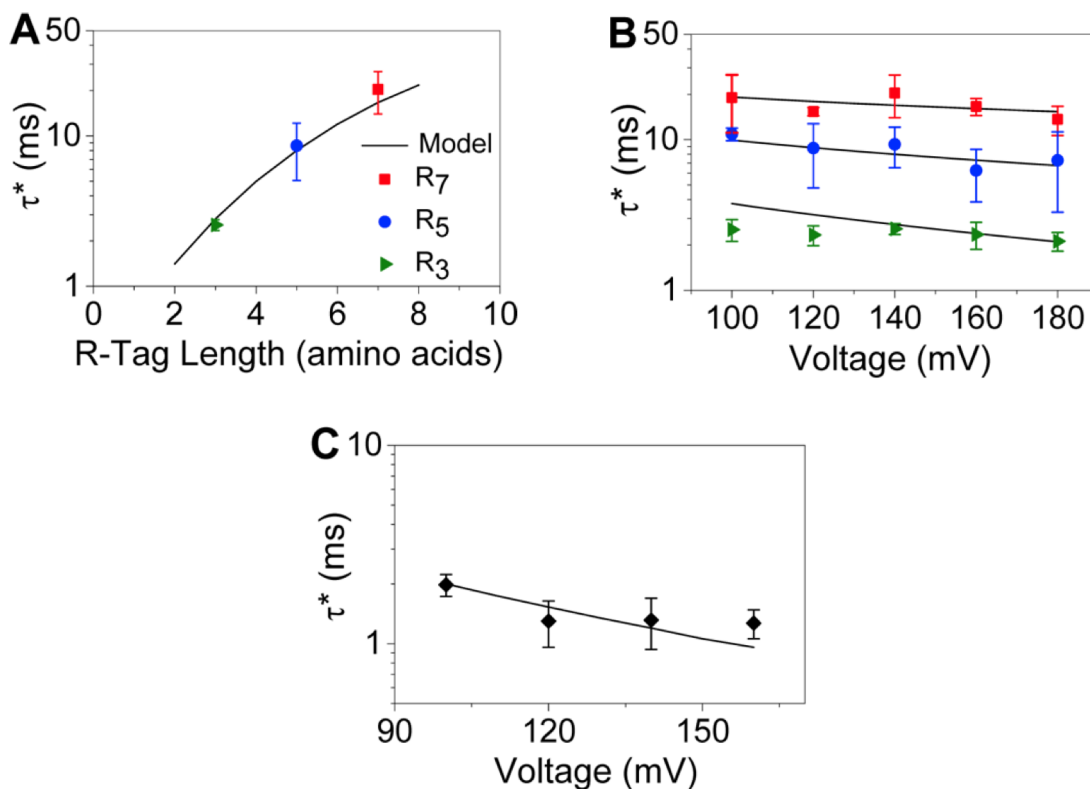


Figure 3.4.4 τ^* vs voltage. Quantitative analysis of pore translocation for DNA-peptide conjugates. Plots show experimental data points and fits for τ^* , the dominant characteristic time scales of the Becquerel decay function. Characteristic time scales for translocation of (A) the R_n-tag as a function of arginine tag length at 140 mV, and (B) for R₃-DNA (green triangles), R₅-DNA (blue circles), and R₇-DNA (red squares), as a function of applied potential, and (C) for D₆-DNA as a function of applied voltage. Error bars are calculated as the average standard deviation in τ^* obtained from three or more independent experiments at each voltage with the exception of data points for R₅-DNA at 120 and 180 mV with two recordings but with an above-average total number of 2598 and 3145 events, respectively. The fits are derived from the biophysical model and provide the parameters of $q_1 = 0.31$, $q_2 = -0.013$, $k_1 = 1387\text{s}^{-1}$, $k_0 = 10_5\text{s}^{-1}$ for data in panels A and B, and $q_2 = 0.48$ for data in panel C.

The second source of slowed movement through α -hemolysin is due to the steric effects caused by the modifications to the ssDNA. The increase in diameter should slow down the movement speed and this is what is seen in the data. This is most easily observed by comparing D₆-DNA data to that of unmodified ssDNA. The order of magnitude increase

in translocation time of the D₆-DNA over ssDNA makes it clear that charge is not the only factor at play. This must be the case considering that the D₆-DNA actually has an increased negative charge compared to its unmodified counterpart. Steric hindrance, then, is the most likely cause of this behavioral difference.

Final trends can be seen in the data when the plot is expanded to include characteristic translocation time as a function of voltage. This is shown in Figure 3.4.4 part B for all three arginine tag lengths. The first observation is that the previously mentioned trend of tag length influencing event duration continues across all voltages. This is expected, as both steric and electrostatic effects remain present as voltage is modulated. The second noteworthy trend is that as voltage increases, translocation time decreases for ssDNA attached to all modifications. Since the primary force driving translocation is electrophoretic in nature, this trend is also expected. As applied voltage is increased, the driving force is increased with it. The strength of this effect is very weak however, indicating other effects might play a larger role over the electrostatic driving force.

3.4.5 Formulation of a Biophysical Model

In order to further probe the relative importance between steric and electrostatic effects, a biophysical model was developed to describe the passage of our modified ssDNA strands through an α -hemolysin pore. Our model was based on the previous approach of Schink et al.⁷⁹ and modified to give τ^* of our system as a function of applied voltage and aspartate/arginine tag length. This is done through first describing our modified ssDNA with charge distributions and size dependent movement rates. Then, the free energy landscape of a molecule undergoing translocation is calculated. Following this, so called hopping rates

are applied to the forward and reverse movement of the peptide-DNA conjugate which in turn lead to a predicted τ^* value. This process is summarized in Figure 3.4.5 below and will be elaborated on in the next paragraphs.

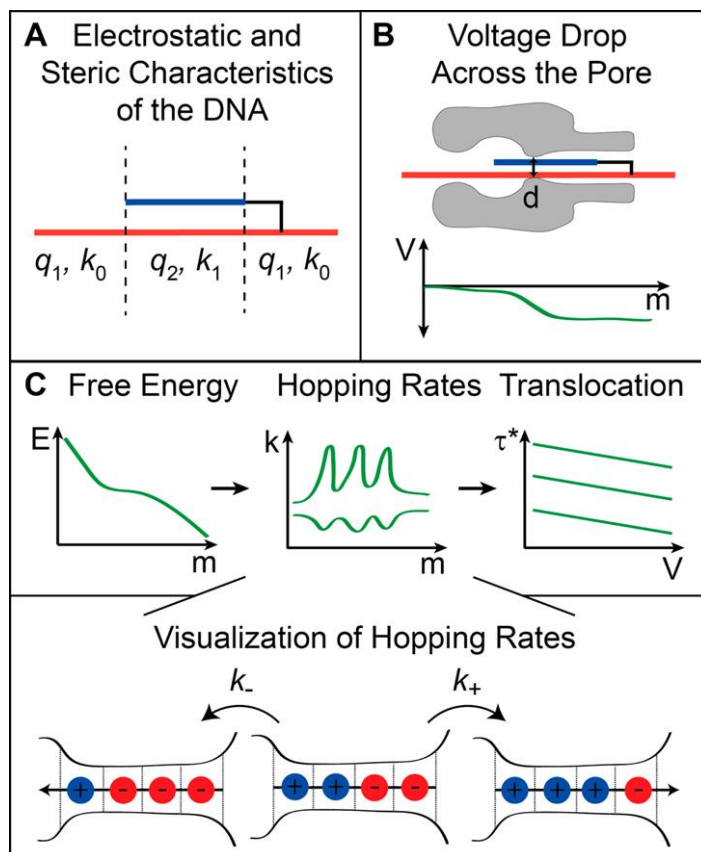


Figure 3.4.5 Biophysical Model. Scheme illustrating our biophysical model. (A) The charge and steric features are defined. (B) The voltage drop across the pore is assumed to be linear. (C) The free energy is calculated which provides the hopping rates which in turn provide the translocation time. Bottom row shows an illustration of the hopping rates.

The first step in this process is to accurately describe the differently modified ssDNA molecules used in the study. This is most easily done by characterizing the charge along the DNA strand, given by q , and the stochastic motion the DNA strand, given by the hopping rates k . Each molecule is best described piecewise, as a function of nucleotide position, m (m specifies how many nucleotides have entered the pore). The two ends on either side of each strand have the characteristics of unmodified ssDNA, specifically a charge expressed as the

electron charge, e , times the partial charge constant, q_1 as well as the known basal hopping rate of ssDNA in an α -hemolysin pore, k_0 ($\sim 10^{-5} \text{ s}^{-1}$).⁵³ The central modified regions will be similarly written as having a charge of q_2 multiplied by e and be assigned a hopping rate of k_1 , which will be smaller than k_0 due to the added steric effect. The complete equation for $q(m)$ is given by

$$q(m) = \begin{cases} q_1 e & m < 18 \\ q_2 e & 18 \leq m < (17 + R) \\ q_1 e & m > (17 + R) \end{cases} \quad (3.4.1)$$

and the expression for $k(m)$ is given below.

$$k(m) = \begin{cases} k_0 & m < 18 \\ k_1 & 18 \leq m < (17 + R) \\ k_0 & m > (17 + R) \end{cases} \quad (3.4.2)$$

In this equation, $m = 1$ refers to the first nucleotide having entered the inner constriction and m can be any value between 1 and 27 (the full length of our ssDNA). To best match our synthesized molecules, the modified region begins at nucleotide 18. This is not the same location as the covalent bond adhering the peptide modification because we will treat the linker as negligible due to its relatively small size.

Once the ssDNA molecules are accurately described, it is possible to calculate the free energy landscape associated with the ssDNA moving through an α -hemolysin pore. The free energy function, $F(m)$, will again be piecewise due to the three regions of our translocating molecule. This function $F(m)$ will be the sum of three terms including the applied voltage (F_{voltage}), total number of possible DNA configurations (F_{conf}), and the energy of the DNA binding to itself (F_{fold}). The second term, F_{conf} , was shown to be at least two orders of magnitude lower than F_{voltage} for unfolded ssDNA⁸⁰ and as such will be negligible in our system. The third term, F_{fold} , turns out to also be negligible due to the design of our ssDNA

nucleotide sequence. This factor is depended on the number the complimentary nucleotides that can interact with each other along the same strand of ssDNA. There are many online tools, such as Oligo Analyzer (Integrated DNA Technologies), which can calculate the energy of varies sequence dependent structures. For our sequence, the most likely conformation has a G value of 0.93 kcal per mol, which is small enough to ignore. This leaves us with the following function for $F(m)$ which is calculated by summing the energy of each charged segment, m , of our ssDNA molecule moving in a potential.

$$F(m) = \begin{cases} \sum_{l=0}^{m-1} V(l)q(m-1) & m \leq L \\ V \sum_{l=1}^{m-L} q(l) + \sum_{l=0}^{L-1} V(l)q(m-l) & L \leq m < 27 \\ V \sum_{l=1}^{m-L} q(l) + \sum_{l=m-27}^{L-1} V(l)q(m-l) & m > 27 \end{cases} \quad (3.4.3)$$

It is assumed that the entirety of the voltage is dropped over the inner constriction and that it is done so linearly. This results in the following expression for V

$$V(m) = V_0 \frac{m+1}{L+1} \quad (3.4.4)$$

where the length of the inner constriction is then given by L and a value of 4 is used to best match the structure of our pore.

It is next required that the position dependent hopping rates we written out. As previously mentioned, these functions represent the likelihood that our ssDNA will shift either forward (+) or backwards (-) by one value of m . Following the lead of Schink et al. we take the form of our hopping rates to be exponential, with their full equations being given as a function of m below.⁷⁹

$$\begin{aligned}
k_+ &= k(m)e^{-\alpha\Delta(m+1)} \\
k_- &= k(m)e^{-(1-\alpha)\Delta(m+1)}
\end{aligned}
\tag{3.4.5}$$

The term $\Delta(m)$ is defined as the energy difference between two consecutive states and is given by the following.

$$\Delta(m) = \frac{F(m) - F(m - 1)}{k_B t}
\tag{3.4.6}$$

The variable α in the Equation 3.4.5 is included because there may be asymmetry present in the physical transition point between two successive values of m stemming from the structure of ssDNA. It has been shown that for ssDNA a value of α equal to 0.6 is appropriate for translocation in the 5' to 3' direction.⁸¹

We are now in a position to use the first passage formulation developed in the theory section of this chapter. Our system is described very well by the model presented there, and we are able to use the resulting equation for the average translocation time of our ssDNA through the pore. The above equations describing the free energy of the system can be fed into the expression for the hopping rates, which in turn can be inserted into the final equation (3.2.15) predicting the average translocation time.

3.4.6 Disentangling Steric and Electrostatic Factors

Before the presented biophysical model can be used to extrapolate the relative importance of steric vs electrostatics effects, it is important to see how well it describes our data. This was done by first writing out the equation for translocation time as a function of k_0 , k_1 , q_1 , q_2 and V , then fitting to the entire data set, over all voltages and tags, in order to find best fit values for k_1 , q_1 , and q_2 . Since the value of k_0 is known, it was held as a constant. The results from this fit are shown by the black lines in Figure 3.4.4 and the fit was of high

quality for the majority of the data set with an overall correlation coefficient, R^2 , of 0.98. The fit matched best for R_5 -DNA and R_7 -DNA with worse fit for the R_3 -DNA, especially at low voltages. This may be related to other interactions between the ssDNA and the pore and is discussed later in this section.

Table 3.4.3 shows a summary of the best fit parameters found using our model, for unmodified ssDNA, R_n -DNA and D_6 -DNA. All of the parameter values are in good agreement with the expectations. Starting with the charge on the unmodified ssDNA segments, q_1 , we get a value of 0.31 which matches previously published data which is in the range of 0.1 to 0.4.⁵³ When looking at the R_n -DNA data set, the charge on the modified region, q_2 , is found to be -0.013. Keeping in mind that the total charge still requires a factor of e , this value also makes sense. From the computational simulations we predicted that the arginine modified ssDNA would have a small positive charge, which matches to our q_2 value. The best fit parameters for the D_6 -DNA, on the other hand, resulted in a q_2 value of 0.48. This value is the correct sign, and it is larger than that found on unmodified ssDNA, which again matches expectation. Lastly, the parameter k_1 was found to have a value of 1387. It is more difficult to evaluate the quality of this value due to a lack of comparable studies in the literature. What can be said is that this value is many orders of magnitude smaller than that of ssDNA inside α -hemolysin which is a trend in the correct direction. The increased diameter of the modified ssDNA will increase steric hindrance and therefore lower the rate of hopping, translating to a lower value of k_1 . As a whole, the results of the model suggest that it describes our system accurately enough that it can be used to gain insights on the relative importance of the different aspects governing transport.

DNA	R#-DNA	D#-DNA
$q_1 = .31e$	$q_1 = .31e$	$q_1 = .31e$
$q_2 = .31e$	$q_2 = -.013e$	$q_2 = .48e$
$k_1 = 10^5$	$k_1 = 10^5$	$k_1 = 10^5$
$k_2 = 10^5$	$k_2 = 1387$	$k_2 = 1387$

Table 3.4.3 Fit parameters. Fit-parameters for the biophysical model of nanopore translocation for unmodified, arginine-modified and aspartate-modified DNA.

Attempts to use our model without either the steric or electrostatic components resulted in relatively poor fits in all cases. For example, R₅-DNA at 160 mV has an experimental translocation time of about 8 ms and this value is correctly predicted when the complete model is used. If the steric effects of the modification are removed from the equation, by setting k_1 equal to k_0 , the predicted translocation time is only 0.2 ms. If the same type of calculation is done, except this time only the electrostatic effects are ignored, which can be done by setting q_2 equal to q_1 , the predicted duration is 1.5 ms. As a control test, if both steric and electrostatic effects of the modification are ignored, a translocation time of 0.1 ms is predicted, which matches experimental results using ssDNA.⁵⁹ In both cases where only one factor is included, the model inadequately describes the system making it clear that the combination of both effects are required. Additionally, the error given by each method provides some small insight into the relative importance of each effect and makes it clear that there is some amount of interplay between the mechanisms.

3.5 Conclusion

To summarize, this chapter has presented the transport behavior of ssDNA locally modified to alter charge and diameter characteristics. Through molecular simulations and experimental data, it was found that the additions of peptides to the central region of ssDNA molecules dramatically slowed down the translocation rate through an α -hemolysin pore. In order to explain this behavior, a biophysical model was constructed which incorporates both electrostatic and steric based effects. The resulting parameters and the quality of the best fit analysis against our experimental data validate its use. We conclude that both steric and electrostatic effects are required for accurate predictions of the translocation time, and provide some insight into the relative importance of each.

The work in this chapter has been done with certain simplifying assumptions. The first is that the voltage was assumed to drop off linear across the central restriction of the α -hemolysin pore. In reality, this is dependent of the specific channel characteristics as well as surrounding areas. The known structure of α -hemolysin makes a more accurate representation of the voltage possible, but would require additional computing power and time. The second assumption is that only steric and electrostatic effects were considered in the biophysical model. It is known that there are other forces at play such as interactions between the pore wall and the ssDNA. At large voltages, and long tag lengths, these factors may be not play a large role, but as voltage and tag length decreases their relative importance increases. This may explain why the fit of our model seems to be lower quality at low voltages and short tag lengths. Finally, our model does not include any effects due to electroosmotic flow which can sometimes be important in determining DNA translocation

kinetics.^{82,83} In the case of this work however, the majority of the channel was blocked during translocation reducing the possible amount of electroosmotic flow.

In the larger picture, we aim to help with understanding how the speed of translocation can be tuned to best fit the application. Many current technologies, such as those used for high speed DNA sequencing suffer from low signal to noise ratios, making data analysis difficult. Techniques like the one proposed here could be used to slow transport down and improve accuracy. Additionally, our methods can be applied to any type of molecule or pore through substitution of a few equations, such as the hopping rates or free energy. As technologies based on nanopore sensing continue to develop and push current boundaries the ability to carefully monitor and tune transport behavior will be required, which in turn, requires the use of an accurate physical model.

Chapter 4: Making Nanopore Gates from Polymer Pores and DNA

4.1 Introduction

Biological nanopores found throughout nature often have the capability to respond to stimuli in the surrounding environment. This is possible because changes in conditions such as voltage, pH, light, temperature and mechanical stress, have the potential to trigger a significant difference in a pore's transport properties.³ The underlying mechanics of this behavior have mostly remained a mystery until the development of recent laboratory techniques, such as X-ray crystallography and patch clamps, which allow individual pores to be isolated and examined. While we have gleaned significant information on the mechanisms governing pore gating, it has been found that these ion channels often have incredibly complex structures. This has made it very difficult to identify which elements of the design are required for pore function and exactly how they work. An alternative route towards this end is the use of synthetic nanopores as model systems which we can directly manipulate at test. This provides a platform which can be built and studied from the ground up, as opposed to the top down methods used for biological pores.

In order to create synthetic nanopores on par with those seen in nature, we have to start with something simple. One logical point of origin is with synthetic pores such as those made in polymer or SiN membranes. There are several methods used to fabricate these types of pores, some of the most popular using the track etch technique, e-beam lithography/TEM and focused ion beam technology, and they produce simple and robust pore designs.²⁰ Alone, these pores generally do not show strong stimuli induced gating behavior (in some cases charged based ion selectivity is present), but they provide a scaffold to which modifications

can be applied. Through careful design, researchers have been able to tune their behavior to partially mimic that of their biological counterparts. In the case of pH and voltage response, a common trigger for natural pores, gating is typically achieved through a nanomechanical change which can alter the pore's internal diameter, exposed surface chemistry and channel shape.³ One way this mechanism has been replicated, using solid-state nanopores, is through the attachment of molecules to the pores opening and/or inner walls. These modifications can then interact with the pore transport properties through steric and electrostatic effects. Pores that have been fabricated in this way have successfully shown some gating behavior in response to individual changes in pH or voltage.

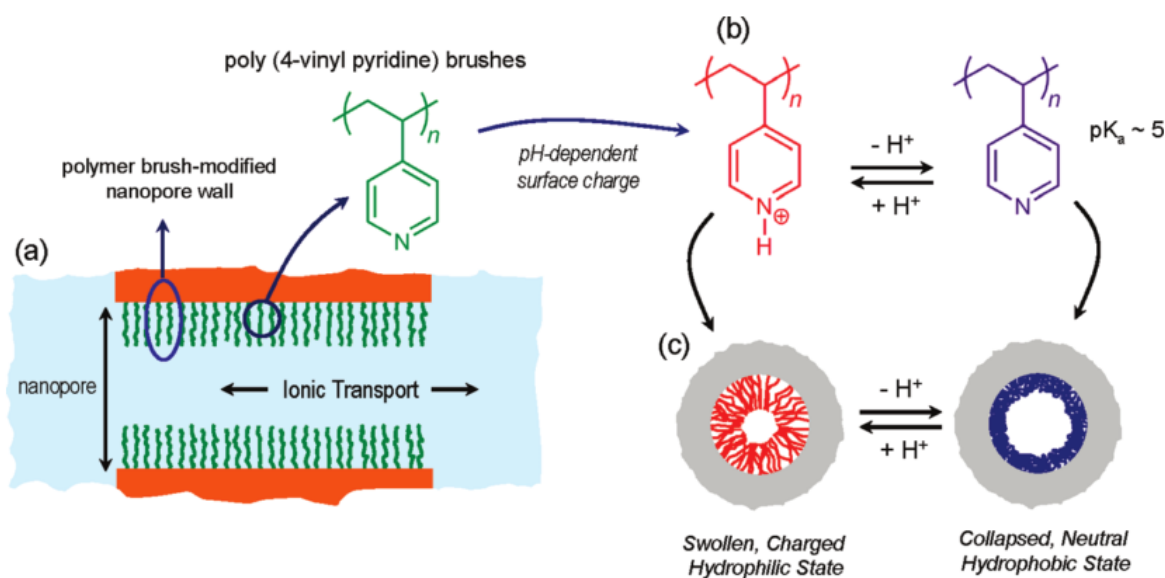


Figure 4.1.1 Polymer brushes. (a) Schematic describing a nanochannels modified with polymer brushes. (b) pH dependent pyridine-pyridinium equilibrium occurring in brushes. (c) Conformational changes in the brush layer resulting from a change in the pH. Reprinted with permission from Yameen et al.⁸⁵ Copyright 2009, American Chemical Society.

Synthetic pores that show a pH or voltage response have been created in a few different ways but they all follow the above template. One example was fabricated using a 20 nm diameter (tip side) track etched conical nanopore in a polyimide membrane.⁸⁴ The pore was then modified such that zwitterionic polymer brushes could be grown on the

interior pore walls. As the pH was changed, these brushes would effectively alter the surface charge of the pore wall influencing the transport properties, namely ion rectification. This work was expanded on by altering the polymer brushes so that as pH values increased, they would become swollen and more hydrophilic (shown in Figure 4.1.1).⁸⁵ Cylindrical pores 15 nm in diameter modified with these brushes showed a 10 fold decrease in conductance when in the closed state. A somewhat different approach was taken by Charles Martin's group and used tracked etched polycarbonate pores with sub 60 nm tip diameters modified with ssDNA to achieve gating behavior.⁸⁶ The ssDNA was attached to the tip side of the conical pore and acted as a voltage sensitive mechanical gate due to its high charge, a schematic is shown in Figure 4.1.2. The steric effects of the applied voltage pulling on the DNA strands resulted in a rectification value of 11.5, showing that both methods produced similar gating magnitudes.

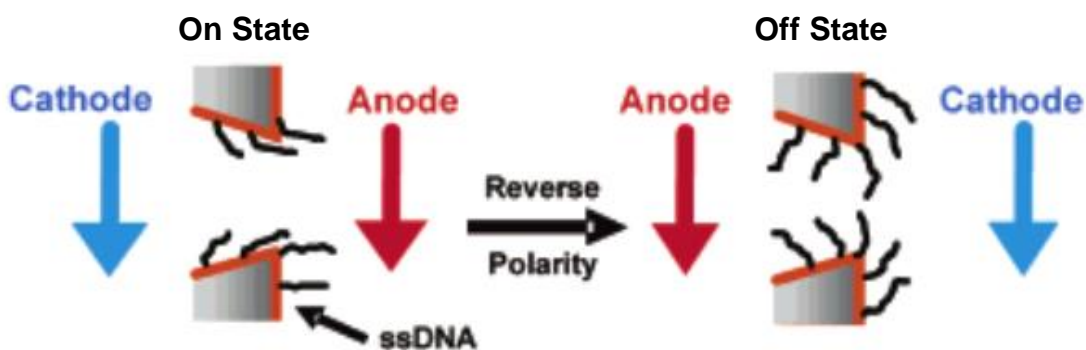


Figure 4.1.2 DNA gate. Schematic of a polymer pore modified with DNA attachments to the pore wall. The electrode polarity and DNA chain position of two different conductive states are shown. Reprinted with permission from Harrell et al.⁸⁶ Copyright 2004, American Chemical Society.

The work in this chapter will build on the idea of using ssDNA as a tool to modify polymer nanopores in order to improve their gating characteristics. We aim to create a synthetic nanopore which can respond to multiple stimuli at once, including pH and voltage, similar to biological pores. We also will show that our pore design results in flux changes between open and closed states that are significantly more dramatic than one order of

magnitude. While there is still a long way to go before biomimetic synthetic nanopores can compete with those found in nature, the work here is an important step to achieving that goal.

4.2 Theory

4.2.1 Track Etch Technique

The track etch technique consists of two fundamental steps, which as the name implies, include the formation of a track and then the etching of it. To create the track a specific path through the material is modified in some way. The material is subsequently subjected to an etching step, which impacts the unmodified material differently than the area where the track was formed. Although track etching is a technique used in a wide variety of applications,^{87,88} the discussion here will be focused on its use in fabricating nanochannels in polymer membranes. In this context, the base material is a thin polymer membrane and the track passes from one side to the other. During the etching step, the material along the track is removed, resulting in a void, which becomes the nanopore. The pores prepared in this chapter were etched in polyethylene terephthalate (PET) films.

In order to create a track through a polymer film, a particle accelerator is utilized. The membrane is suspended in place and irradiated with anywhere from a single, to 10^{10} heavy energetic ions. Accelerated ions used in this study include gold, xenon and uranium, and are referred to as heavy due to having an atomic mass significantly larger than the hydrogen, carbon and oxygen atoms that make up the polymer matrix. They are described as energetic due to having an energy of around 2 GeV, which is sufficient for them to pass entirely through a 12 μm PET membrane. As these ions pass through a film, they transfer

energy from themselves to the atoms along their path. This results in a latent track of damage that will change the etching characteristics along the path during the later fabrication steps.

The details behind exactly how these accelerated heavy ions transfer their energy to the atoms in the polymer films is still up for some debate. There are two current theories which represent this process, the first of which is called the thermal spike model. In this model, as the imparted ion passes through the polymer, it promotes electrons in nearby atoms thereby transferring thermal energy to them. This results in so called “hot” atoms

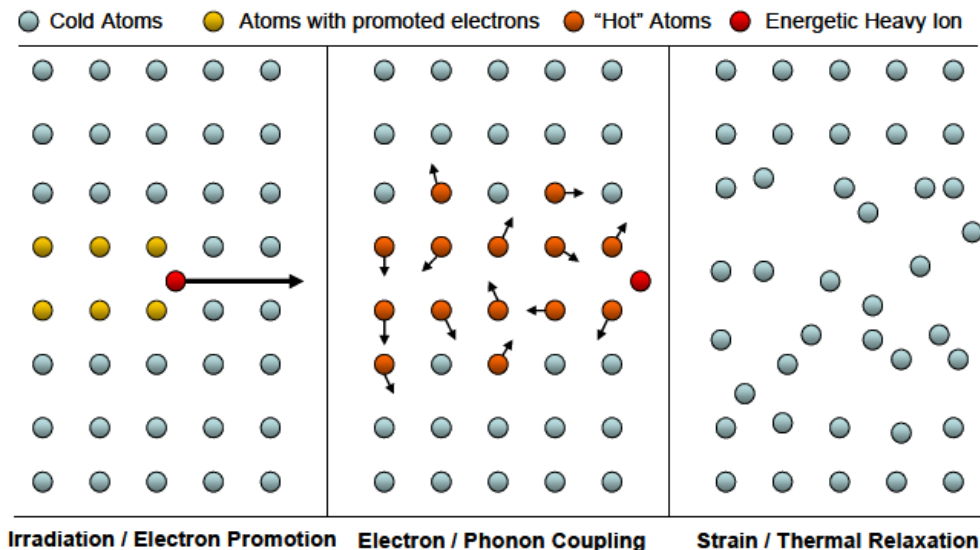


Figure 4.2.1 Thermal spike model. Diagram showing the thermal spike model for latent track formation. Atoms near the imparted heavy ion have their electrons excited, resulting in thermal fluctuations. This energy quickly leaves the system freezing the atoms in a disorganized structure. Figure courtesy of Eric Kalman.²⁸

which temporarily have enough energy to overcome neighboring bonds and shift in position.

These atoms quickly cool back down to normal temperatures and become stuck in their new

locations. The end result is a track of disorganized atoms along the path traveled by the

imparted heavy ion. An illustration of this model is shown in Figure 4.2.1. The alternate

theory is called the ionization spike model and is similar in that energy is transferred from

the accelerated ion to the atoms in the polymer matrix. The difference is that in this model, the energy transfer ionizes the polymer atoms stripping away their electrons and giving them a positive net charge. These atoms then electrostatically repel each other, once again resulting in a damaged track as seen by Figure 4.2.2. Both models are plausible and not mutually exclusive so it is likely that the true cause of the damaged track is a combination of the two. A study using TEM based techniques to answer this question, among others, observed evidence suggesting both effects are indeed occurring.⁸⁹ Once formed, this latent track is very stable and films prepared in this way can be stored or shipped without much worry of causing damage.

Once the creation of the track is complete, the samples are ready for wet chemical etching. The PET films used here are etched through hydrolysis of the ester bonds in the polyester chains. This can be achieved through the use of almost any alkali solution but the one selected for this work was sodium hydroxide (NaOH). Both the etching rate of bulk PET,

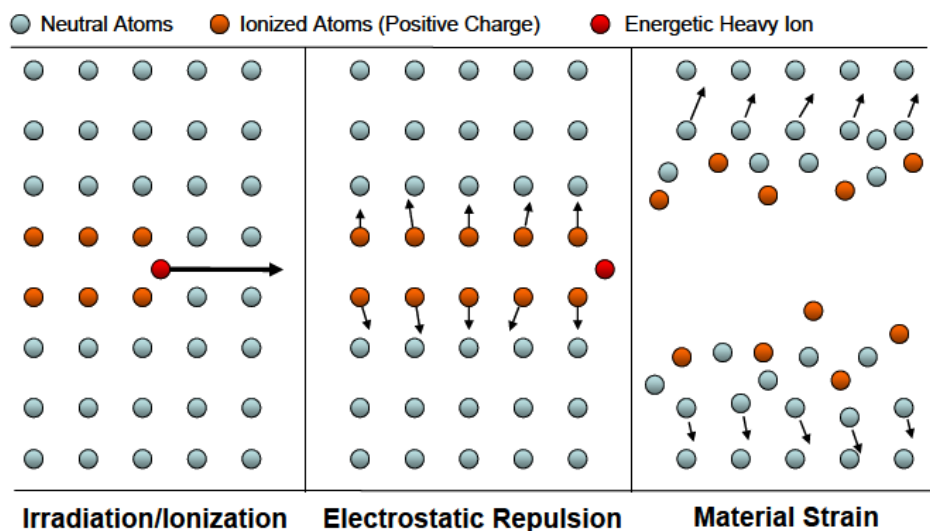


Figure 4.2.2 Ionization spike model. Diagram showing the ionization spike model for latent track formation. The imparted heavy ion fully ionizes atoms which it passes, resulting in an electrostatic repulsion between neighboring atoms along the damaged track. Image courtesy of Eric Kalman.²⁸

v_{bulk} , and along the damaged track, v_{track} , will be influenced by the etchant concentration and temperature. Additionally, the etch rate v_{track} will be significantly faster than v_{bulk} due to the increased reactivity of the broken polymer chains. For reference, using 9 M NaOH at room temperature results in $v_{\text{track}} = 1200 \text{ nm/min}$ and $v_{\text{bulk}} = 2 \text{ nm/min}$.⁹⁰ It has also been shown that exposing the films to UV radiation, prior to etching, speeds up v_{track} through creating more fragmented polymer chains.⁹¹ The difference between the track and bulk etch rates is what enables the formation of a nanopore and can be used to tune the pore characteristics.

Through altering the etch conditions, it is possible to change the ratio of v_{bulk} to v_{track} . This allows for some control over the pore shape by controlling the etching in the radial and axial directions. In the limit that v_{track} is much larger than v_{bulk} , the bulk etch rate can essentially be ignored. This will produce a pore that has completed the axial etch before any radial etching is done resulting in a pore which is cylindrical in shape. Once the pore has etched through, further incubation in the etchant solution will increase the pore diameter evenly at the rate of v_{bulk} along the length, maintaining the cylindrical shape. If instead, v_{bulk} becomes more significant when compared to v_{track} , it results in some radial etching that increases the pore diameter in areas where the track was first etched. If etchant is placed on both sides of the membrane, this will create a symmetrical but hourglass shaped pore, with the center of the pore having the smallest diameter. If the etchant is placed only on one side, the final pore shape will be conical with the smallest diameter on the end farthest away from the etchant. This can be seen in Figure 4.2.3 (left side). Conical pores etched in this way can have small opening angles (1° - 2°)⁹² with incredibly small tip diameters (sub 10 nm) through the application of a few additional techniques.

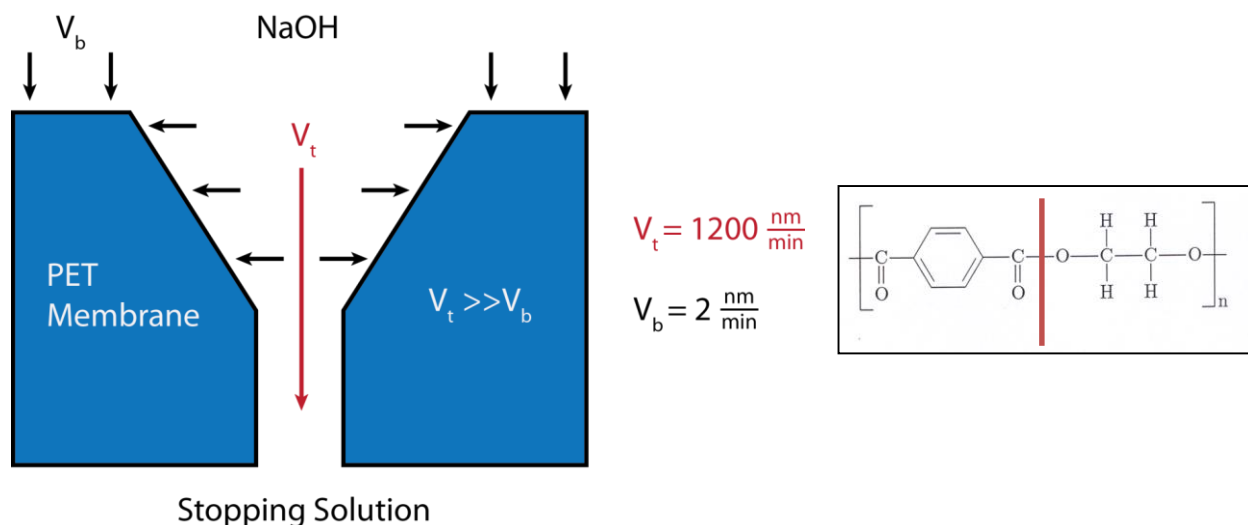


Figure 4.2.3 PET pore etching. (Left) Conditions used to etch a conical pore in a PET film. The etch rate along the track is much faster than the bulk etch rate, resulting in a cone shaped cross section with a small opening angle. (Right) Chemical structure of the PET polymer showing the site which is attacked by the NaOH (red line).

Control over the shape of a conical pore, especially the tip diameter, can be enhanced through the use of additional controls in the etching process. First, a mildly acidic stopping solution can be placed on the side of the film opposite from the etchant. As the track etch breaks through the far side of the membrane, this stopping solution is exposed and neutralizes further etching of the pore. This is particularly useful because tip diameter can grow beyond the sub 10 nm range in a matter of minutes following breakthrough. A second addition is an applied voltage across the membrane through the use of platinum electrodes placed in solution. The benefit of this technique is twofold. When positive voltage is applied on the etchant side, it pulls hydroxide ions away from the tip, slowing down the etch rate prior to breakthrough and allowing more room for error in stopping the etching process. This voltage also provides an easy way to monitor the breakthrough and know when occurs. Measurement of the ionic current across the membrane will show a significant spike the moment an ion channel is formed. When this is observed, the etchant is removed, the membrane is washed, and the etching step is complete. Finally, it has been found that PET

pores can sometimes have incompletely etched polymer strands near the tip of the pore.^{93,94} The length of these dangling ends is small enough that they can be typically ignored, but when the pore size is only a few nm, they can impact the pore behavior. If the pore shows reversible pore blocking or non-smooth I-V curves, it is sometimes desirable to briefly expose the tip side of the film to NaOH. If done quickly enough this can help to remove some of these polymer strands without significantly increasing the tip diameter.

4.2.2 PET Surface Chemistry

PET pores etched using the track etch technique have surface chemistries that are desirable for several reasons. The etching process produces a pore wall that consists of exposed hydroxyl and carboxyl groups.⁹⁵ This gives rise to the first benefit of PET pores, which is hydrophilicity. Due to the polarity of the exposed groups PET pores wet very easily, which is not always the case at the nanoscale. The chemical groups at the surface also result in a net surface charge under most testing conditions (about e/nm^2 at pH 8).⁹⁶ This comes from the deprotonation of the carboxyl groups at sufficiently high pH levels (carboxyl groups have a pK_a around 3.7).⁹⁷ When the pore diameter is small enough, this surface charge can change the pores ionic behavior as discussed in Chapter 2. Finally, these carboxyl groups are attractive because they can be used to attach many different kinds of modifications to the pore surface.

In the case of this project, the modification chemistry used was based on a commonly used technique involving N-(3-Dimethylaminopropyl)-N'-ethylcarbodiimide (EDC).⁹⁸ In this process, which is summarized in Figure 4.2.4, the carboxyl groups are first exposed to EDC, which combine to form an active O-acylisourea ester. This intermediary state is not

particularly stable and is quickly replaced with an amine group, producing an isourea byproduct. The end result is a strong amide bond between the original carboxyl group and added amine groups. It follows then that so long as the desired pore modification either has or can be attached to an amine group, it can be easily adhered to a PET pore wall. Luckily, there are several companies from which amine modified DNA can be ordered to spec, which is what was used here.

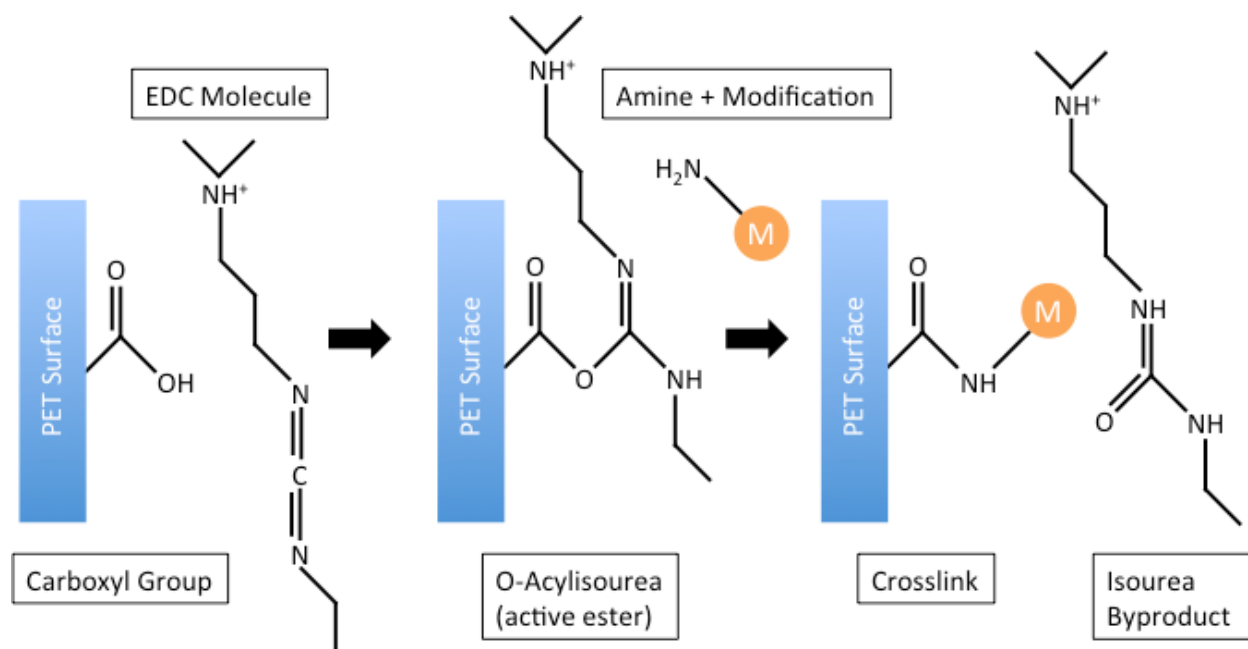


Figure 4.2.4 EDC chemistry. Chemical diagram showing the one step EDC modification reaction. A surface containing a carboxyl group reacts with EDC to produce an intermediary O-acylisourea molecule which is displaced by an amine group. The end result is the attachment of the modification molecule to the surface via an amide bond.

4.2.3 Characterization of Nanopores

The conical PET pores used in this section were characterized using known etch rates combined with measurements of ionic current. The complete picture representing pore transport was discussed in Chapter 2, however, the pores used in this section allow for many useful simplifications to be made. Due to the negligible amount of electroosmotic flow in

these pores, the Stokes equation and corresponding velocity term can be dropped.³³ Additionally, when doing characterization, we will be working at very low voltages and high KCl concentrations, so that the device can be assumed to behave ohmically even when small.⁹⁹ This allows us to model the pore as a simple resistor made from a linear dielectric material. We know that our pores are conical in shape and therefore we must solve for the matching geometry. It turns out that a perfectly conical pore is not analytically solvable so we instead use an approximation with the pore size given by

$$d = \frac{4L}{\kappa\pi DR} \quad (4.2.1)$$

where L is the pore length, D is the large pore opening, R is the pore resistance, d is the small pore opening, and κ is the bulk conductivity. The accuracy of this simplified equation increases with decreasing opening angle, which is why its use is acceptable for the high aspect ratio pores in this chapter.¹⁰⁰ In the above equation, we are able to deduce R through taking I-V curves and measuring the slope at low voltages. Figure 4.2.5 shows the pore geometry as well as an example I-V curve and corresponding value of R.¹⁰¹ We are also able

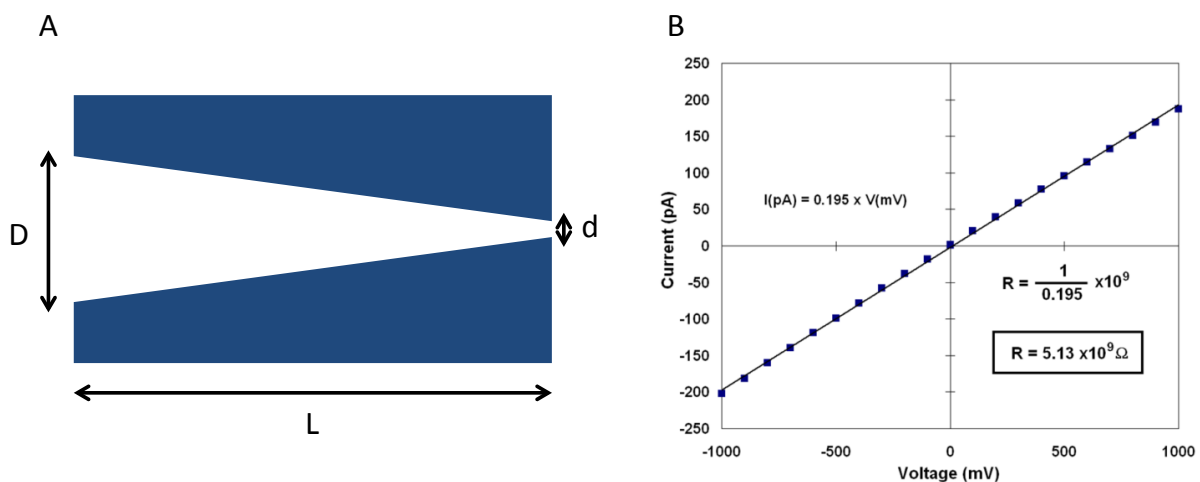


Figure 4.2.5 Pore sizing. (A) Geometrical layout of a conical pore for which Equation 4.2.1 can be used. (B) Sample fit of an I-V curve from a conical pore in order to find the resistance. The resistance shown corresponds to a pore with a 7 nm tip diameter. (B) Courtesy of Matt Powell.¹⁰¹

to find D based on the bulk etch rate of PET in 9 M KOH and the total pore etching time. The length L , is known based on the thickness of our films and the bulk conductivity is easily measured or looked up. This leaves us in a position where we can find the small pore opening, d , which is the physical parameter of most interest in determining pore behavior.

4.2.4 Rectification in Conical Nanopores

Rectification in nanopores refers to the passage of current in one direction much more readily than the opposite direction. This is a type of behavior commonly seen in electronics, being the primary purpose of a solid state diode. This behavior is also observed in biological pores such as α -hemolysin, although their complex structure makes it difficult to analyze.¹⁰² In some synthetic nanopores, however, the structure is simple enough to reveal the underlying physics of rectification. Through solving the PNP equations discussed in Chapter 2, it is possible to see that a conical nanopore with negative surface charge will rectify under the correct conditions (shown in Figure 2.1.2).^{34,103} The carboxyl groups present on pores made from PET carry a negative charge and result in high concentrations of cations, such as potassium, near the pore walls. At the tip of the pore, where the diameter approaches the Debye length, the concentration across the pore profile will be almost entirely potassium ions. As a result, the transport through our pores is strongly cation selective with a ratio of 9:1 cations to anions.^{104,105} When an applied potential is in the direction that moves positive ions from the tip towards the base, the ions readily go. This is helped by the fact that the tip side easily replaces ions from the nearby bulk. In the opposite case, the potassium will be pushed from the tip towards the bulk leaving a space that needs

to be sourced from the base area of the pore. This is more difficult and results in a lower transport rate.

This behavior is dependent on an underlying asymmetry in the system combined with some form of surface charge. In the case of our PET conical pore, the surface charge is constant while the narrowing diameter of the pore breaks the symmetry. In an alternative setup, the surface charge could be modified such that part of the pore has a charge and part does not (unipolar diode) or that part has a negative surface charge and part has a positive

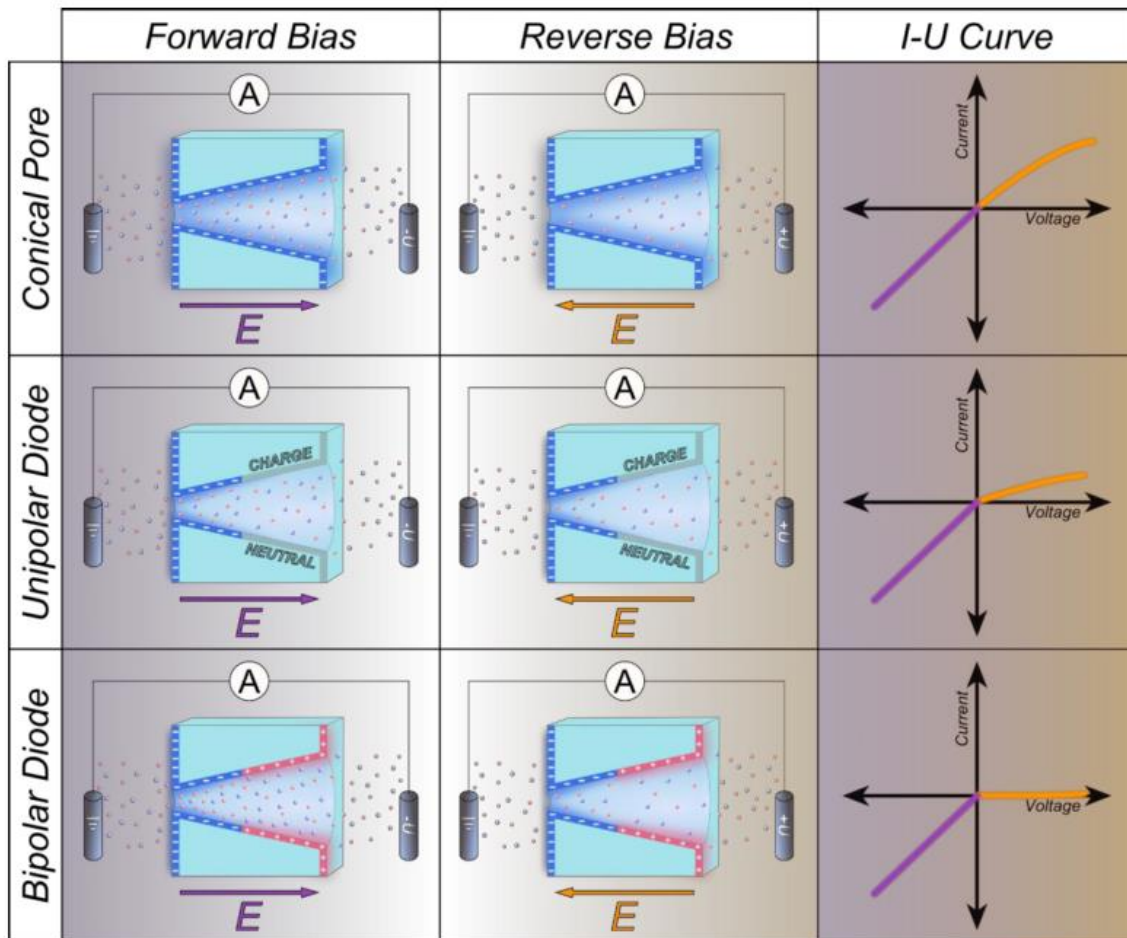


Figure 4.2.6 Ionic diodes. Diagram showing different types of nanofluidic diodes. Asymmetry is derived from both the conical shape and a non-uniform surface charge. In the unipolar and bipolar case, the discontinuity in surface charge forms depletion regions making it harder for ions to pass in the off state. Figure courtesy of Matt Davenport.¹⁰⁹

surface charge (bipolar diode). In the bipolar and unipolar setup, the non-uniform surface charge adds additional asymmetry to the system, increasing rectification. This is realized through the formation of an ion depletion region near the surface charge discontinuity which is enhanced or reduced based on the direction of the applied potential.¹⁰⁶⁻¹⁰⁸ Drawings of these three types of rectifiers are shown in Figure 4.2.6.¹⁰⁹ When using pores made from unmodified PET, the level of rectification can also be modulated through changing the solution pH, which changes the charge on the pore walls. Using a pH near the pK_a value of carboxyl groups can result in the removal of rectification. This behavior is also dependent on the ion concentration which directly influences the Debye length. Lower salt concentrations increase the Debye length which can increase the impact of the surface charge on the ion density in the pore. Finally, rectification is dependent on pore size. Pores with smaller diameters are more influenced by surface charge and diffusion limited processes resulting in higher rectification. If the pore diameter is significantly larger than the Debye length, rectification behavior will not exist based on these principles.

4.2.5 Charge Distribution of DNA

Of particular importance to this work is the location of charges along the DNA molecule. The net charge of DNA is heavily negative with each sugar-phosphate segment containing a one extra electron charge. Due to the double helix structure, dsDNA will have two electron charges per segment, while ssDNA will have only one. The length of a single sugar-phosphate-nucleotide unit is approximately 3 nm which means that DNA is one of the most negatively charged molecules, per unit length, found in nature. This backbone charge dominates the large scale behavior of a DNA strand, but on the smaller scale, the nucleotides

themselves can show some interesting behavior. As previously mentioned, each base is slightly different which results in each molecule having a slightly different pK_a value. A and C are both relatively protonatable with a pK_a value of around 5.3.^{110,111} G on the other hand has a much lower pK_a of 3 and T usually does not become protonated.¹¹² Under the right conditions, this allows for the formation of local positive charges among the strands of DNA which contain the proper bases. These local charges may influence the conformation of DNA¹¹³ and how DNA strands packed in high density can interact with each other which is a concept that we aim to test and use as a gating mechanism.

4.2.6 DNA Conformations in Solution

The steric effects resulting from DNA attached to the inside of a nanopore will influence the pore behavior. Single stranded DNA is much more flexible than its dsDNA counterpart. This flexibility allows the conformation of a ssDNA molecule to be greatly influenced by different types of forces. One such force is due to the exposed bases which have affinities for one another. Complimentary bases will bond to each other, forming so-called hairpins, inducing a conformation which reduces the free energy of the molecule. This effect can be controlled through the careful selection of the nucleotide sequence. Many tools are available which allow for the prediction of ssDNA conformations based on nucleotide binding and the corresponding free energy values. The easiest way to avoid this problem is to use sequences which do not contain any complimentary bases, such as a repeating sequence of A and C, or all one base.

Another important element in determining the conformation of a DNA strand is the repulsion of each sugar-phosphate backbone element on its neighbors. In the absence of

other molecules, this repulsion will cause the DNA strand to stiffen. When the DNA is in solution, the highly charged backbone will attract ions of the opposite sign, thereby shielding some of this repulsion. The more ions that are available in the solution, the larger this shielding effect will be and the repulsion due to the backbone charge will decrease.¹¹⁴ The result of this phenomenon is that a high ionic concentration causes a ssDNA strand to fold in on itself more readily, decreasing its effective length, while at low salt concentrations the opposite occurs. This behavior has been predicted by modeling polyelectrolyte chains, which was done as early as 1977.¹¹⁵ Additionally, the persistence length, a measure of stiffness, seen in ssDNA has been experimentally measured as a function of ion concentration and can be seen to decrease as salt concentration increases.¹¹⁶ A lower persistence length corresponds to a more flexible ssDNA molecule, which can be seen in Figure 4.2.7. This is especially important in nanopores since it means that changing the concentration of salt in a solution can directly translate to changing the effective pore size.

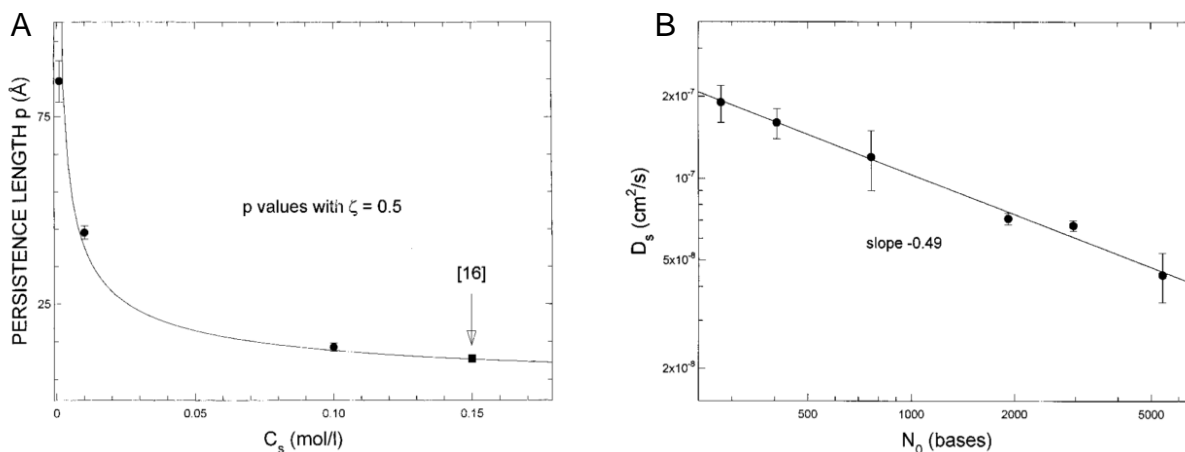


Figure 4.2.7 ssDNA length. Characteristics of ssDNA molecules experimentally measured using fluorescence recovery after thermal denaturation. (A) Plot of the persistence length of ssDNA as a function of the ionic concentration. (B) Plot of the diffusion coefficient as a function of number of bases of a ssDNA molecule. Reprinted with permission from Tinland et al.¹¹⁶ Copyright 1997, American Chemical Society.

4.2.7 Concentration Profile in a Conical Nanopore

The work in this chapter will take advantage of the ability to only modify one side of a conical nanopore. In the majority of cases, DNA is attached to only a small segment at the tip and in one case DNA is attached everywhere except the tip. The way in which this is accomplished is through the steady state solution to diffusion stemming from a single side of the pore. What this means is that if the ssDNA solution is placed only on the tip side of the pore, the concentration of ssDNA very quickly dies off along the direction of the pore axis resulting in sufficiently high concentrations to induce modification only at the tip.

In order to better see this a calculation can be done to predict that concentration gradient in our conical pores. This can be expressed starting with the steady state diffusion equation which reduces to Laplace equation

$$\nabla^2 C = 0 \quad (4.2.2)$$

where C is the concentration. It is then easiest to define a conical pore using spherical coordinates with an opening angle and length in terms of r and use the Laplace equation in spherical coordinates. Switching variables back to x , applying the appropriate boundary conditions for either the tip or base side and then solving for the concentration is possible. The complete derivation will not be done here but can be seen in the thesis of Gael Nguyen.^{106,117} The solution to starting with DNA on the tip side is found to be

$$C(z) = C_0 \frac{a \cot(\alpha)}{L} \left(\frac{L - z}{a \cot(\alpha) + z} \right) \quad (4.2.3)$$

and the solution resulting from DNA placed on the base side is

$$C(z) = C_0 \frac{z}{L} \left(\frac{L + a \cot(\alpha)}{z + a \cot(\alpha)} \right) \quad (4.2.4)$$

where the coordinates are given by Figure 4.2.8 part C. The previous two equations are plotted in Figure 4.2.8 part A and B which show strong gradients of modifying agents over the first few hundred nm or the pore tip which die off at larger distances.

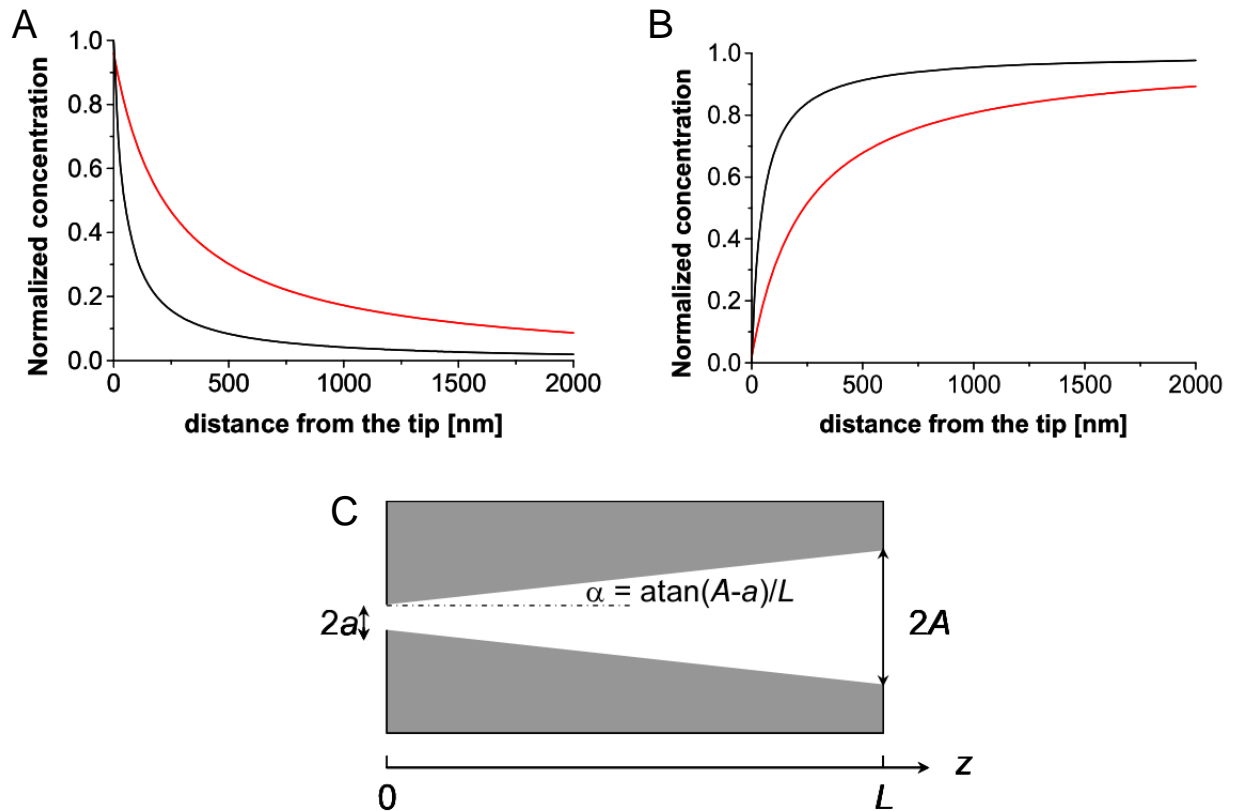


Figure 4.2.8 Diffusion through a conical pore. Plots of the steady state solution for diffusion from the (A) tip side and the (B) base side of a conical nanopore. The narrow opening of the pore was set to 5 nm and the large opening was set to 250 nm (red line) and 1250 nm (black line). (C) Schematic of the pore used in the diffusion model resulting in Equation 4.2.3 and 4.2.4. Figures courtesy of Nguyen et al.¹⁰⁶ © IOP Publishing. Reproduced with permission. All rights reserved.

4.3 Experimental Setup

4.3.1 PET Pore Fabrication

Individual cone shaped nanopores were prepared in 12 μm thick PET membranes using the track etching technique discussed in section 4.2. Films were first irradiated by our collaborators at GSI Helmholtzzentrum für Schwerionenforschung GmbH (GSI).¹¹⁸ This was

done with stacks of eight samples that were covered in a mask, restricting ion penetration to a 0.1 mm diameter region in the center. Au atoms were accelerated towards the membranes at an energy of 11.4 MeV and detected on the other side, ensuring that only a single ion penetrated each film. Following delivery to our lab, the samples were placed under UV radiation (max intensity at 320 nm) for 30 minutes. The membranes were then loaded into

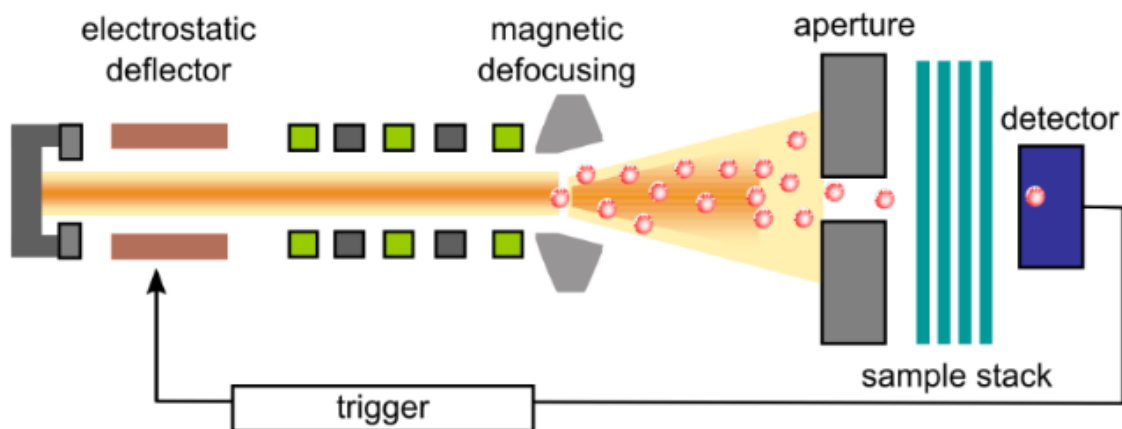


Figure 4.3.1 GSI beamline. Schematic of the GSI beamline used for single ion irradiation of a PET film. Following acceleration, the beamline is defocused so approximately 1 ion per second are sent to the film. An ion detector is used to ensure that only a single ion hits each film. Image courtesy of Toimil-Molares et al.¹¹⁸

a polychlorotrifluoroethylene and stainless steel cell and sealed with parafilm and pressure for etching. During etching, 9 M NaOH was loaded into one side of the cell and 1 M formic acid stopping solution was loaded into the other at room temperature. Platinum electrodes were inserted into both sides of the cell and 1 V was applied across the membrane, with the positive electrode on the NaOH side. Trans-membrane current was monitored until a spike was observed at which point the NaOH was removed, etching time was recorded and stopping solution was added to both sides, followed by washing of the membrane with DI and/or KCl solution. If pores showed erratic conductance behavior, the tip side was sometimes exposed to 9 M NaOH for an additional 30 s.

4.3.2 Conical PET Pore Characterization

Immediately following etching and washing of a membrane, both reservoirs were filled with KCl solution of known concentration and pH. Voltage sweeps were then applied between -5 V and +5 V and current values were recorded at intermediary values to generate I-V curves. During this step and the remainder of pore measurements Ag/AgCl electrodes were used to measure ionic current. Conductance information from the I-V curves along with etching time were then used to find the size and shape of the pores based on the equations given in the previous section. Several I-V curves were taken at different KCl concentrations to ensure each pore showed expected and repeatable behavior before proceeding with any sort of modification.

4.3.3 Modifying Pores with ssDNA

DNA oligomers chemically modified with an amine attached to the 5' end were ordered from Integrated DNA Technologies (Coralville, IA) with three different sequences:

- 5- /5AmMC12/CGC GAG AAGTTA CAT GAC CTG TAG ACG ATC -3
- 5- /5AmMC12/CAC CCA CAA CCA CCA ACA CAC ACC ACC ACC -3
- 5- /5AmMC12/GTG GTG GTG TGG TGG TGT TGG TGG TGG TGG -3

Prior to modification, DNA was resuspended into 100 mM MES buffer at pH 5.5 to achieve a DNA concentration of 1.2 ± 0.3 mM. 0.05 M EDC was then added to the DNA solution to facilitate bonding between the 5' amine modified DNA end and the carboxyl groups along the pore surface. This solution was then added to one side of a mounted nanopore (generally the tip side) and incubated for 24 hours at room temperature. Following removal of the DNA solution and washing of the film with DI, modified pores were then re-characterized at 1 M

KCl to ensure modification was successful. This was most easily seen through a reduction of the effective pore diameter.

4.3.4 Data Acquisition and Analysis

The majority of data shown was recorded using a Keithley 6487 picoammeter/voltage source. If higher resolution time data was required, data was taken on an Axopatch 200B Amplifier (Molecular Devices). Data analysis was done using Wolfram Mathematica, OriginLab Origin, Adobe Illustrator and Microsoft Excel.

4.4 Results and Discussion

4.4.1 Competing Steric and Electrostatic Effects from DNA Modification

Following successful modification of our PET pores with ssDNA at the tip, I-V curves were recorded at both pH 8 and pH 5.5. As expected, the addition of this DNA had a

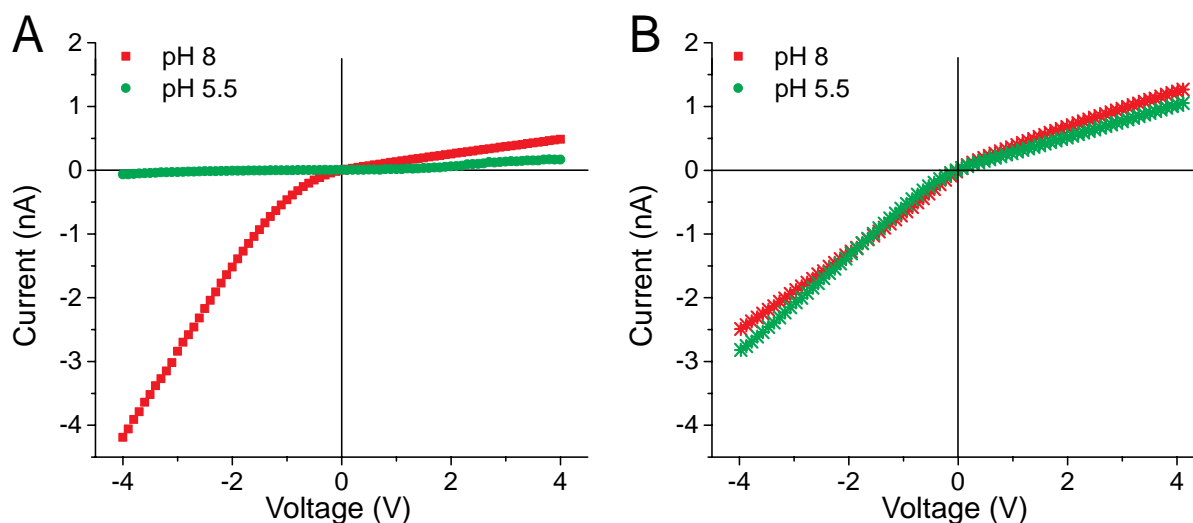


Figure 4.4.1 AC-rich modified pore. (A) I-V graphs for nanopore modified with AC-rich DNA recorded in 100 mM KCl at pH 8 (red) and pH 5.5 (green). The small opening diameter of this pore was found to be 8 nm after modification. (B) I-V curves for the same pore prior to DNA modification. All data is an average of three scans.

significant impact on the overall pore conductance. Figure 4.4.1 shows the I-V curves from a conical pore before and after modification with AC rich DNA, at both pH 8 and 5.5. It can be seen that this pore exhibits a strong pH and voltage dependent behavior following modification. In order to understand these effects, it is first useful to study pH independent impacts of the DNA modification. Focusing first on the pH 8 scans, it can be seen that the ionic conductance actually increased following the modification. This may be somewhat surprising considering that a significant amount of material is added to the interior of the pore, thereby reducing the effective pore diameter. In order to understand what is happening here, it is important to note that there are actually two competing phenomena which alter the pore conductance.

The first effect, which was already briefly mentioned, comes from the filling of the pore with DNA. This results in a steric effect which reduces the void space or open volume of the pore. As discussed earlier in this chapter, the conductance of a nanopore is directly related to its effective cross section. This means that the more DNA there is inside the pore, the lower the conductance will be. On the other hand, DNA is known for being a highly charged molecule and it brings this charge with it into the pore. From Chapter 2, it was shown that, assuming the pore has a diameter on the order of the Debye length, surface charge will alter pore conductance through influencing the salt concentration inside the pore. The highly charged DNA can then be thought of as increasing surface charge, while simultaneously reducing the pore diameter. These steric and electrostatic effects can alter the conductance in opposing ways with the relative strength of each dependent on the specific conditions of the pore.¹¹⁹ One way this can be tested is through modifying pores of different sizes with the same DNA molecules and this is shown in Figure 4.4.2. It can be seen

that the behavior is roughly broken up into three regions. In the case of a very small pore (less than ~ 5 nm) the occluded volume resulting from the DNA dominates all other effects and the current is dramatically reduced. In the very large pore case (above ~ 20 nm) it can be seen that neither effect is particularly significant, with the occlusion barely winning out. Finally, there appears to be a middle region where the electrostatic effects overcome the DNA occlusion to increase the pore rectification resulting in higher currents at low voltages following modification.

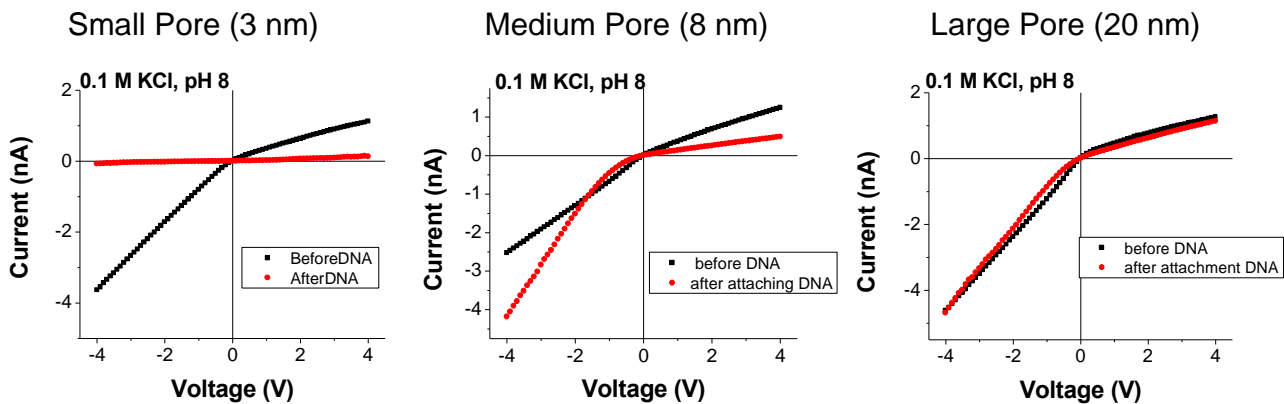


Figure 4.4.2 DNA in different size pores. I-V curves before and after DNA modification for pores with diameters of 3, 8 and 20 nm on the tip side. In the small pore the DNA occludes the pore volume overwhelming the electrostatic effects and dramatically reducing the current. In the medium diameter case, the electrostatic effects are able to overcome blockage from the DNA increasing the current and rectification. In the large pore case, neither the surface charge or occluded volume have a significant effect but the current can be seen to slightly drop.

To further complicate matters, a change in electrolyte concentration will have an impact on both of these effects. As salt concentration drops, the Debye length increases and therefore the impact of surface charge also increases. This means that at very low salt concentrations, the current amplification caused by the DNA charge will have a larger effect. Additionally, the extension of a DNA molecule is dependent on the ionic shielding from the surrounding electrolyte (Figure 4.2.7). As KCl concentration is decreased, the DNA will

experience larger electrostatic repulsion and extend farther into the pore interior, lowering the conductance.

4.4.2 Nano-mechanical Voltage Dependent Gating

Voltage dependent gating has previously been reported in pores with DNA modifications and the pores in this work show it as well.¹²⁰ In Figure 4.4.1 it can be seen (most easily at pH 8) that after DNA modification of an 8 nm pore, the rectification increased due to the DNA in the pore. This DNA induced voltage response is not seen in pores of all sizes however and an explanation is shown in Figure 4.4.3. As a voltage sweep is applied across a conical nanopore, the DNA is first pulled in one direction (towards the tip side of the pore for negative bias) and then pulled in the other direction (towards the base side for positive bias). Due to the asymmetrical shape of our pores, this can potentially result in a

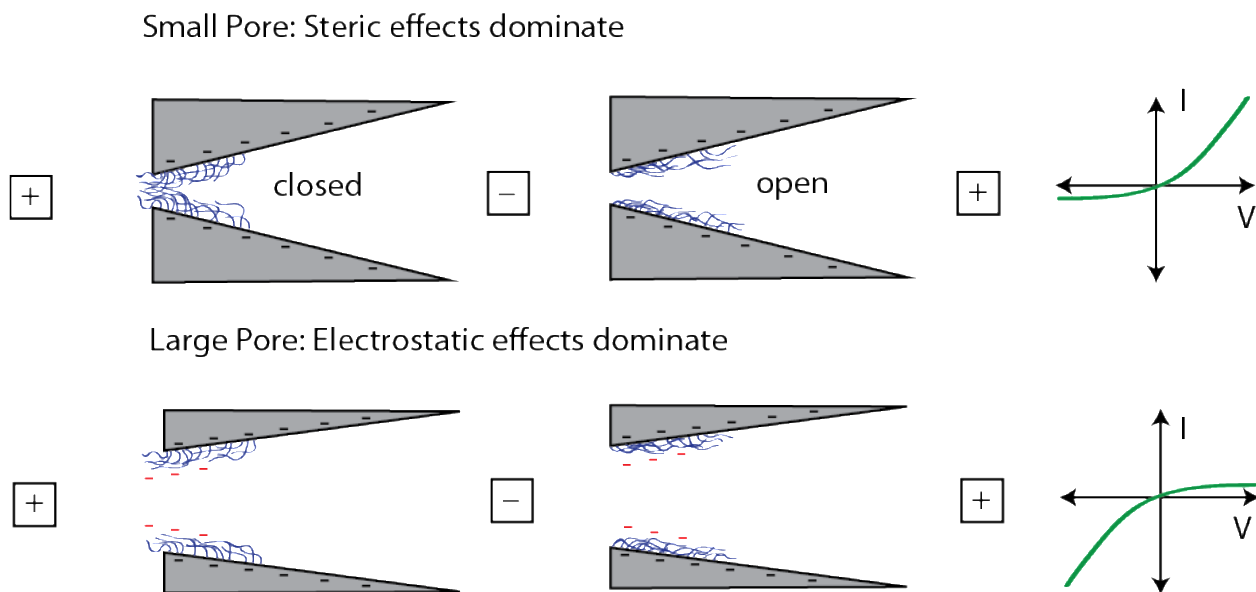


Figure 4.4.3 Voltage response vs pore size. Drawing which shows the voltage dependent gating resulting from the attachment of ssDNA to the pore interior. It can be seen that the voltage induced conformation change of the DNA influences pore behavior in a diameter dependent way.

type of gating behavior if the pore has a small enough diameter. For large pores, the arguments of the previous section apply and extension of the DNA due to the applied voltage does not have a large impact on overall conductance. In this case, the pore will continue to rectify in a similar fashion as an unmodified pore, but more strongly due to the increased surface charge. In smaller pores however, this voltage dependent steric blockage can start to dominate the behavior. As DNA is pulled towards the tip, it is packed into a smaller volume, thereby reducing pore conductance. When the DNA is pulled towards the base, the opposite happens. This induces rectification in the opposite direction of our unmodified pores. If the DNA gating effect is strong enough, it is possible for this to dominate the pore behavior and reverse the rectification which will be discussed in section 4.4.4.

Under certain testing conditions, I-V curves also show evidence of more complicated DNA movement occurring inside the pore. One place this can be seen is in the I-V curves for an 8 nm DNA modified pore which is shown in Figure 4.4.4. It seems that a voltage sweep from negative potential to positive does not always produce the same I-V curve as one applied in the opposite direction. It has been suggested that this effect, known as hysteresis, is dependent on the initial state of the DNA prior to taking a conductance measurement.¹²⁰ If the DNA is packed tightly (into the pore tip for example), then it could potentially become “stuck”, requiring additional force to revert to a new state. If the DNA is instead deflected into a larger volume (such as the base of the pore), it will be much easier for it to change orientations. This means that, at some intermediary voltage, scanning from the positive to negative direction could result in a different conductance value than what is seen when the scan is done in the opposite direction, similar to what is observed in the I-V curve in Figure 4.4.4.

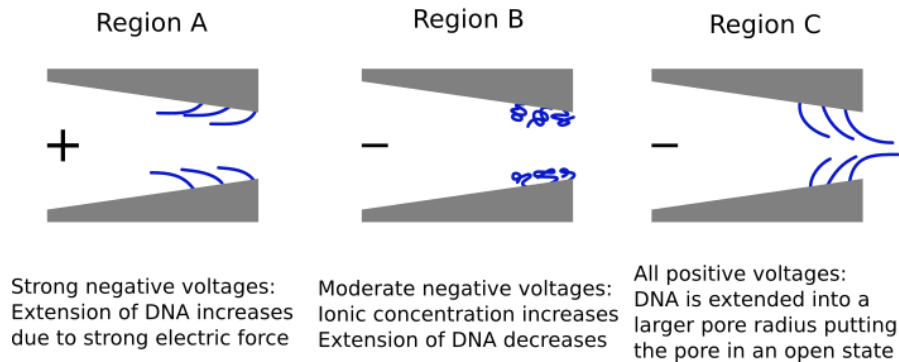
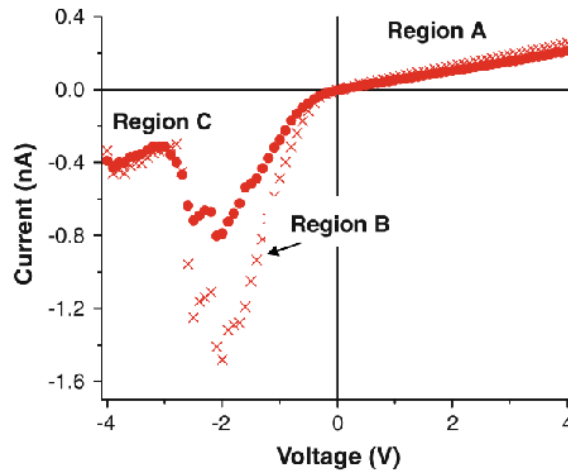


Figure 4.4.4 Hysteresis from DNA conformations. Forward (+4 V to -4 V) and reverse (-4 V to +4 V) I-V curves are shown for a pore with 8 nm diameter showing hysteresis. Insets show diagrams of DNA configurations at key points through the voltage scan. Image adapted from Nguyen et al.¹²⁰ with permission of Springer.

This explanation for the hysteresis is further solidified by what appears to be a transition in conductance states within the negative voltage regime during a single voltage sweep. We hypothesize that this is caused by the fact that low/medium negative applied voltages induce an increase in ionic concentration inside the pore that increases the amount of ionic shielding around the DNA. This in turn can reduce the effective length of the molecules, opening up the pore and putting it into a temporary open state. As the negative bias is increased, the electric force acting on the DNA eventually overcomes this effect and pulls the DNA towards the tip, reducing the pore conductance. The I-V curve in Figure 4.4.4

shows this transition, from region B to region C, occurring at around negative 2 V and a schematic drawing showing the DNA structure in each region is given. This intermediate state is relatively fragile and can form more easily when the DNA starts in a less packed orientation. It will be seen in a later section that this intermediate conformation can be removed entirely through changing the solution conditions.

4.4.3 pH Dependent Gating through DNA Mesh Formation

One of the primary goals of this research was to create a gate sensitive to multiple stimuli, in this case voltage and pH. To achieve this, the DNA, which was previously described to show voltage dependent gating, was carefully selected to show pH sensitivity as well. Custom DNA molecules were tailored based on the fact that each nucleotide has a different

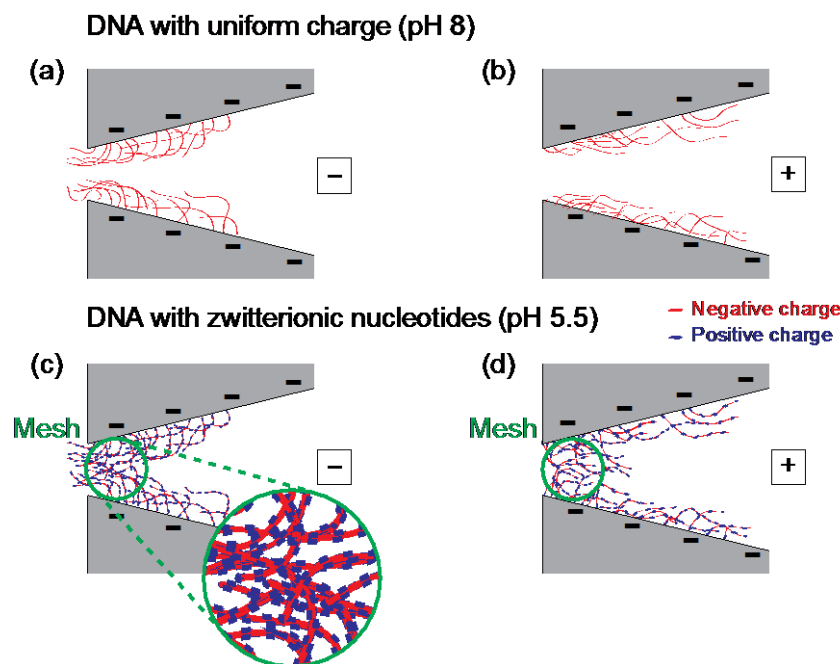


Figure 4.4.5 Formation of electrostatic mesh. Schematic of voltage and pH responsive gating in conical pores modified with DNA molecules. (a) Voltage induced deflection of negatively charged DNA reduces ionic current. (b) Deflection in the opposite direction results in increased conductance. (c) Careful selection of nucleotide sequence results in the formation of a nanomechanical mesh blocking the pore. (d) Deflection of the DNA is only partially allowed due to mesh formation.

pK_a value. The relatively protonatable bases, A and C, were used to create our gated nanochannels, and the much more difficult to protonate G and T were used as control sequences. Returning to Figure 4.4.1 it can be seen that prior to modification, the nanopore showed very little difference between scans done in pH 8 and pH 5.5. This is expected since the pK_a of the negatively charged carboxyl groups of the PET walls is well below 5.5. Following modification however, decreasing the pH to 5.5 had a dramatic effect, lowering pore conductance by approximately 60 times at -4 V (to value below 100 pA). This demonstrates a clear and almost complete closure of the pore for both voltage polarities in response to a pH change.

As an explanation for this pH gating behavior (summarized in Figure 4.4.5), we turn to the nucleotide dependent structure of DNA and how it influences neighboring interactions. At pH 5.5 it is likely that some of the A and C bases have become protonated, giving them a small local positive charge. We believe that when the density of the DNA is

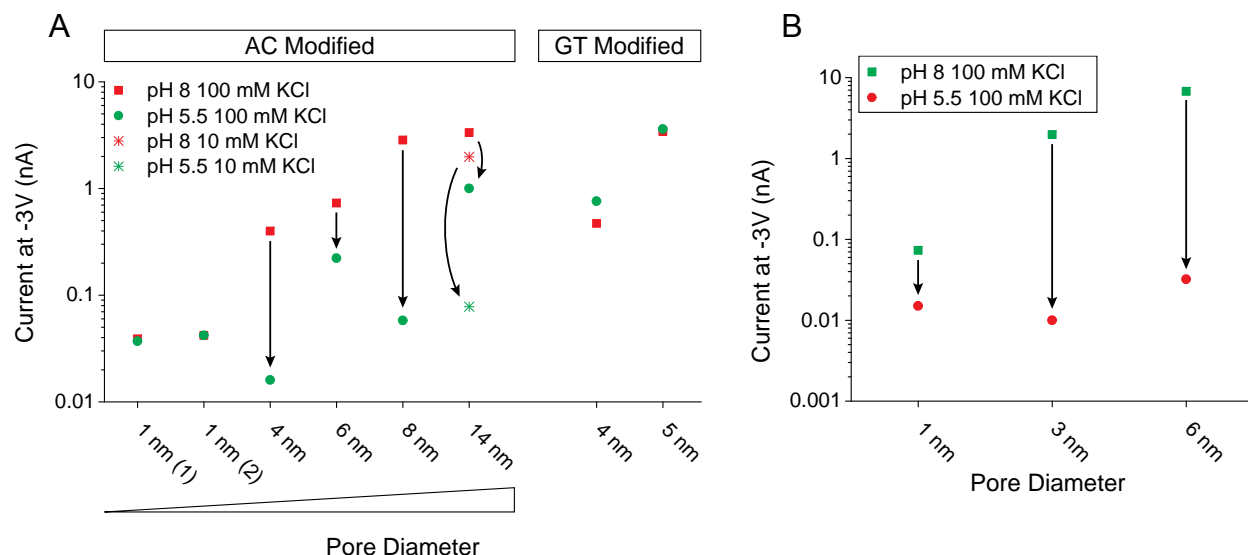


Figure 4.4.6 Summary of pH gating data. Ionic current recorded at -3 V for independently prepared nanopores after attachment of (A) AC-rich and GT-rich ssDNA or (B) DNA containing all bases. Points in red and green represent data at pH 8 and pH 5.5, respectively. The tip diameter given for all pores was calculated after DNA modification in 1 M KCl and pH 8.

high enough, these local positive charges facilitate the formation of a biopolymer mesh that spans the pore. This mesh provides a more complete blockage than previous DNA modifications, producing the large drop in conductance. In order to test our mesh based hypothesis, we repeated the same experiments shown in Figure 4.4.1 using pores with varying diameter modified with both AC rich DNA and our GT control sequence. A summary of the results taken from eight pores with post modified diameters ranging from 1 – 14 nm is shown in Figure 4.4.6 part A and selected pH I-V curves from which this data was taken are shown in Figure 4.4.7.

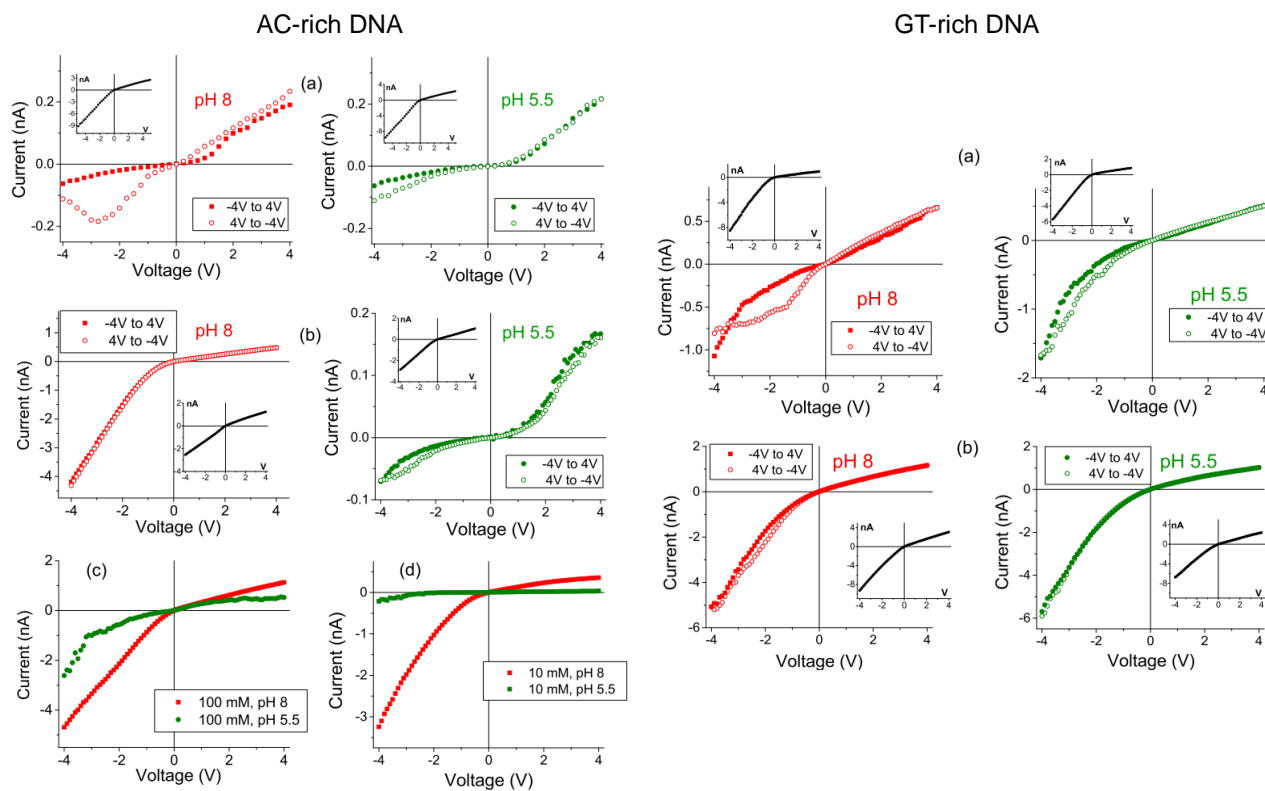


Figure 4.4.7 pH dependent I-V curves. I-V curves for representative pores modified with either AC or GT rich DNA. Data in red and green represent pH 8 and 5.5 respectively. AC-rich DNA: Recordings for three nanopores with opening diameters (a) 1 nm (b) 8 nm and (c,d) 14 nm. Recordings are in 100 mM KCl for (a), (b) and (c) and in 10 mM KCl for (d). GT-rich DNA: Data recorded in 100 mM KCl for a pore with diameter (a) 4 nm and (b) 5 nm. All insets show I-V curves prior to modification.

First, we will focus on the six pores modified with the AC rich DNA strands. These pores show that there seems to be a relationship between post-modified pore diameter and the magnitude of pH response. This can be explained simply by the fact that if the pore is sufficiently filled DNA, there is no room for additional closure. This is observed to be most extreme in the smallest two pores, both with modified diameter of only 1 nm. These two devices show current levels for pH 8 and pH 5.5 that are both similar to those seen in larger pores that are in a closed state. The pores with a modified diameter in the range of 4 to 6 nm showed a moderate pH response and the larger pores showed the greatest response, backing this claim. It is interesting to note that pH behavior was at its maximum for the modified 8 nm pore suggesting that there may be an optimal post modification diameter. This would mostly likely arise from balancing the overcrowding effects of a small pore with high DNA density with the inability of the DNA to bridge the gap of a pore with a larger radius. This idea can be probed through extending the DNA molecules via using a lower KCl

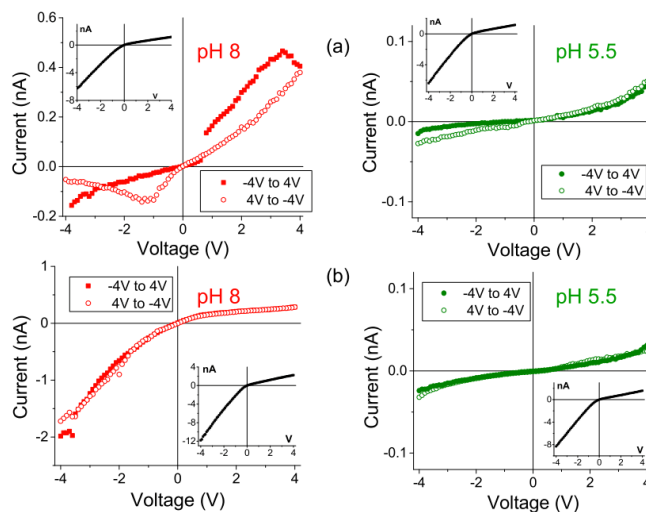


Figure 4.4.8 All base I-V curves. I-V curves for nanopores modified with DNA containing all bases. Scans were taken in 100 mM KCl at pH 8 (red) and pH 5.5 (green). The diameter of the tip side after DNA attachment was (a) 1 nm and (b) 3 nm. Insets show I-V curves recorded at the same conditions prior to DNA modification.

concentration. When the 14 nm pore was exposed 10 mM KCl it did indeed become entirely closed at pH 5.5.

Further evidence of the mesh formation is given by the right most two pores in Figure 4.4.6. As expected, these GT control modified devices did not show any closure in response to lowered pH. The small changes observed were most likely electrostatic in nature and due to the modulation of the surface charge via pH change. From Chapter 2 as well as in previous publications from our lab, it has been shown that such modulation can produce nontrivial, nonmonotonic effects on pore conductance which are also dependent on pore geometry.¹²¹ It is also possible that increased proton concentration resulted in more flexible DNA which increased pore conductance. This behavior makes it very clear that there is no formation of a mesh like in the AC modified case. As additional evidence, we show in Figure 4.4.6 part B that DNA containing all bases also showed pH dependent closure, although it was not as strong. Selected I-V curves from Figure 4.4.6 part B are shown in Figure 4.4.8. This points to the fact that the underlying mechanism for the pH gating comes from the protonation of A

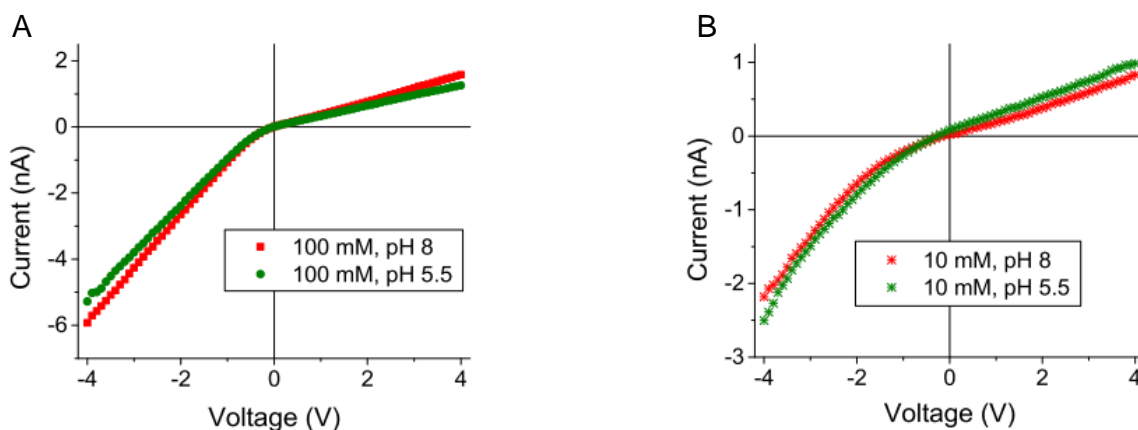


Figure 4.4.9 Base side modificaton. I-V curves from a 14 nm diameter pore which was modified with DNA from the base side in pH 8 (red) and pH 5.5 (green) using (A) 100 mM and (B) 10 mM KCl. Based on the diffusion model presented earlier, it is expected that DNA is attached everywhere except a few hundred nm near the tip. As a result the narrowest region is tens of nm in diameter which is large enough to stop the DNA from forming a pH dependent mesh.

and C along with the inability of G and T bases to be protonated at pH 5.5. As a final check, one pore was modified with DNA placed on the large side resulting in DNA attachment everywhere except a few hundred nanometers near the tip. The data can be seen in Figure 4.4.9 and shows that pH induced gating was not observed. This is most likely due to the fact that the DNA molecules are unable to reach across the larger pore radius and form a stabilizing mesh.

4.4.4 Switching of the Rectification Direction

In order to validate some of the theories thus far, it is useful to closely examine the I-V curves taken from the smallest pores. Figure 4.4.10 shows this data for one of the post modification 1 nm diameter devices. This pore was sufficiently occluded with DNA and showed very little pH response in Figure 4.4.6. More careful analysis shows that the current traces from pH 5.5 and pH 8 do show elucidating differences. At pH 8, hysteresis behavior and a change in conductance states similar to that discussed in section 4.4.3 can be seen,

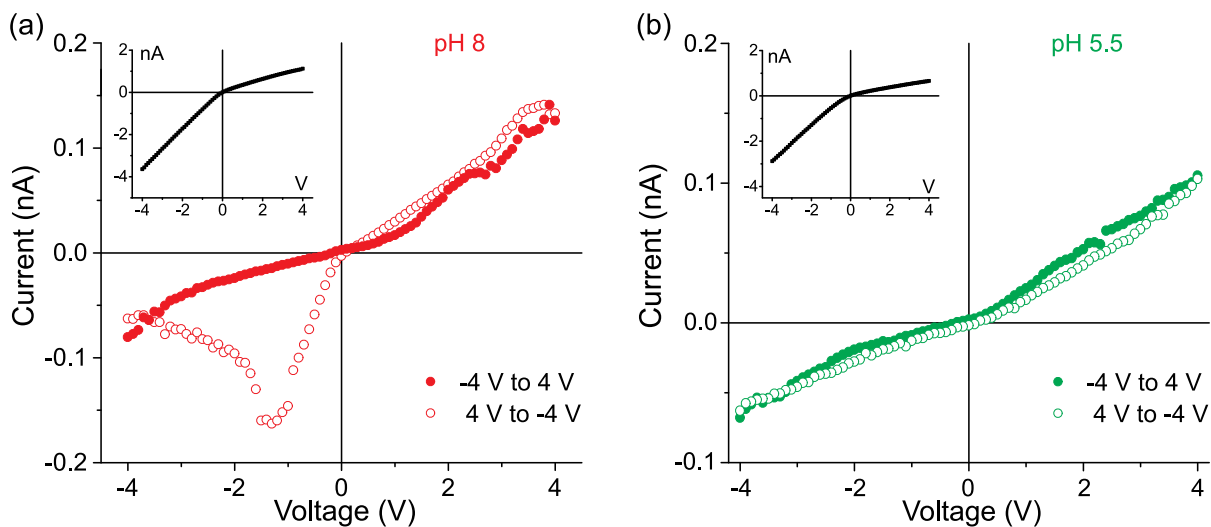


Figure 4.4.10 Switching rectification direction. I-V curves recorded from a pore with a post modification tip diameter of 1 nm at (a) pH 8 and (b) pH 5.5. I-V curves prior to modification (diameter of 3 nm) are shown at the same conditions in the insets.

suggesting that the DNA is free to undergo some asymmetrical movement in response to the applied voltage. Scans at pH 5.5 however, show that this behavior is no longer occurring. This lack of hysteresis in low pH I-V curves suggests that there is a mesh in place that is robust enough to hold the DNA molecules in place and only allow minor deflection.

Beyond restricting movement of the flexible DNA molecules, this mesh formation is strong enough to make the pore undergo a complete reversal in rectification behavior. Figure 4.4.10 part b shows I-V curves with larger currents at positive voltages which is the opposite of behavior seen in unmodified conical PET pores. This type of reversal in pore rectification has previously been achieved by modifying the pore walls with positive charges, but this is the first time it has been accomplished through the addition of negative charges and governed by steric interactions. It may also be worth noting that electroosmotic effects were not considered here and may play a role. It has been previously shown, however, that these effects are very small.¹²²

4.4.5 Reversibility of closure

The pH induced closure of our DNA modified pores is shown to be easily reversible. Figure 4.4.11 presents the data from an AC modified pore (4 nm post modification) that underwent several cycles of closure and reopening. This was done by alternating the pH of the KCl solution between pH 5.5 and 8 with DI washing steps in between. It can be clearly seen that, with the exception of a small current reduction at pH 8, the open and closed states of the pore can be recovered. If the mesh formation is indeed occurring, this would be expected since the A and C bases can be reversibly protonated and deprotonated via pH. To explain the change in current at pH 8 after varying cycles we have two theories. The first is

that each time the mesh forms and deforms, the DNA will be left in a unique arrangement. Differing arrangements could then result in different ionic currents. The second explanation is that there could be some residual mesh formation that never completely recovers. This is

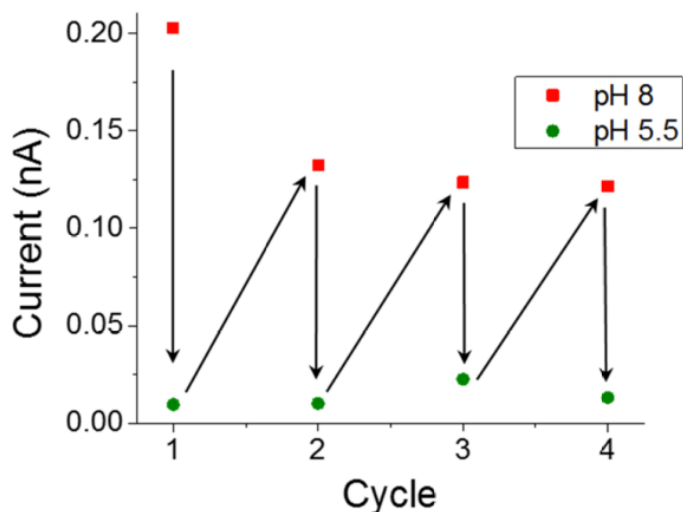


Figure 4.4.11 Reversible closure. Magnitude of the current at -3 V in 100 mM KCl is shown for a pore with AC-rich modified pore with a modified tip diameter of 4 nm. The pH is alternated between 8 (red) and 5.5 (green) and I-V curves were taken from -4 V to 4 V in order to show the reversibility of the mesh formation. The current drop after the first cycle may be due to residual mesh formation.

suggested by the seemingly smooth decay of the current at pH 8 as the DNA structure converges on a possible residual formation. In either case, this current decrease is small enough that it does not hinder overall device reversibility.

4.5 Conclusion

In conclusion, we have presented a novel synthetic nanopore which demonstrates a gating response to multiple stimuli at once, namely changes in voltage and pH. Additionally, when the pore is in the closed state, translocation of both charged and neutral molecules are blocked. This was achieved through the attachment of carefully selected ssDNA molecules

to the tip side of a conical PET nanopore. The central concept of our nanopore gate is the formation of a robust and stable mesh resulting from ssDNA molecules with local positive charges due to the presence of zwitterionic nucleotides. Pore closure and opening was reversibly shown through altering the pH between 8 and 5.5 followed by taking voltage sweeps across the pore membrane. We were also able to gain some insight into the nanomechanical movement of ssDNA inside the confined space of a nanopore as voltage, pH and ion concentration are modulated. We believe our nanopore gate is an important stepping-stone along the road to fabricating synthetic nanopore gates comparable to those found in nature.

While the work presented here, along with other accomplishments in the nanopore community is significant, it is important to note several key shortfalls in synthetic nanopore performance. The first of which is the amplitude of the gating. With the addition of our work, synthetic pores have achieved approximately 100-fold difference in conductance between open and closed states. This is comparable to some biological pores but still at least an order of magnitude below others.¹²³ Additionally, the open states of synthetic pores generally have significantly lower conductance values than those of biological pores. The second area synthetic pores are outclassed is in selectivity. Protein based pores such as potassium and sodium gated channels are incredibly successful in distinguishing one type of ion from another. Even though potassium and sodium have a size difference of less than one angstrom they are easily selected for in their respective ion channels. This requires methods of selection more sophisticated than those that have been designed so far. Finally, natural pores, like the potassium channels described above can respond a complex arrangement of

stimuli at once. While the work here was an attempt to bridge this gap, there is still much ground to cover.

As the capabilities and sophistication of synthetic nanopore gates improve, they will provide new insights, which could help elucidate the remaining mysteries of their natural counterparts. This, in turn, will produce new understandings of nanopore physics that can be applied to improving our synthetic versions. The results of this feedback loop promise to produce future technologies such as novel drug delivery systems designed to release their payload in a safe way under specific conditions or new and exciting biosensors built around recently discovered gating mechanisms.

Chapter 5: Unraveling Nanofluidic Phenomena in Individual CNTs

5.1 Introduction

The focus of this chapter will be on yet another type of nanochannel which is fabricated using carbon nanotubes (CNTs). The history of CNTs goes back a long ways starting in 1952 when Russian scientists L.V. Radushkevich and V. M. Lukyanovich published work showing tubes made of carbon with diameters of 50 nm.^{124,125} Unfortunately, due to the publication being in Russian and exposed to a limited audience thanks to the Cold War, the work was mostly ignored. There were a few intermediate publications, such as the vapor-phase tubes grown by Morinobu Endo,¹²⁶ but the catalyst for future CNT related research didn't come for another 39 years. In 1991, Sumio Iijima published a paper showing CNTs with diameters as small as 0.7 nm and lengths of microns, which were fabricated using arc-evaporation techniques.¹²⁷ Once in the spotlight, many remarkable predictions were made about their properties, which fueled further attempts to find applications for them. Examples include water filtration,¹²⁸⁻¹³⁰ high strength materials,¹³¹⁻¹³³ electronic circuitry and components¹³⁴⁻¹³⁶, and even biomedical applications.¹³⁷⁻¹³⁹ The work done in this chapter will be specifically looking at their use as nanochannels and examining their unique behaviors.

Carbon nanotubes can be thought of as a sheet of graphene (a single layer of carbon atoms in a hexagonal lattice) that has been rolled up into a seamless cylindrical tube. They can be grown with diameters ranging from greater than 100 to less than 1 nm and can have lengths reaching centimeters controlled with sub micrometer precision.¹⁴⁰ Unlike most other pores, which have some form of undulating diameter or surface roughness, CNTs are

uniform along their entire length. Due to their graphitic nature the walls are both molecularly smooth and hydrophobic. An additional advantage is that carboxyl groups at the entrance of CNTs provide an easily targetable site for modifications that may be required in future technologies. Finally, CNTs are incredibly robust and their structure is known with atomic precision which makes them ideal for studies in nanofluidic phenomena and as biomimetic pores.

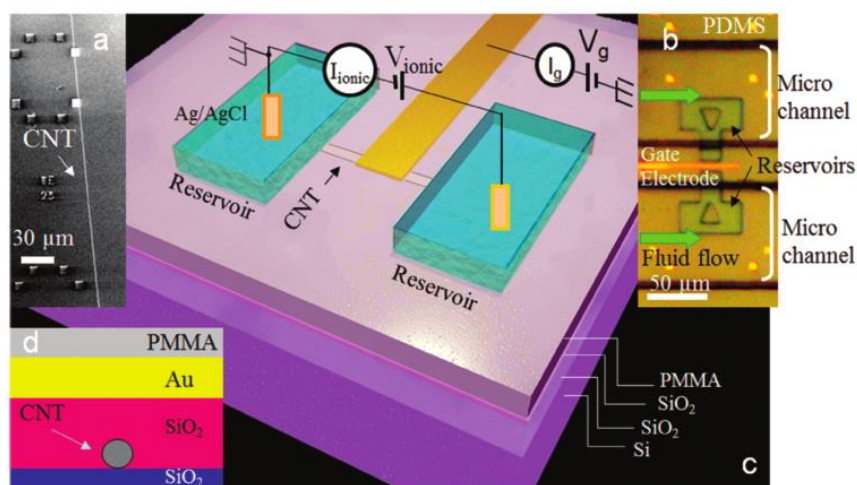


Figure 5.1.1 Horizontal single CNT device. Experimental setup used by Pang et al. to test the behavior of a nanochannel made from the interior of a single CNT which bridged the gap between two fluid reservoirs. (a) Scanning electron microscope images of a CNT on silicone oxide. (b) Optical microscope image showing a top view of the device. (c) Schematic of the device structure and electrical connections used. Reprinted with permission from Pang et al.¹⁴⁹ Copyright 2011, American Chemical Society.

The hollow interior of CNTs can be used to bridge a gap between two reservoirs in an electrochemical cell, creating a system similar to those seen in the previous chapters. In this way, synthetic nanopore systems can be fabricated which possess finely tuned characteristics and truly nanometer size scales. Importantly, the unique properties of the carbon walls and confined space they create have the potential to produce very unusual nanofluidic behaviors. Looking primarily at tubes with diameters below 10 nm, some of

most exciting results include: 1) spontaneous wetting of the CNT interior despite its hydrophobicity;^{141,142} 2) selective transport through tubes with the addition of entrance modifications;^{143,144} 3) incredibly high gas, water and proton permeation rates that can be orders of magnitude larger than other comparable pores;¹⁴⁵⁻¹⁴⁷ and 4) large complex molecules, such as ssDNA or florescent dyes can translocate through similarly sized CNTs.¹⁴⁸

Despite the work that has been done so far, some of the most fundamental physical principles governing CNT transport are widely debated in the literature.²² The first example is the true enhancement factor of CNT transport over similar pores. Researchers using a combination of membranes, molecular modeling and individual CNTs have reported values spanning a few orders of magnitude. In addition, the cause of this enhanced flow is only partially understood. Most explanations agree that it is due to high electroosmotic flow, but require additions such as surfaces charges which are difficult to fully justify.¹⁴⁹ A second example is the expected current modulation resulting from a translocating particle in a coulter counter setup. Depending on the charge and size of such a particle it is known that both current increases and decreases are possible. There is debate however, regarding which types of events can be used to justify the existence of a single conducting channel.^{150,151} Finally, the question of what carries the majority of the current remains an open question. In the work done by Strano and coworkers it is suggested that protons carry the current and the entrance of salts into the tube interior causes stochastic blocking.^{151,152} Publications by Lindsay's group, on the other hand, find that the current is carried primarily by salt ions.^{149,153} The sensitive nature and the variety of CNTs used across the community has made it difficult to elucidate and study the physics that govern transport.

In order to help answer some of the above questions, this chapter will cover the fabrication and analysis of a platform in which single CNT nanochannels are isolated and tested. Here, we build a platform in which a forest of vertically aligned CNTs are grown and then sealed on a freestanding silicon nitride (Si_3N_4 but will be abbreviated as SiN) membrane. Focused ion beam (FIB) techniques are then used to open one end of a single tube on one side, followed by reactive ion etching (RIE) which opens all the tubes on the other side. The final product is a single (or a few) active CNT channel in series with a SiN pore, which can then be placed between two reservoirs in an electrochemical cell. In parallel with experiments done using this system, theoretical simulations will be used to model transport through a similar CNT. We use methods based on first principles, molecular dynamics and continuum modeling to offer possible explanations for the nanofluidic phenomena observed in our system.

5.2 Theory

5.2.1 Structure of a CNT

Carbon nanotubes can be structurally thought of as a layer of graphene rolled up into a tube. A graphene layer consists of sp^2 bonded carbon atoms in a honeycomb lattice, shown in Figure 5.2.1 (top left). The lattice can be described through its lattice vectors, \vec{a}_1 and \vec{a}_2 , which point from one location on the lattice to a corresponding repeat of that point. In order to form the carbon nanotube, this graphene sheet can then be rolled up in many different ways. In order to describe the different rolling orientations, something called the chiral vector is defined as

$$\vec{C} = n\vec{a}_1 + m\vec{a}_2 \quad (2.2.1)$$

where n and m are integers. The chiral vector points along the direction of rolling and connects two equivalent points where the tube is completed. The integers n and m describe the number of unit lattice vectors which need to be summed in order to create the chiral vector. In the simple case where $m = 0$, the tube is rolled along the direction of a_1 and the tube is called zigzag (blue coloring in Figure 5.2.1). If we use values such that $n = m$, then the tube is rolled in a symmetrical fashion and is called armchair (red coloring in Figure 5.2.1).

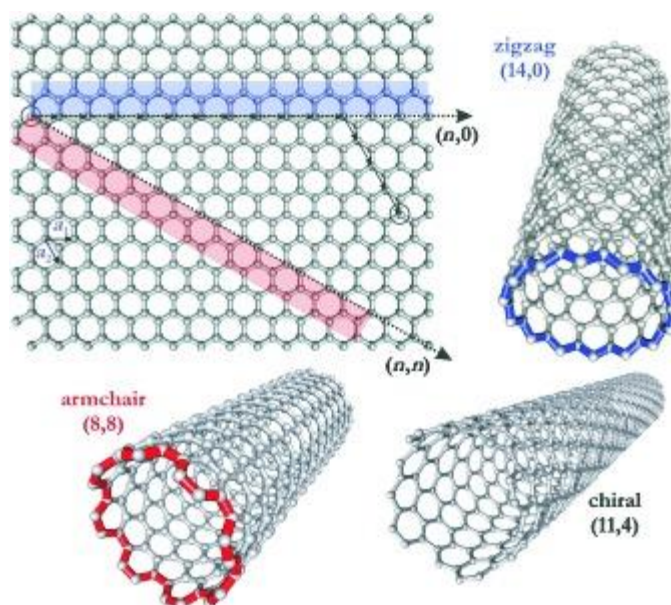


Figure 5.2.1 Structure of a CNT. Diagram showing the structure of graphene (top left) and of carbon nanotubes of different chirality. The lattice vectors a_1 and a_2 are defined as well as the chiral vector (red or blue shading). Figure courtesy of Balasubramanian et al.¹⁵⁴ Copyright Wiley-VCH Verlag GmbH & Co. KGaA. Reproduced with permission.

Both of these terms come from the pattern of the carbon bonds along the chiral vector. For all other values of n and m , the tubes are simply called chiral. Since the chiral vector is by definition a path along the circumference of the tube cross-section, it is possible to find a relationship between it and the tube diameter. This is given by

$$D = \frac{\vec{C}}{\pi} = \frac{\sqrt{3}}{\pi} a_c \sqrt{n^2 + m^2 + nm} \quad (2.2.2)$$

where a_c is the length of a carbon-carbon bond which is known to be about 0.14 nm. Figure 5.2.1 shows a cartoon representation of three different possible carbon nanotube configurations.¹⁵⁴

A carbon nanotube can consist of a single layer of graphene rolled up in the described way or it can include many. If the tube is a single sheet, it is referred to as a single walled carbon nanotube (SWCNT), if it has two layers it called a double walled carbon nanotube (DWCNT) and if it has more than two layers it is called a multi walled carbon nanotube (MWCNT). Figure 5.2.2 shows how the different layers of a MWCNT are organized. The tubes used in this chapter were primarily single walled although a small fraction of them were found to be double walled.

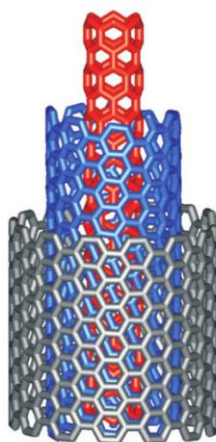


Figure 5.2.2 Multi walled CNT. Structural representation of a carbon nanotube that consists of many walls. In the case of a single walled tube, the blue and gray layers are not present. Figure taken from Balasubramanian et al.¹⁵⁴ Copyright Wiley-VCH Verlag GmbH & Co. KGaA. Reproduced with permission.

5.2.2 Electronic Characteristics of CNTs

The way in which a CNT is rolled up, as well as the number of walls, can greatly impact its electronic behavior. The electronic band structure can be solved for in a SWCNT and

shows that tubes are roughly broken up into two categories, conducting and semi-conducting.¹⁵⁵ It is found that if n and m are related by

$$\frac{(2n + m)}{3} \in \mathbb{Z} \quad (2.2.3)$$

where \mathbb{Z} represents integers, then the CNT will be conducting. In all other cases, the tube will be semiconducting with the band gap that decreases with tube diameter as $1/D$. Carbon nanotubes fabricated by chemical vapor deposition, which is the method used in this chapter will be approximately two thirds semi-conducting and one third conducting.

The focus of this chapter will be on the transport through the interior of CNTs. As a result the currents measured are not likely related to electrons traveling down the CNT walls, but instead to charged ions traveling down the tube opening. Although it might be possible for the chirality of a CNT to have some effect on the structure of molecules inside, it is unlikely to cause observable changes in our experiments. As a result of this, as well as the way in which devices are fabricated, we will not attempt to measure or monitor any of the chiral characteristics of the tubes used here.

5.2.3 Enhanced Flow in CNTs

One of the most unique characteristics seen in CNTs is incredibly rapid transport through their interiors. This has been both predicted with simulations as well as observed in experiments. As mentioned in the introduction, this fast flow has been seen for many different types of transport including that of gas, water, protons and ions. It was first predicted by scientists such as Hummer et al. who were able to simulate fast pulse like flows of water through CNTs using MD simulations.¹⁴¹ Due to the difficulty in isolating single CNTs, the majority of experimental results measuring CNT flow come from using membranes

which contain billions of open pores. One such example comes from the Hinds research group, where they showed that water transport through a membrane of MWCNTs under an applied pressure was 4-5 orders of magnitude above similar membranes.¹⁴⁶ More recently, experiments have been done on single CNTs by scientists such as Lindsey and Strano. It has been found that the ionic conductance is also greatly enhanced with values several orders of magnitude above equivalent non carbon pores.¹⁴⁹

Most of the literature agrees that this enhancement in flow stems at least in part from the hydrophobicity and molecular smoothness characteristic of carbon nanotube walls. In order to model this mathematically, the concept of slip length needs to be introduced. In Chapter 2, the Navier-Stokes equation was discussed which gives us the fluid flow resulting from different types of applied potentials. If this equation is simplified to the specific case of an incompressible fluid undergoing laminar flow through a long cylindrical pipe we get what is called the Hagen-Poiseuille equation.

$$u_{HP}(r) = -\frac{PR^4}{4\eta} \left(1 - \frac{r^2}{R^2}\right) \quad (2.2.4)$$

In the above equation the fluid velocity in the pipe, v_{HP} , is given as a function of radius, r . P stands for the pressure difference, R is the radius of the pipe and as before, η is the viscosity. To get the total flux through the tube the above expression can be integrated over the pipe cross-section to give the following.

$$J_{HP} = -\frac{\pi R^4 P}{8\eta} \quad (2.2.2)$$

In order to arrive at this equation, a no-slip boundary condition must be used. This means that velocity of the fluid is set to be zero at the pore wall, or written mathematically, $u(R) = 0$. This is an assumption that is acceptable for the pores in the first two chapters, but

CNTs are unique. Instead of using this, we can represent the smoothness of the CNT walls through the inclusion of a slip length. This can be done using the following boundary condition

$$u(R) = -L_s \frac{\partial u}{\partial r} \Big|_{r=R} \quad (2.2.2)$$

where we have introduced the slip length given by L_s . Using this new formulation, the new expression for the velocity profile is found to be

$$u_s(r) = -\frac{PR^4}{4\eta} \left(1 - \frac{r^2}{R^2} + \frac{2L_s}{R} \right) \quad (2.2.2)$$

and the corresponding expression for flux is given below.

$$J_s = J_{HP} \left(1 + \frac{4L_s}{R} \right) \quad (2.2.2)$$

It can be seen that through introducing the slip length, we have made it possible to model enhanced flow rates through selection of a fitting value for L_s . With this formulation, the enhancement factor of CNT flow can be defined as the ratio of the observed flow to the flow predicted by the Hagen-Poiseuille law. For a thorough summary of the different enhancement factors present throughout the literature, the reader is directed to a recent review by Guo et al.²² The physical interpretation for these very long slip lengths present in CNTs is still a topic of interest in the field, but one possible explanation involving a depletion layer with reduced viscosity near the pore wall is given by Tim Myers.¹⁵⁶

5.2.4 Limitations of the Continuum Models in CNTs

All of the mathematical modeling of transport through nanotubes so far has been based on a continuum formulation. This means that the finite size of particles is not taken into consideration. In order for this to be true, the size scale of our system must significantly

larger than the size of individual molecules. One useful parameter which helps determine this is known as the Knudsen number. It is defined as

$$\text{Kn} = \frac{l}{L} \quad (2.2.2)$$

where l is the mean free path of a particle and L is the smallest physical length of a system. For our system, we can plug in the mean free path of water (~ 0.3 nm) and compare it to the diameter of our CNTs (~ 3 nm) to get a value of Kn equal to 0.1. This is a somewhat safe regime for a continuum approach, but not if the tube diameter is decreased by a significant amount. A second parameter which can be looked at is the Debye length. At high concentrations such as 1 M KCl, it approaches a value of 0.3 nm which is on the same scale as the mean free path of particles in our system. As a result some care needs to be taken in using the continuum approach here.

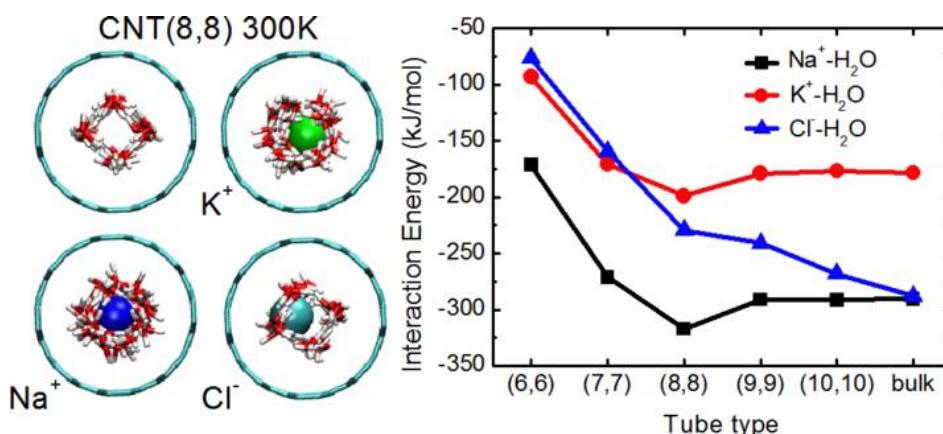


Figure 5.2.3 MD simulation inside a CNT. Cross-sectional images of the radial distribution of Na⁺, K⁺ and Cl⁻ ions in an (8,8) CNT (left). Graph of the interaction energy within a range of 1 nm for Na⁺-H₂O (black), K⁺-H₂O (red) and Cl⁻-H₂O (blue) for several different CNT types (right). It can be seen that tube structure can have a large impact on the interactions between molecules in the tube. Reprinted with permission from He et al.¹⁵⁷ Copyright 2013, American Chemical Society.

Additional issues with the formulation so far involve ignoring interactions between the particles in our system. It has been shown that under the confinement of small CNTs, water and salt molecules can take on very unique organizations due to their hydrogen

bonds.^{157,158} Figure 5.2.3 shows one example of this in which chiral tubes containing water and either K^+ , Na^+ or Cl^- were modeled. It can be seen that the interaction energy and as a result the structure of the molecules differ greatly as the tube diameter changes, with the (8,8) tube being the most unique. It is also known additional interactions between ions, water molecules, and the carbon atoms in the tube walls take place such as cation- π bonds.¹⁵⁹ Ignoring these interactions can result in models which are lacking in terms of accurately describing transport through a CNT. Near the end of this chapter, we approach this through first principle and MD simulations that attempt to more accurately examine the structure of salt ions inside our CNTs.

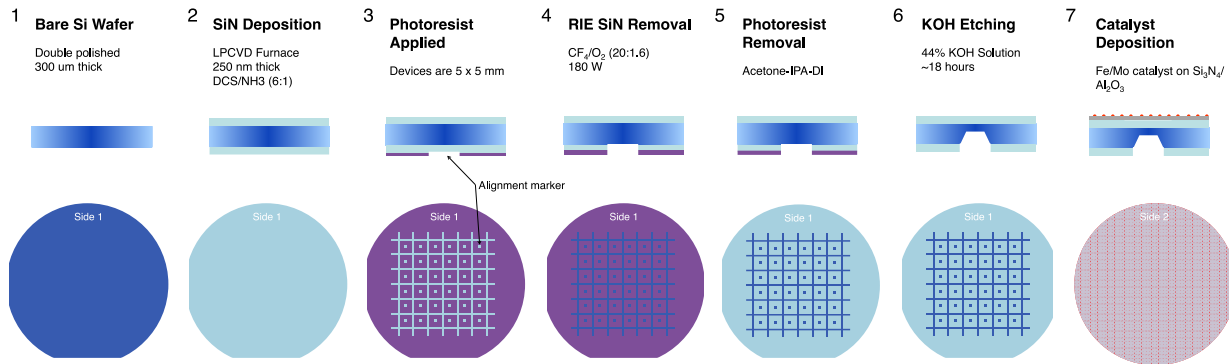
5.3 Experimental Setup

5.3.1 Device Fabrication

Devices fabrication can be described in two stages, those done at the wafer scale, and those done on an individual device scale. Starting with a double polished 300 nm thick Si wafer (100), a 250 nm thick layer of SiN is deposited using standard low pressure chemical vapor deposition (LPCVD) techniques. Next, AZ1518 photoresist is spun onto one side and standard photolithography is used to expose a grid like pattern that defines the 5 mm x 5 mm chip size. The entire side then undergoes reactive ion etching (RIE) using CF_4 and O_2 (20 sccm and 1.6 sccm respectively) at ~ 0.3 Torr and 180 W in order to remove the SiN under the exposed pattern. Photoresist is then removed using an acetone IPA cleaning and the wafer is left in 44% KOH solution for 18 hours at $65^\circ C$. Finally, the smooth side of the wafer is used for catalyst deposition. Using electron beam lithography a catalyst layer (details in section 5.3.2) is deposited on top of the SiN.

Device Fabrication Steps

Whole Wafer Steps



Individual Device Steps

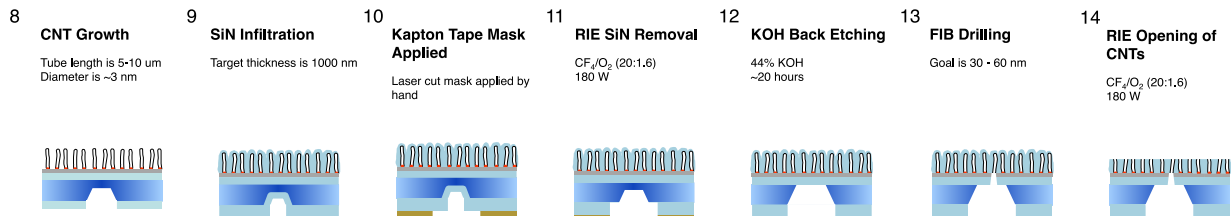


Figure 5.3.1 CNT Device Fabrication. Schematic of the fabrication process for our ssDNA platform. Starting with a bare Si wafer, a 250 nm layer of SiN is deposited and photolithography and etching in 44% KOH solution is used to define the device shape. A catalyst layer is then deposited on the entire wafer. The remaining steps are done in individual 5 x 5 mm devices (sometimes in batches). CNT growth via CVD is followed by SiN infiltration using LPCVD. A Kapton tape mask is applied to remove remaining SiN and KOH etching exposes the CNT supporting membrane. FIB is used to drill a ~60 nm diameter pore followed by RIE which exposes all the tubes on the opposite side.

Following catalyst deposition, the wafer is broken up into the pre-patterned 5 mm device squares and placed in a tube furnace for CNT growth (details in section 5.3.2). Following growth of a vertical CNT forest, LPCVD is again used to infiltrate the gaps between tubes and seal the membrane. After this step, a Kapton tape mask outlining a 1.5 x 0.5 mm window is placed on the backside (non CNT side) and RIE is used to remove the exposed SiN. The device is then placed in a Teflon cell which makes it possible to expose only the backside to 44% KOH. Overnight incubation results in the removal of Si material creating a freestanding SiN membrane with the CNT forest on top. With the SiN membrane exposed, it is now possible to use FIB to drill a 20 to 100 nm sized pore reaching a single (or a few)

CNT(s) on the other side. As a final step, RIE is again used to remove the excess SiN layer on top of the CNTs resulting from the initial infiltration. This process also removes the closed CNT caps, opening all the tubes on that side. The result is a FIB drilled pore in series with a single (or a few) open CNT nanochannel(s).

5.3.2 CNT Growth

CNT growth begins with the deposition of a multilayer electron beam (Semicore SC600) deposited catalyst layer. The layers are sequentially added at a constant pressure below 1.6×10^{-6} Torr and consist of 30 nm of aluminum oxide followed by 0.05 nm of molybdenum (Mo) and 0.55 nm of iron (Fe). Due to the very thin films used, the given values, especially of the latter two are what is reported by the thin film deposition monitor and can vary slightly from actual thickness. Using Rutherford backscattering spectroscopy (RBS) on a representative sample gave thicknesses of 0.42, 0.06 and 30 nm for Fe, Mo and aluminum oxide respectively.

Following catalyst deposition, vertically aligned CNT forests are grown using a thermal CVD tube furnace (Lindberg Blue M Mini-Mite, Thermo Scientific). Prior to growths, the tube is kept at 120° C with water vapor monitored and kept below 20 ppmv. The devices are placed inside and the tube is purged with 1000° sccm of He for 10 minutes. Next, the temperature is raised to 850° C while the sample is exposed to an atmosphere of 515 sccm of He and 400 sccm of H₂. Once this temperature has stabilized, it is held in this state for 10 minutes in order to facilitate annealing which creates nanoparticle growth sites. The temperature is then brought down to 750° C, and the sample is ready for growth. A flow of 100 sccm of Ethylene is added to 15 sccm of H₂ and 515 sccm of carrier He is maintained

until the desired tube length is achieved, which in this study was a height of 6-12 μm . Following growth, the samples are slowly cooled down to room temperature in an atmosphere of He (515 sccm).

5.3.3 CNT Characterization

Characterization of CNT forests was carried out using several different techniques, the first of which was scanning electron microscopy (SEM). Samples were sometimes sputtered coated with a thin layer of gold and then imaged using a cold cathode JSM-6333F SEM. Samples were examined top down as well as broken in half and looked at via cross-section. Next, high-resolution transmission electron microscopy (TEM) was used to quantify CNT diameter distribution and to count the number of tube walls. A JOEL 2100-F field emission analytical TEM, operating at 120 kV and 200kx magnification was used. Samples were prepared by dispersing CNT forests into ethanol and using ultrasonication to separate tubes followed by dropcasting the dispersion onto Cu TEM grids coated with Formvar. The final method of characterization used was Micro-Raman spectroscopy using a Nicolet Almega XR dispersive Raman spectrometer (Thermo Scientific). An excitation wavelength of 633 nm and a 100x objective magnification was used and produced a sub μm spot size.

5.3.4 Leak Testing

In order to ensure there were no alternate pathways through a SiN infiltrated forest, the devices underwent control testing at several points during the fabrication process. Both before and after FIB was performed, the devices were loaded into an electrochemical cell and the conductance across the membrane was measured at 1 V in 1 M KCl. If the current was

larger than 100 pA the device was considered to have a leak and was not used. Additionally, SEM cross-sectional images were used to evaluate the quality of the SiN infiltration for a representative device from each batch. If the quality visually looked poor, the rest of the devices in the batch were not used.

5.3.5 Data Acquisition and Analysis

Data acquisition was done by loading the CNT device into a molded PDMS cell (Figure 5.3.2) which contained two reservoirs isolated by a CNT/SiN membrane fabricated as described above. Ag/AgCl pellet electrodes (A-M Systems) were inserted into either side and the current across the membrane was recorded in the presence of an applied voltage. This was done using either an Axopatch 200B amplifier connected to a 1550 Digitizer (Molecular Devices) or HEKA EPC 10 (HEKA Electronics). Data analysis was done using Clampfit 10, Matlab 2012b and Origin 9.0. During voltage sweeps, voltage was held at each value until current was stable and I-V curves were generated by taking the average and standard deviation of the current calculated over the final 2 seconds.

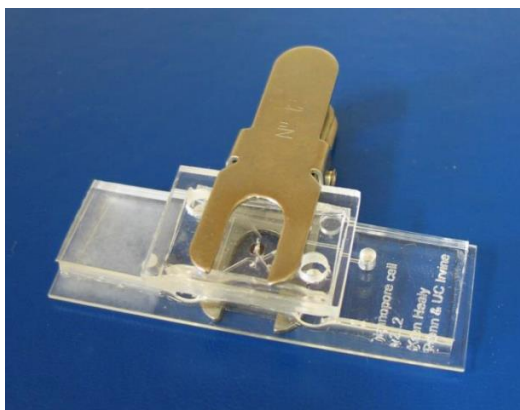


Figure 5.3.2 PDMS electrochemical cell. Photo of the PDMS conductivity cell that was used to take measurements in our CNT devices. The device is sandwiched between two layers of PDMS with the CNT forest perpendicular to the largest PDMS surface. Picture courtesy of Matt Davenport.

5.3.6 Molecular Simulations

To understand the structure of KCl solution under confinement, first-principles MD simulations were performed. Confined KCl solution inside a CNT was represented by a tetragonal supercell constructed from 4 repeats of the (19,0) CNT primitive unit cell, with the dimension of $a = b = 21.17 \text{ \AA}$, $c = 17.06 \text{ \AA}$. The supercell contains one KCl pair and 52 water molecules in a $d = 14.0 \text{ \AA}$ diameter CNT, yielding a 1.0 M concentration salt solution with the bulk water density. Born-Oppenheimer molecular dynamics (BOMD) simulations were carried out using Qbox¹⁶⁰ with interatomic forces derived from density functional theory (DFT) and the Perdew, Burke, and Ernzerhof (PBE) approximation for the exchange-correlation energy functional.¹⁶¹ The interaction between valence electrons and ionic cores was represented by norm-conserving pseudopotentials,¹⁶² and the electronic wave functions were expanded in a plane-wave basis set truncated at a cutoff energy of 85 Ry. All hydrogen atoms were replaced with deuterium in order to maximize the allowable time step and a time step of 10 a.u. was adopted in all simulations. Models of bulk and confined solutions were equilibrated at a constant temperature $T=400^\circ \text{ K}$ for 15 ps and 5 ps, respectively.

Classical simulations were also carried out to examine the performance of different force fields and the effect of specific interactions on the structures of confined ions, and results were compared with those derived from first-principles. Both non-polarizable and polarizable force fields were considered with and without cation- π interaction. Specifically, we employed OPLS-AA for ions^{163,164} and a SPC/E water model¹⁶⁵ for non-polarizable force fields. Polarizable force fields simulations were carried out using the SWM4-NDP water model¹⁶⁶ and polarizable ions as well as a CNT.¹⁶⁷ Finally, cation- π interactions were also included using polarizable force fields.¹⁶⁸ Statistics were collected over 2 ns NVT simulations.

Ionic conductance in nanopore structures mimicking the actual nanofluidic devices were calculated by numerically solving coupled Poisson, Nernst-Planck, and Navier-Stokes equations using COMSOL, with and without slip boundary conditions at the CNT inner wall.

5.4 Results and Discussion

5.4.1 Demonstration of a Successful Device

The nature of single ion channel experiments and the design complexity required to isolate a single carbon nanotube make it important to ensure a successful device following fabrication. In order to maintain high control over fabrication, characterization from devices following several of the fabrication steps was done. A summary of these tests is shown in Figure 5.4.1 for CNT forests, CNT/SiN composites and FIB drilled pores. First, Raman spectroscopy was done following the growth of a vertical CNT forest. The most important indicator was the ratio of the G band (1582 cm^{-1}) to the D band (1350 cm^{-1}). This gives a good measure of the quality of the CNTs with the G band representing sp^2 bonded carbon and the D band representing defects in the CNT structure.¹⁶⁹ Samples were considered to be high quality forests if the G/D was in the range of 6-8. Following Raman analysis, cross-sectional SEM images of the CNT forests were used to verify vertical alignment and provide a rough estimate of tube density. An example spectrum and SEM image are both shown in Figure 5.4.1 part b. As a final method to monitor tube quality, forests were then dispersed in EtOH and imaged using TEM. Along with verification of the tube structure, TEM analysis makes it possible to record the tube diameter distribution which is a good indicator of the catalyst deposition thickness. A representative distribution as well as a sample TEM image is shown in Figure 5.4.1 part a.

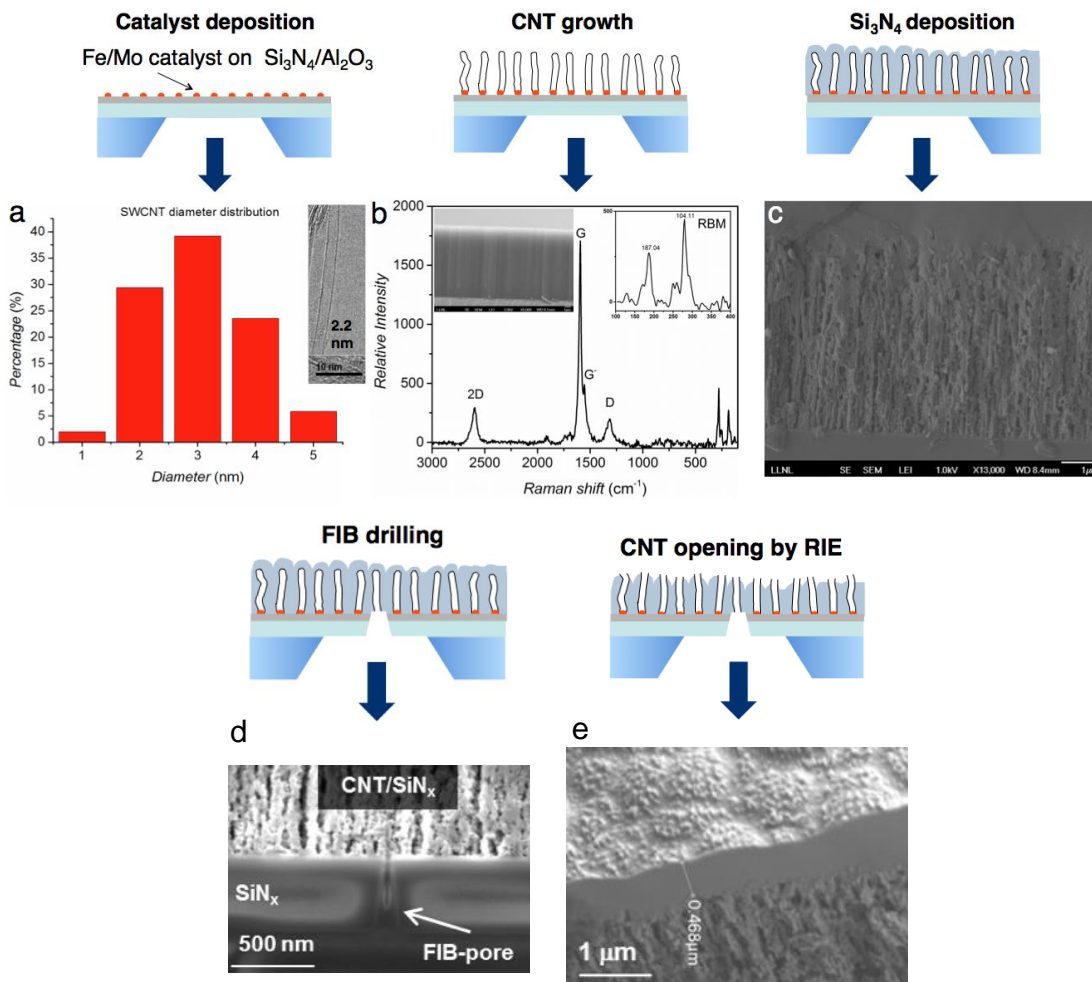


Figure 5.4.1 CNT device characterization. Characterization of representative devices at different steps in the fabrication process. a) TEM analysis of CNT tube diameter which is directly influenced by catalyst deposition thickness. b) SEM and Raman analysis show successful growth of a vertically aligned CNT forest. c) SEM images show successful infiltration of SiN between tubes as well as the formation of an excess layer on top. d) Cross-sectional SEM image following the drilling of a pore using FIB show that only a few tubes are activated. e) SEM images following RIE etching on the side with the excess layer of SiN showing the exposed tips of the CNTs. SEM images courtesy of Shirui Guo.

Following infiltration of the CNT forest with SiN using LPCVD, a random sampling of devices were broken in half and a cross-section SEM image was taken. Using this method it is possible to make a rough visual observation of how complete the gaps between the tubes were filled in (see Figure 5.4.1 part c). In all cases, the formation of a solid SiN layer was observed on top of the CNTs that was about 900 nm thick. SEM images following RIE (Figure

5.4.1 part e) show that when only a few hundred nm of the layer is removed, tubes can be seen protruding through suggesting the forest extends into the solid SiN layer. We believe this layer is instrumental in sealing transport across the membrane and only after excessive etching can some gaps be seen. Finally, Figure 5.4.1 part d shows cross-section images following the FIB drilling of a pore in the SiN layer supporting the CNTs. To get these images, the FIB pore was first drilled, then a larger area of material was milled away until a cross-section of the pore was visible. It can be clearly seen in the image, that not only is a well defined FIB pore successfully created in the SiN, but that it is also in contact with the CNT forest on the other side.

In order to test for the presence of leaks in our system, we also subjected our device to several electrochemical control tests. We did this by measuring the current across the CNT/SiN membrane in various states of fabrication. Testing was first done in devices which had yet to undergo KOH etching and were therefore several hundreds of microns thick (consisting of Si). Occasional leaks were observed during this step that we were able to mostly remove through cleaning of the PDMS cell surface to ensure a tight seal was formed at the SiN interface. We believe this step is especially important since it has been previously shown that small channels in PDMS interfaces can form and even show stochastic blocking behavior.¹⁷⁰ The next control test was done following the KOH etching step, which results in a free standing SiN support in contact with a SiN/CNT composite. This was to check for any possible cracks in the SiN membrane caused by the stress of KOH etching and failed devices at this stage were rare. Finally, currents were measured following the FIB drilling of a small pore in the SiN membrane. Large currents here would indicate a possible leak through the CNT/SiN matrix and were also found to be rare. In all cases, if currents at 1 V in 1 M KCl were

observed to be above 100 pA, a device was considered to have failed the control test. Devices which successfully passed all of these steps were then opened on the CNT side using RIE and retested. Successful devices showed an ionic current only after this final fabrication step.

As additional proof of interior CNT conductance, translocating particles were used. Based on the idea of the coulter counter, the addition of particles with known diameter to one side of the CNT allowed them to be driven through with an applied voltage. Single amplitude blockade events indicate the conductance of only one channel and give some information on its size. If multiple blockades are seen, or no blockades are present, it is evidence that the channel is not working as intended. Using this technique, we were successfully able to observe single amplitude blockades after the addition of PEG in many of our devices. Example current traces of these PEG events are shown in Figure 5.4.2. It is also worth noting that PEG is an uncharged molecule indicating the presence of significant electroosmotic flow. Further evidence of this type of current will be given later in this chapter. Further characterization of these translocation events is planned in future work.

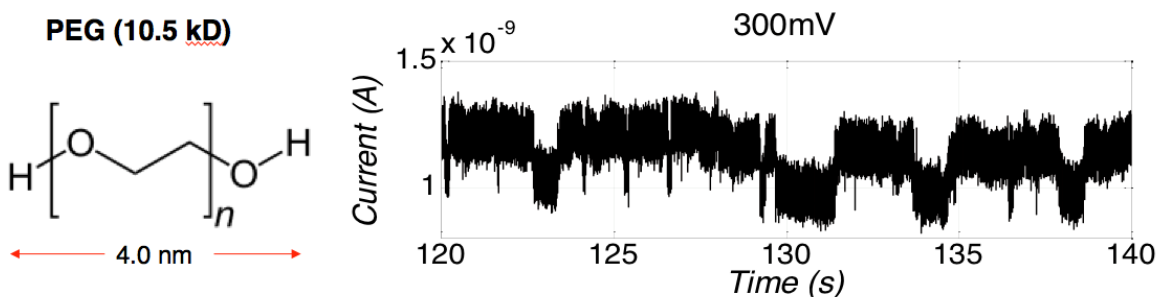


Figure 5.4.2 Translocation through a CNT. (left) Structure and size of a 10.5 kD PEG molecule and (right) current traces showing particle translocation through a CNT channel where single level blockades can be seen.

5.4.2 Ionic Transport in a CNT

Once the success of our device fabrication had been validated, we turned to the analysis of conductance through a CNT. We thoroughly investigated the current-voltage characteristics of our CNT channel as a function of the solution concentration, pH and field strength. Starting first with the pH, Figure 5.4.3 shows the ionic current recorded across a range of different pH values. The data clearly show that there does not seem to be a significant correlation between the magnitude of the current and the pH. More specifically, as pH decreases the current does not show a strong upward trend. Any patterns we did observe were inconsistent between devices and the magnitude of variation were incredibly

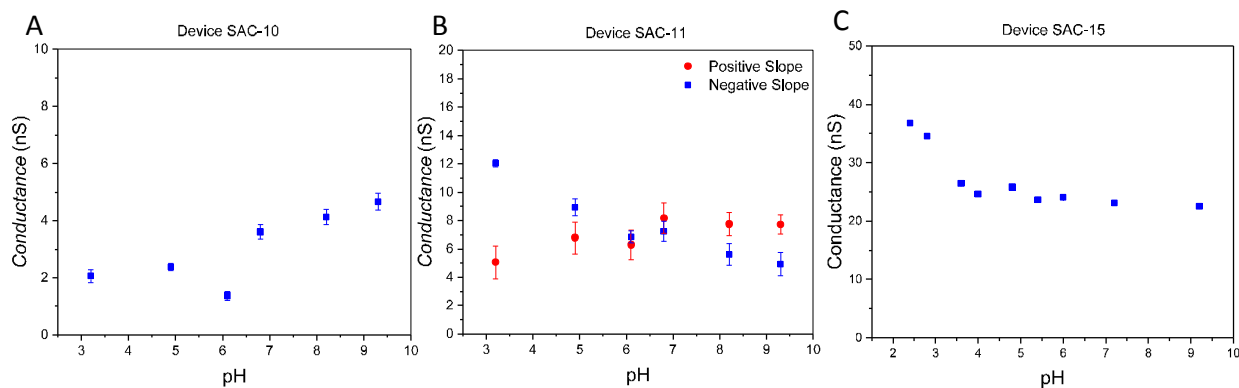


Figure 5.4.3 Conductance vs pH. Conductance as a function of pH for three different CNT devices. Plots (A) and (C) have their conductance values taken from the entire I-V curve while (B) has the slope over positive and negative voltages calculated separately. In all cases there is very little change in conductance, especially considering pH is the log of the proton concentration.

small considering that pH is based on the log of the proton concentration. The device in Figure 5.3.4 part B was unique in that it showed some non-linearity in its I-V curves that changed as a function of pH, but even still these changes are small given the pH range. This tells us that in our system, the dominating current is almost certainly not derived from the transport of protons. This result matches that of some groups in the literature, such as work from Lindsey's group, but it is in direct opposition to the work of Strano's group. It is not entirely clear where the difference is originating from, but it is worth noting that the CNTs

used by Strano's group are significantly longer and have slightly smaller diameters. The tubes used by Lindsey however, much more closely resemble our own. It is possible that the length of a CNT can play a role in determining the dominating charge carrier. It is also worth noting that when doing experiments with salt ions, stochastic blocking due to ion translocation, similar to that reported by Strano's group, was not observed. This further suggests that our system is not dominated by proton transport.

Next, we looked at the magnitude of the current resulting from salt ions in solution. The studies done here used KCl dissolved in deionized water (DI) at concentrations spanning many orders of magnitude. Since our system consists of both a SiN pore and a CNT in series, it was important to verify that any observed behavior was dominated by the CNT. To test this we did our experiments using devices both with and without the CNT forest. The results are summarized in Figure 5.4.4 for both of these cases. Part A shows that when using a SiN nanopore between 54 and 105 nm, the results match what is expected for a charged pore. As previously discussed, when a pore carries a surface charge, one of the expected behaviors is a leveling off of the conductance as the salt concentration drops. The surface charge is able to maintain an artificially high salt concentration in the pore and as the bulk concentration drops, causing the Debye length to increase, an equilibrium is eventually reached. In our data the beginning of this effect can be seen starting at roughly 10 mM KCl. At 10 mM the Debye length is roughly 3 nm, which is sufficient to impact conductance. When the data from these devices is fit to equations describing traditional pore transport¹⁷¹ we were able to successfully generate surface charge densities expected from SiN as well as diameters that matched with our SEM analysis. The predictability of these reference devices serves as a

nice control test as well as allow for a direct comparison against their CNT containing counterparts.

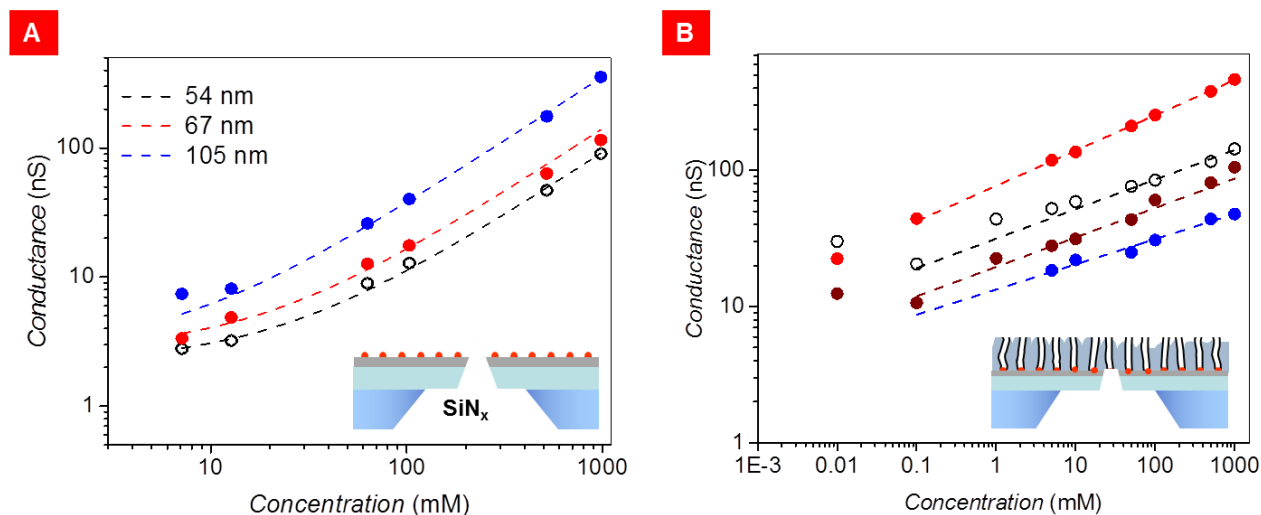


Figure 5.4.4 Conductance vs KCl concentration. Plots of the ionic conductance dependence on concentration. (A) Devices which do not have the CNT forest and consist of a SiN pore alone show expected linear behavior which levels off at low concentrations. (B) Devices which have CNTs show anomalous ionic conductance that follows a sub-linear power law with an exponent between 0.18 and 0.26. Insets show a diagram of the devices used in each plot

When devices which have a CNT in series with the SiN pore are tested, the results are significantly changed. This can be seen by looking at Figure 5.4.4 part B which shows a summary of the CNT data. There appear to be two profound behaviors due to CNT transport phenomena. The first is a very large overall magnitude of the current and the second is a unique power law dependence of conductance on KCl concentration. The measured conductance, above 100 nS at 1 M KCl, is many orders of magnitude above what would be expected from a classical pore that is of a similar shape and size. For reference a classical uncharged nanopore with a diameter of 3 nm and a length of 10 μm would have a conductance at 1 M KCl of only 30 pS (ignoring entrance resistance). Comparing these two values gives our system an enhancement factor of roughly three orders of magnitude. This huge conductance is in line with other literature as well as with most simulation work. It is

worth noting however, that there is a huge spread in the reported CNT enhancement factor and it remains a mystery as to why it is so large.

The second clear difference over the SiN control device is the power law dependence of the conductance. Rather than the linear relationship that levels off at low KCl seen in the control case we observe a power law dependence, with an exponent between 0.18 and 0.26, that is consistent over a huge range of KCl concentrations. Tests were done at concentrations down to 10 μM and the power law dependence was clear down to around 100 μM . We believe that as the KCl concentration reaches extremely low values, the behavioral effects of the SiN pore will dominate, which may be happening at the 10 μM data point. This power law dependence again only matches a small subset of the current published literature in the field. Lindsey's group is the only other to report this type of unique power law behavior. It is not yet known for certain where these unique phenomena originate, but the leading idea is based on the high electroosmotic flow predicted in CNTs.

5.4.3 Evidence of Electroosmotic Flow

Published work, both based on simulations and experimental data, attribute many of the unique characteristics seen in CNTs to having very large electroosmotic flow. This is generally said to originate from the smooth graphitic surface which creates a very long slip length combined with the presence of some surface charge. Direct experimental confirmation of this has been somewhat difficult and lacking as it can be hard to decouple the different types of possible transport. Some experiments have attempted to measure the electroosmotic velocity, but the reported values show huge variability.²² Additionally, it is not clear where a strong surface charge on the pore wall could originate. It is worth noting

that the ends of a CNT have carboxyl groups which result in a negative charge. The magnitude and location of charges sufficient to produce strong electroosmotic flow in most simulation work however, goes well beyond what could be provide by the CNT ends. Due to these concerns, the explanation and magnitude of electroosmotic current in CNTs is still up for some debate.

The unique geometry of our platform allows for verification of electroosmotic flow. Because our system consists of two pores in parallel, it gives us a way to observe the electroosmotic effects of one channel induced on the other. From Figure 5.4.4 it can be seen that the devices with CNTs in series with a FIB pore have conductance values that are often larger than the reference devices with only FIB pores of the same diameter. Interestingly, this seems to be in direct contradiction with the standard resistance in series method for calculating the system conductance. This unexpected result can be explained by the presence of electroosmotic flow through CNTs that is much larger than that of a regular FIB pore. Solving the full PNPS equations for two pores that are connected in series shows that the electroosmotic flow of one induces electroosmotic flow in the other to produce an overall averaging effect. This means that the CNT induces a large electroosmotic current in the FIB pore, making it possible to achieve currents higher then with the FIB pore alone.

To validate these claims, we have performed continuum calculations and quantified ionic conductance for a setup similar to our experimental device. A single 30 nm FIB pore was compared to a FIB pore of the same size in parallel with a 4 nm diameter 1 μm long CNT with a surface charge of 1 electron charge per nm^2 . The ionic current at -1 V was calculated using a slip length of both 0 and 100 nm and is shown in Figure 5.4.5. It can be seen that in the no slip case, the FIB/CNT pore combination has a much lower conductance than the FIB

pore alone. In the presence of a large slip length, however, the FIB/CNT pore is able to maintain a conductance that is actually larger than the FIB pore alone. This helps to validate the large conductance values observed in our system and show that their mostly likely origin is due to large electroosmotic current in CNTs. We hope, in future work to arrive at a more

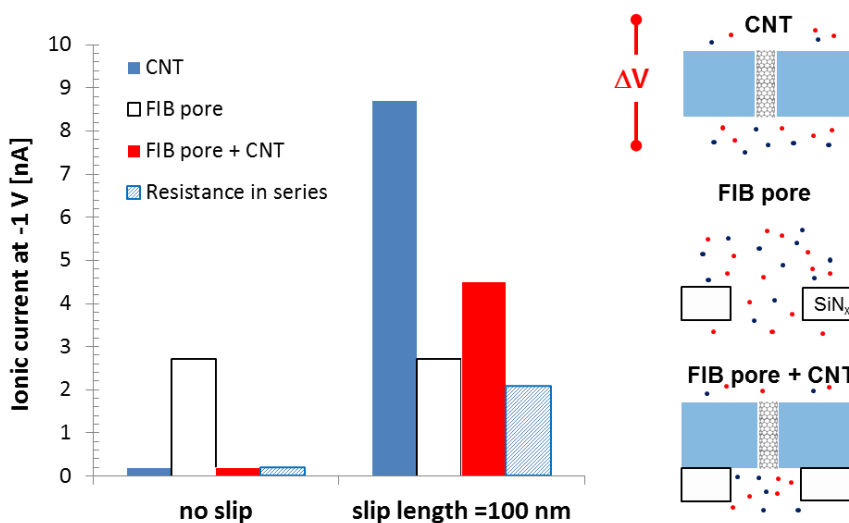


Figure 5.4.5 Electroosmotic flow. Comparison of ionic currents predicted at -1 V for a system with a SiN pore, a CNT channel and a CNT-SiN in series pore. The CNT has a diameter of 4 nm and a surface charge of 1 electron per nm² and is shown with and without slip. The SiN pore has a diameter of 30 nm and a length of 280 nm. Predictions are shown using both a full PNPS simulation as well as a traditional resistor in series model.

quantitative comparison through more accurately comparing our systems. It should be noted that the continuum model used here predicts some rectification in a plot of I-V which is not generally seen in our system. The data presented is taken for the most conductive voltage polarity to emphasize the impact of electroosmotic flow but further work is still needed to find the source of this discrepancy. Like most other simulations done, this model also leaves lingering questions related to the origin of such a strong surface charge on the CNT walls, which is a question we hope to address in the next section through MD simulations of ions in a CNT.

5.4.4 Simulation Suggests Origin of Electroosmotic Flow

In order to obtain some information on the origin of electroosmotic flow in CNTs, first principle and classical MD simulations were performed. More specifically, we looked at the structure that was induced when salt ions dissolved in water were placed inside a CNT. A 1.4 nm diameter single walled CNT was filled with a solution representing 1 M KCl and the resulting radial distribution of the molecules were computed. The radial distributions as well as molecular snapshots are shown in Figure 5.4.6. It was found that both K^+ and Cl^- ions tended to remain close to the carbon surface but the potassium ion was notably closer. The radial density distribution of the potassium ions was very narrow and indicates a strong interaction with the CNT wall. Additionally it suggests that the K^+ cation may be desolvated. As a result of this attraction, the MD simulations show the formation of localized negative polarization charges on the carbon atoms located near a K^+ ion.

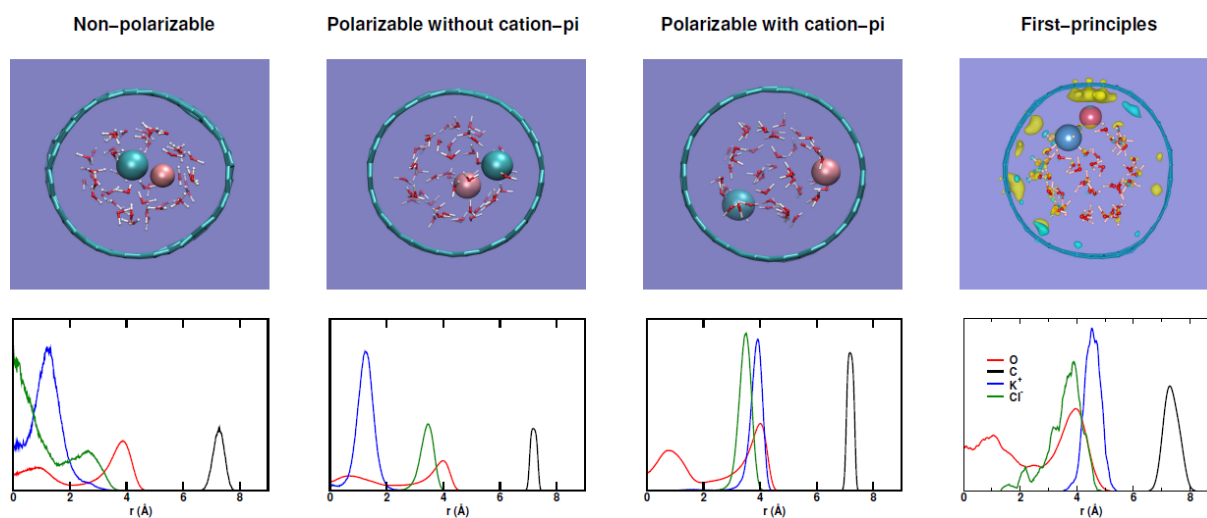


Figure 5.4.6 MD simulations of KCl in a CNT. First principle and classical MD simulations of KCl solution inside a 1.4 nm CNT. Images in the top row are snapshots of MD trajectories with Cl^- (light blue), K^+ (violet), oxygen (red) and hydrogen (white) ions along with negative and positive polarization charges in yellow and blue respectively. The bottom row shows radial distribution functions for oxygen, K^+ and Cl^- molecules using, from left to right, classical MD and non-polarizable fields, classical MD with polarizable force fields, classical MD with polarizable fields and cation- π interactions and first principle MD simulations. Image courtesy of Anh Pham.

To study this effect further, simulations were carried out using different classical MD simulations to see if the effect was still present. It was found that in order to correctly capture this unique cation behavior, both polarization and cation- π effects were needed. This indicates that ion-carbon based interactions cannot be left out of future CNT related simulations. Additionally, some initial calculations were done using NaCl. It was found that sodium ions did not exhibit this unique behavior, with the Na⁺ ion actually farther away from the carbon wall than the Cl⁻. In future work we hope to verify this claim experimentally by running tests with different salts.

We believe that these observations might shed some light of the origin of surface charges present on seemingly uncharged graphitic walls. The unique structural behavior of K⁺ cations seems to induce a type of surface charge on the CNT walls resulting from charge polarization. This charge imbalance could then, in part or in whole, be the source of the missing charge in CNT simulations. If so, it could help explain the huge magnitude of electroosmotic current observed in CNTs. Importantly, more simulation work needs to be done in order to bridge the gap between ion structure inside the tube and measurable ionic currents. It would also be particularly interesting to compare the conductance of CNTs using both NaCl and KCl. Future work planned on this topic will include such experiments and hopefully provide an explanation to the long running questions regarding large CNT conductance.

5.4.5 Interpretations of a Work in Progress

The work presented in this chapter is part of an ongoing project and as such the results should be interpreted accordingly. Every effort has been made to accurately and

consistently report the data. The nature of single CNT experiments, however, results in a large amount of experimental complexity and inconsistency. As we continue to fabricate and test devices we will thoroughly compare behaviors with those seen in previous devices to both verify the claims in this work and continue to further our understanding of CNT nanofluidic phenomena.

5.5 Conclusion

To summarize, we have presented a novel platform which can isolate a single or a few CNT channel(s) for analysis. By growing a vertical CNT forest on a SiN membrane, we have the capability to activate single CNT nanochannels using FIB nano-milling technology. This fabrication method is ideal because the large CNT membrane fabrication technique side-steps the need to position or otherwise manipulate single CNTs which is a requirement in most other systems. Additionally, it allows for the opening of anywhere from a single, to billions of tubes within the same device by simply increasing the SiN membrane opening size. Following the fabrication of our device, we first subject it to many control tests to ensure the absence of leaks and that transport is through a CNT interior. We then work to help elucidate some of the long-standing questions regarding CNT transport and aim to reduce the inconsistencies seen in the literature.

We first demonstrate a distinct lack of pH response when measuring pore conductance, suggesting that protons do not supply the current. We then show a summary of data using KCl solutions that suggest our CNTs have both a very large conductance and a power-law dependence on salt concentration, in line with some reported literature. Next we are able to demonstrate a unique type of evidence in support of electroosmotic flow through

CNTs, resulting from the FIB and CNT channels being in parallel. Finally we perform simulation work that provides a possible explanation for the large electroosmotic flow needed to explain the behavior in this chapter. Despite agreement that electroosmosis is involved with CNT phenomena, the question of where the needed surface charge originates has remained. Our modeling shows that unique ion behavior under confinement may result in a type of effective charge on the CNT wall.

Despite the work done in this chapter, the project is still incomplete and remains ongoing. Several questions remain regarding topics such as the effect of length on transport modes, the apparent difference between CNT membranes and individual CNT channels, the relationship between salts used and conductance measured and the physics governing the translocation of large molecules such as DNA. We believe our platform allows for the necessary experiments to be performed and in future work we plan to test many of these questions.

The amazing phenomena observed in CNTs makes them great candidates for many types of high performance devices such as miniaturized ultrasensitive detection systems, separation systems and energy storage based nanomaterials. The development of technologies such as these, however, is dependent on a successful understanding of how and why CNTs behave the way that they do. Studies such as the one presented here are essential to testing these core concepts and much work is still needed. As the CNT community is able to identify the source of the wide variability in the literature and agree on the physics behind CNT behavior, many new types of exciting technologies have the potential to be unlocked.

Chapter 6: The Future of Nanopore Research

Over the course of this thesis we examined the fundamental properties present in a variety of different types of nanochannels. Starting with the study of biological pores found in nature, we moved on to produce synthetic analogs and study their unique behaviors. Researchers have developed many different materials and methods which can produce synthetic nanopores, of which a few are used here. In all cases, there remains a gap in our understanding of what governs nanopore behavior, which is the focus of many scientists around the world, including those involved with this thesis.

In Chapter 3, the physical principles governing transport characteristics through α -hemolysin were studied. It was found that we could successfully model many elements of the transport and as a result predict ways to interact with it. We also demonstrated an ability to modify DNA strands to influence their transport speed. This is important because these bacterial pores have shown great promise for many technologies, most notably DNA sequencing. The ability to read DNA with incredible speed and portability are very appealing. Through this technology, the future holds a world where every person can quickly and easily acquire his or her entire genome, exposing huge amounts of useful health related information. Knowing a patient's genetic predispositions can improve the ability of medical professionals to make correct decisions.^{172,173} Further, through the addition of other natural proteins found in nature, nanopores could potentially allow for alterations to the molecules they probe such as substituting one gene for another. In order for any of this to be possible however, we must continue to study and unwrap the remaining mysteries surrounding biological nanopores.

In Chapter 4, a type of synthetic nanopore was fabricated providing the foundation for additional pore modifications. Using PET films subjected to the track etching technique, simple conical pores were made with tip diameters on the true nanoscale. The structure of these pores is simple enough that a clear model for transport can be developed. With that in hand, we can then use a bottom up approach to increase the complexity of the pore and influence its behavior. It was shown that through the addition of DNA molecules attached to the pore walls, a nanopore gate was fabricated. The synthetic gate designed was able to respond to multiple stimuli as well as show complete sterically induced closure, bringing us one step closer to truly mimicking biological gates. Advanced man-made nanopore gates promise to have applications in drug delivery systems and biosensor applications as well as teach us how natural gates work.^{21,174} The road to synthetic gating systems that truly match their natural counterparts is still long however, the rate at which ground is being covered continues to increase.

Finally, in Chapter 5, a third and unique type of pore was examined. Single and double walled carbon nanotubes were grown and individually activated to study the transport properties through their interiors. CNTs are a very unique type of nanochannel which have demonstrated amazing characteristics such as transport orders of magnitude beyond similar pores. These properties make them instrumental to advances in technologies such as filtration systems, bio-secure fabrics, and energy storage. Despite the immense potential much is still not known about the physics involved with their behavior. Reports in the literature include a wide range of enhancement factors as well as explanations for the existence of enhanced flow in the first place. The platform presented here allows for the study of this enhanced flow and it gives some insights into its source. As further work

continues to elucidate on the physics of carbon nanotube transport, it is very likely that they will be the source of many amazing new technologies to come.

The world of nanopore science is currently a very exciting place. The last 20 years have seen an explosion in the amount of nanopore related research being done. The result is a wealth of new information regarding their behaviors and the creation of many new nanopore based technologies. As the fundamentals continue to be ironed out, additional progress will become ever easier. For this reason, the future of nanopore science holds enormous potential.

Bibliography

- (1) Buchsbaum, S. F.; Mitchell, N.; Martin, H.; Wiggin, M.; Marziali, A.; Coveney, P. V.; Siwy, Z.; Howorka, S. Disentangling Steric and Electrostatic Factors in Nanoscale Transport through Confined Space. *Nano Lett.* **2013**, *13*, 3890–3896.
- (2) Buchsbaum, S. F.; Nguyen, G.; Howorka, S.; Siwy, Z. S. DNA-Modified Polymer Pores Allow pH- and Voltage-Gated Control of Channel Flux. *J. Am. Chem. Soc.* **2014**, *136*, 9902–9905.
- (3) Hille, B. Ion Channel Excitable Membranes. In *Sunderland Massachusetts USA*; 2001; pp. 1–37.
- (4) Alberts, B.; Johnson, A.; Lewis, J.; Raff, M.; Roberts, K.; Walter, P. *Molecular Biology of the Cell, Fourth Edition*; 2002.
- (5) Bayley, H. Pore-Forming Proteins with Built-in Triggers and Switches. *Bioorg. Chem.* **1995**, *23*, 340–354.
- (6) Bhakdi, S.; Trantum-Jensen, J. Alpha-Toxin of Staphylococcus Aureus. *Microbiol. Rev.* **1991**, *55*, 733–751.
- (7) McGillivray, D. J.; Valincius, G.; Heinrich, F.; Robertson, J. W. F.; Vanderah, D. J.; Febo-Ayala, W.; Ignatjev, I.; Lösche, M.; Kasianowicz, J. J. Structure of Functional Staphylococcus Aureus Alpha-Hemolysin Channels in Tethered Bilayer Lipid Membranes. *Biophys. J.* **2009**, *96*, 1547–1553.
- (8) Prince, L. R.; Graham, K. J.; Connolly, J.; Anwar, S.; Ridley, R.; Sabroe, I.; Foster, S. J.; Whyte, M. K. B. Staphylococcus Aureus Induces Eosinophil Cell Death Mediated by α -Hemolysin. *PLoS One* **2012**, *7*, e31506.
- (9) Essmann, F.; Bantel, H.; Totzke, G.; Engels, I. H.; Sinha, B.; Schulze-Osthoff, K.; Jänicke, R. U. Staphylococcus Aureus Alpha-Toxin-Induced Cell Death: Predominant Necrosis despite Apoptotic Caspase Activation. *Cell Death Differ.* **2003**, *10*, 1260–1272.
- (10) HODGKIN, A.; HUXLEY, A. A Quantitative Description of Membrane Current and Its Application to Conduction and Excitation in Nerve. *Bull. Math. Biol.* **1990**, *52*, 25–71.
- (11) Doyle, D. a; Morais Cabral, J.; Pfuetzner, R. a; Kuo, a; Gulbis, J. M.; Cohen, S. L.; Chait, B. T.; MacKinnon, R. The Structure of the Potassium Channel: Molecular Basis of K⁺ Conduction and Selectivity. *Science* **1998**, *280*, 69–77.
- (12) Rajakulendran, S.; Kullmann, D. Inherited Ion Channel Disorders of the Brain. *Advances in Clinical Neuroscience and Rehabilitation*. January 2013,.
- (13) Weinreich, F.; Jentsch, T. J. Neurological Diseases Caused by Ion-Channel Mutations. *Curr. Opin. Neurobiol.* **2000**, *10*, 409–415.
- (14) Zaydman, M. a; Silva, J. R.; Cui, J. Ion Channel Associated Diseases: Overview of Molecular Mechanisms. *Chem. Rev.* **2012**, *112*, 6319–6333.
- (15) Hübner, C. a; Jentsch, T. J. Ion Channel Diseases. *Hum. Mol. Genet.* **2002**, *11*, 2435–

2445.

- (16) The Nobel Prize in Physiology or Medicine in 1991
www.nobelprize.org/nobel_prices/medicine/laureates/1991/.
- (17) Venkatesan, B. M.; Bashir, R. Nanopore Sensors for Nucleic Acid Analysis. *Nat. Nanotechnol.* **2011**, *6*, 615–624.
- (18) Howorka, S.; Cheley, S.; Bayley, H. Sequence-Specific Detection of Individual DNA Strands Using Engineered Nanopores. *Nat. Biotechnol.* **2001**, *19*, 636–639.
- (19) Ma, L.; Cockcroft, S. L. Biological Nanopores for Single-Molecule Biophysics. *ChemBioChem* **2010**, *11*, 25–34.
- (20) Dekker, C. Solid-State Nanopores. *Nat. Nanotechnol.* **2007**, *2*, 209–215.
- (21) Kowalczyk, S. W.; Blosser, T. R.; Dekker, C. Biomimetic Nanopores: Learning from and about Nature. *Trends Biotechnol.* **2011**, *29*, 607–614.
- (22) Guo, S.; Meshot, E. R.; Kuykendall, T.; Cabrini, S.; Fornasiero, F. Nanofluidic Transport through Isolated Carbon Nanotube Channels: Advances, Controversies, and Challenges. *Adv. Mater.* **2015**, n/a – n/a.
- (23) Siwy, Z. S.; Howorka, S. Engineered Voltage-Responsive Nanopores. *Chem. Soc. Rev.* **2010**, *39*, 1115–1132.
- (24) Helmholtz, H. Ueber Einige Gesetze Der Vertheilung Elektrischer Ströme in Körperlichen Leitern Mit Anwendung Auf Die Thierisch-elektrischen Versuche. *Ann. Phys.* **1853**, *January*.
- (25) Gouy, G. Sur La Constitution de La Charge Electrique a La Surface D'un Electrolyte. *Compt. Rend.* **1910**, *149*, 654.
- (26) Chapman, D. L. A Contribution to the Theory of Electrocapillarity. *Philos. Mag.* **1913**, *25*, 475–481.
- (27) Stern, O. ZUR THEORIE DER ELEKTROLYTISCHEN DOPPELSCHICHT. *Zeitschrift für Elektrochemie und Angew. Phys. Chemie* **1924**, *November*, 508–516.
- (28) Kalman, E. B. Controlling Ionic Transport for Device Design in Synthetic Nanopores, UC Irvine, 2010.
- (29) Grahame, D. The Electrical Double Layer and the Theory of Electrocapillarity. *Chem. Rev.* **1947**, 441–501.
- (30) Bockris, J. O.; Devanathan, M. A. V.; Müller, K. On the Structure of Charged Interfaces. *Proc. R. Soc. A Math. Phys. Eng. Sci.* **1963**, *274*, 55–79.
- (31) Marcus, R. A. Electron Transfer Reactions in Chemistry: Theory and Experiment. *Angew. Chemie Int. Ed. English* **1993**, *32*, 1111–1121.
- (32) Purcell, E. M. Life at Low Reynolds Number. *Am. J. Phys.* **1977**, *45*, 3.
- (33) Xue, J. M.; Zou, X. Q.; Xie, Y. B.; Wang, Y. G. Molecular Dynamics Simulations on the Ionic Current through Charged Nanopores. *J. Phys. D. Appl. Phys.* **2009**, *42*, 105308.

- (34) Cervera, J.; Schiedt, B.; Ramirez, P. A Poisson/Nernst-Planck Model for Ionic Transport through Synthetic Conical Nanopores. *Europhys. Lett.* **2005**, *71*, 35–41.
- (35) Emma, S. J. A Brief Look at ECG Sensor Technology. *Medical Design Technology*. August 2011,.
- (36) Jović, B. M.; Jović, V. D.; Dražić, D. M. Kinetics of Chloride Ion Adsorption and the Mechanism of AgCl Layer Formation on the (111), (100) and (110) Faces of Silver. *J. Electroanal. Chem.* **1995**, *399*, 197–206.
- (37) Zhang, Y.; Wang, Y.; Song, Y. Impedance Characteristics for Solid Ag/AgCl Electrode Used as Recording Electric Field Generated by Vessels in Seawater. *J. Shanghai Univ.* **2009**, *13*, 57–62.
- (38) Coulter, W. H.; Hogg, W. R. Apparatus and Method for Measuring a Dividing Particle Size of a Particulate System. US3557352 A, 1971.
- (39) Henriquez, R. R.; Ito, T.; Sun, L.; Crooks, R. M. The Resurgence of Coulter Counting for Analyzing Nanoscale Objects. *Analyst* **2004**, *129*, 478–482.
- (40) Davenport, M.; Healy, K.; Pevarnik, M.; Teslich, N.; Cabrini, S.; Morrison, A. P.; Siwy, Z. S.; Létant, S. E. The Role of Pore Geometry in Single Nanoparticle Detection. *ACS Nano* **2012**, *6*, 8366–8380.
- (41) Saleh, O. a.; Sohn, L. L. Quantitative Sensing of Nanoscale Colloids Using a Microchip Coulter Counter. *Rev. Sci. Instrum.* **2001**, *72*, 4449–4451.
- (42) DeBlois, R. W.; Bean, C. P. Counting and Sizing of Submicron Particles by the Resistive Pulse Technique. *Rev. Sci. Instrum.* **1970**, *41*, 909–916.
- (43) Pevarnik, M. A. Transport of Ions and Particles Through Single Pores of Controlled Geometry and Surface Chemistry, UC Irvine, 2012.
- (44) Kim, S. C.; Kannam, S. K.; Harrer, S.; Downton, M. T.; Moore, S.; Wagner, J. M. Geometric Dependence of the Conductance Drop in a Nanopore due to a Particle. *Phys. Rev. E* **2014**, *89*, 042702.
- (45) Vlassarev, D. M.; Golovchenko, J. A. Trapping DNA near a Solid-State Nanopore. **2012**, *103*, 352–356.
- (46) Kasianowicz, J. J.; Brandin, E.; Branton, D.; Deamer, D. W. Characterization of Individual Polynucleotide Molecules Using a Membrane Channel. *Proc. Natl. Acad. Sci. U. S. A.* **1996**, *93*, 13770–13773.
- (47) Deamer, D. W.; Branton, D. Characterization of Nucleic Acids by Nanopore Analysis. *Acc. Chem. Res.* **2002**, *35*, 817–825.
- (48) Branton, D.; Deamer, D. W.; Marziali, A.; Bayley, H.; Benner, S. a; Butler, T.; Di Ventra, M.; Garaj, S.; Hibbs, A.; Huang, X.; *et al.* The Potential and Challenges of Nanopore Sequencing. *Nat. Biotechnol.* **2008**, *26*, 1146–1153.
- (49) Wanunu, M. Nanopores: A Journey towards DNA Sequencing. *Phys. Life Rev.* **2012**, *9*, 125–158.

- (50) Manrao, E. A.; Derrington, I. M.; Laszlo, A. H.; Langford, K. W.; Hopper, M. K.; Gillgren, N.; Pavlenok, M.; Niederweis, M.; Gundlach, J. H. Reading DNA at Single-Nucleotide Resolution with a Mutant MspA Nanopore and phi29 DNA Polymerase. *Nat. Biotechnol.* **2012**, *30*, 349–353.
- (51) Technologies, O. N. MinION MkI: portable, real-time biological analyses <https://www.nanoporetech.com/products-services/minion-mki>.
- (52) Song, L.; Hobaugh, M. R.; Shustak, C.; Cheley, S.; Bayley, H.; Gouaux, J. E. Structure of Staphylococcal Alpha-Hemolysin, a Heptameric Transmembrane Pore. *Science (80-.)*. **1996**, *274*, 1859–1865.
- (53) Meller, a.; Nivon, L.; Branton, D. Voltage-Driven DNA Translocations through a Nanopore. *Phys. Rev. Lett.* **2001**, *86*, 3435–3438.
- (54) Luan, B.; Stolovitzky, G.; Martyna, G. Slowing and Controlling the Translocation of DNA in a Solid-State Nanopore. *Nanoscale* **2012**, *4*, 1068–1077.
- (55) Bayley, H. Sequencing Single Molecules of DNA. *Curr. Opin. Chem. Biol.* **2006**, *10*, 628–637.
- (56) Nivala, J.; Marks, D. B.; Akeson, M. Unfoldase-Mediated Protein Translocation through an α -Hemolysin Nanopore. *Nat. Biotechnol.* **2013**, *31*, 247–250.
- (57) Wiggin, M.; Tropini, C.; Tabard-Cossa, V.; Jetha, N. N.; Marziali, A. Nonexponential Kinetics of DNA Escape from Alpha-Hemolysin Nanopores. *Biophys. J.* **2008**, *95*, 5317–5323.
- (58) Shapovalov, G. Gating Transitions in Bacterial Ion Channels Measured at 3 S Resolution. *J. Gen. Physiol.* **2004**, *124*, 151–161.
- (59) Mitchell, N.; Howorka, S. Chemical Tags Facilitate the Sensing of Individual DNA Strands with Nanopores. *Angew. Chemie* **2008**, *120*, 5647–5650.
- (60) Mathé, J.; Aksimentiev, A.; Nelson, D. R.; Schulten, K.; Meller, A. Orientation Discrimination of Single-Stranded DNA inside the Alpha-Hemolysin Membrane Channel. *Proc. Natl. Acad. Sci. U. S. A.* **2005**, *102*, 12377–12382.
- (61) Clarke, J.; Wu, H.-C.; Jayasinghe, L.; Patel, A.; Reid, S.; Bayley, H. Continuous Base Identification for Single-Molecule Nanopore DNA Sequencing. *Nat. Nanotechnol.* **2009**, *4*, 265–270.
- (62) Meller, A.; Branton, D. Single Molecule Measurements of DNA Transport through a Nanopore. *Electrophoresis* **2002**, *23*, 2583–2591.
- (63) Matysiak, S.; Montesi, A.; Pasquali, M.; Kolomeisky, A. B.; Clementi, C. Dynamics of Polymer Translocation through Nanopores: Theory Meets Experiment. *Phys. Rev. Lett.* **2006**, *96*, 1–4.
- (64) Becquerel, E. La Lumiere; Ses Causes et Ses Effets. *Firmin Didot* **1867**, *1*.
- (65) Austin, R. H.; Beeson, K. W.; Eisenstein, L.; Frauenfelder, H.; Gunsalus, I. C. Dynamics of Ligand Binding to Myoglobin. *Biochemistry* **1975**, *14*, 5355–5373.

- (66) Gardiner, C. Handbook of Stochastic Methods for Physics, Chemistry and the Natural Sciences. *Applied Optics*, 1986.
- (67) Redner, S.; Dorfman, J. R. *A Guide to First-Passage Processes*; 2002; Vol. 70.
- (68) Kalé, L.; Skeel, R.; Bhandarkar, M.; Brunner, R.; Gursoy, A.; Krawetz, N.; Phillips, J.; Shinozaki, A.; Varadarajan, K.; Schulten, K. NAMD2: Greater Scalability for Parallel Molecular Dynamics. *J. Comput. Phys.* **1999**, *151*, 283–312.
- (69) Jorgensen, W. L.; Chandrasekhar, J.; Madura, J. D.; Impey, R. W.; Klein, M. L. Comparison of Simple Potential Functions for Simulating Liquid Water. *J. Chem. Phys.* **1983**, *79*, 926.
- (70) Pearlman, D. A.; Case, D. A.; Caldwell, J. W.; Ross, W. S.; Cheatham, T. E.; DeBolt, S.; Ferguson, D.; Seibel, G.; Kollman, P. A. AMBER, a Package of Computer Programs for Applying Molecular Mechanics, Normal Mode Analysis, Molecular Dynamics and Free Energy Calculations to Simulate the Structural and Energetic Properties of Molecules. *Comput. Phys. Commun.* **1995**, *91*, 1–41.
- (71) Arnott, S.; Smith, P. J. C.; Chandrasekharan, R. *CRC Handbook of Biochemistry and Molecular Biology: Nucleic Acids*; CRC Press: Cleveland, OH, 1972.
- (72) Humphrey, W.; Dalke, A.; Schulten, K. VMD: Visual Molecular Dynamics. *J. Mol. Graph.* **1996**, *14*, 33–38.
- (73) Guex, N.; Peitsch, M. C. SWISS-MODEL and the Swiss-PdbViewer: An Environment for Comparative Protein Modeling. *Electrophoresis* **1997**, *18*, 2714–2723.
- (74) Feller, S. E.; Mackerell, A. D. J. An Improved Empirical Potential Energy Function for Molecular Simulations of Phospholipids. *J. Phys. Chem. B* **2000**, *104*, 7510–7515.
- (75) Batcho, P. F.; Case, D. a.; Schlick, T. Optimized Particle-Mesh Ewald/multiple-Time Step Integration for Molecular Dynamics Simulations. *J. Chem. Phys.* **2001**, *115*, 4003–4018.
- (76) Brunger, A. T. *X-PLOR Version 3.1: A System for X-Ray Crystallography and NMR*; 1992.
- (77) Martyna, G. J.; Tobias, D. J.; Klein, M. L. Constant Pressure Molecular Dynamics Algorithms. *J. Chem. Phys.* **1994**, *101*, 4177.
- (78) Markovitsi, D.; Gustavsson, T.; Banyasz, A. Absorption of UV Radiation by DNA: Spatial and Temporal Features. *Mutat. Res.* **2010**, *704*, 21–28.
- (79) Schink, S.; Renner, S.; Alim, K.; Arnaut, V.; Simmel, F. C.; Gerland, U. Quantitative Analysis of the Nanopore Translocation Dynamics of Simple Structured Polynucleotides. *Biophys. J.* **2012**, *102*, 85–95.
- (80) Chuang, J.; Kantor, Y.; Kardar, M. Anomalous Dynamics of Translocation. *Phys. Rev. E - Stat. Nonlinear, Soft Matter Phys.* **2002**, *65*, 1–8.
- (81) Lathrop, D. K.; Ervin, E. N.; Barrall, G. a.; Keehan, M. G.; Kawano, R.; Krupka, M. a.; White, H. S.; Hibbs, A. H. Monitoring the Escape of DNA from a Nanopore Using an Alternating Current Signal. *J. Am. Chem. Soc.* **2010**, *132*, 1878–1885.

- (82) Luan, B.; Aksimentiev, A. Effective Screening of the DNA Charge in a Nanopore. *Phys. Rev. E - Stat. Nonlinear, Soft Matter Phys.* **2008**, *78*, 021912.
- (83) Firnkes, M.; Pedone, D.; Knezevic, J.; Döblinger, M.; Rant, U. Electrically Facilitated Translocations of Proteins through Silicon Nitride Nanopores: Conjoint and Competitive Action of Diffusion, Electrophoresis, and Electroosmosis. *Nano Lett.* **2010**, *10*, 2162–2167.
- (84) Yameen, B.; Ali, M.; Neumann, R.; Ensinger, W.; Knoll, W.; Azzaroni, O. Single Conical Nanopores Displaying pH-Tunable Rectifying Characteristics. Manipulating Ionic Transport with Zwitterionic Polymer Brushes. *J. Am. Chem. Soc.* **2009**, *131*, 2070–2071.
- (85) Yameen, B.; Ali, M.; Neumann, R.; Ensinger, W.; Knoll, W.; Azzaroni, O. Synthetic Proton-Gated Ion Channels via Single Solid-State Nanochannels Modified with Responsive Polymer Brushes. *Nano Lett.* **2009**, *9*, 2788–2793.
- (86) Harrell, C. C.; Kohli, P.; Siwy, Z.; Martin, C. R. DNA-Nanotube Artificial Ion Channels. *J. Am. Chem. Soc.* **2004**, *126*, 15646–15647.
- (87) Spohr, R. *Ion Tracks and Microtechnology: Principles and Applications*; Friedr. Vieweg & Sohn Verlagsgesellschaft mbH: Braunschweig, 1990.
- (88) Fleischer, R. R. L.; Price, P. B.; Walker, R. M. *Nuclear Tracks in Solids: Principles and Applications*; University of California Press: Berkely and Los Angeles, 1975.
- (89) Adla, A.; Fuess, H.; Trautmann, C. Characterization of Heavy Ion Tracks in Polymers by Transmission Electron Microscopy. *J. Polym. Sci. Part B Polym. Phys.* **2003**, *41*, 2892–2901.
- (90) Apel, P. Y.; Korchev, Y. E.; Siwy, Z.; Spohr, R.; Yoshida, M. Diode-like Single-Ion Track Membrane Prepared by Electro-Stopping. *Nucl. Instruments Methods Phys. Res. Sect. B Beam Interact. with Mater. Atoms* **2001**, *184*, 337–346.
- (91) Crawford, W. T.; DeSorbo, W.; Humphrey Jr., J. S. Enhancement of Track Etching Rates in Charged Particle-Irradiated Plastics by a Photo-Oxidation Effect. *Nature* **1968**, *220*, 1313–1314.
- (92) Bean, C. P.; Desorbo, W. *Porous Bodies and Method of Making*, 1973.
- (93) Siwy, Z.; Apel, P.; Dobrev, D.; Neumann, R.; Spohr, R.; Trautmann, C.; Voss, K. Ion Transport through Asymmetric Nanopores Prepared by Ion Track Etching. *Nucl. Instruments Methods Phys. Res. Sect. B Beam Interact. with Mater. Atoms* **2003**, *208*, 143–148.
- (94) Siwy, Z.; Fuliński, A. Origin of $\langle 1 + \alpha^2 \rangle$ Noise in Membrane Channel Currents. *Phys. Rev. Lett.* **2002**, *89*, 158101.
- (95) Pasternak, C. A.; Alder, G. M.; Apel, P. Y.; Bashford, C. L.; Edmonds, D. T.; Korchev, Y. E.; Lev, A. A.; Lowe, G.; Milovanovich, M.; Pitt, C. W.; *et al.* Nuclear Track-Etched Filters as Model Pores for Biological-Membranes. *Radiat. Meas.* **1995**, *25*, 675–683.

- (96) Xue, J.; Xie, Y.; Yan, Y.; Ke, J.; Wang, Y. Surface Charge Density of the Track-Etched Nanopores in Polyethylene Terephthalate Foils. *Biomicrofluidics* **2009**, *3*, 22408.
- (97) Sober, H. A. *Handbook of Biochemistry*; CRC Press: Cleveland, Ohio, 1968.
- (98) Hermanson, G. T. *Bioconjugate Techniques*; 2008.
- (99) Siwy, Z. S.; Martin, C. R. Tuning Ion Current Rectification in Synthetic Nanotubes. In *Controlled nanoscale motion*; 2007; pp. 349–365.
- (100) Romano, J. D. The Conical Resistor Conundrum: A Potential Solution. *Am. J. Phys.* **1996**, *64*, 1150.
- (101) Powell, M. R. Voltage Responsive Transport Properties of Ion Current through Singles Nanopores, UC Irvine, 2010.
- (102) Aksimentiev, A.; Schulten, K. Imaging α -Hemolysin with Molecular Dynamics: Ionic Conductance, Osmotic Permeability, and the Electrostatic Potential Map. *Biophys. J.* **2005**, *88*, 3745–3761.
- (103) Cervera, J.; Schiedt, B.; Neumann, R.; Mafé, S.; Ramírez, P. Ionic Conduction, Rectification, and Selectivity in Single Conical Nanopores. *J. Chem. Phys.* **2006**, *124*, 104706.
- (104) Siwy, Z.; Fuliński, A. A Nanodevice for Rectification and Pumping Ions. *Am. J. Phys.* **2004**, *72*, 567.
- (105) Siwy, Z.; Fuliński, a. Fabrication of a Synthetic Nanopore Ion Pump. *Phys. Rev. Lett.* **2002**, *89*, 198103.
- (106) Nguyen, G.; Vlassiouk, I.; Siwy, Z. S. Comparison of Bipolar and Unipolar Ionic Diodes. *Nanotechnology* **2010**, *21*, 265301.
- (107) Vlassiouk, I.; Siwy, Z. S. Nanofluidic Diode. *Nano Lett.* **2007**, *7*, 552–556.
- (108) Constantin, D.; Siwy, Z. S. Poisson-Nernst-Planck Model of Ion Current Rectification through a Nanofluidic Diode. *Phys. Rev. E - Stat. Nonlinear, Soft Matter Phys.* **2007**, *76*, 1–10.
- (109) Davenport, M. W. . Synthetic Nanopores : Biological Analogues and Nanofluidic Devices, UC Irvine, 2013.
- (110) Verdolino, V.; Cammi, R.; Munk, B. H.; Schlegel, H. B. Calculation of P K a Values of Nucleobases and the Guanine Oxidation Products Guanidinohydantoin and Spiroiminodihydantoin Using Density Functional Theory and a Polarizable Continuum Model. **2008**, 16860–16873.
- (111) Dolinnaya, N. G.; Fresco, J. R. Single-Stranded Nucleic Acid Helical Secondary Structure Stabilized by Ionic Bonds: d(A(+)-G)₁₀. *Proc. Natl. Acad. Sci. U. S. A.* **1992**, *89*, 9242–9246.
- (112) Blackburn, G. M.; Gait, M. J.; Loakes, D.; Williams, D. M. *Nucleic Acids in Chemistry and Biology*; Cambridge, U.K., 2006.

- (113) Robinson, H.; van der Marel, G. a; van Boom, J. H.; Wang, a H. Unusual DNA Conformation at Low pH Revealed by NMR: Parallel-Stranded DNA Duplex with Homo Base Pairs. *Biochemistry* **1992**, *31*, 10510–10517.
- (114) Kaiser, W.; Rant, U. Conformations of End-Tethered DNA Molecules on Gold Surfaces: Influences of Applied Electric Potential, Electrolyte Screening, and Temperature. *J. Am. Chem. Soc.* **2010**, *132*, 7935–7945.
- (115) Skolnick, J.; Fixman, M. Electrostatic Persistence Length of a Wormlike Polyelectrolyte. *Macromolecules* **2010**, *10*, 944–948.
- (116) Tinland, B.; Pluen, A.; Sturm, J.; Weill, G. Persistence Length of Single-Stranded DNA. *Macromolecules* **1997**, *30*, 5763–5765.
- (117) Nguyen, G. Synthetic Analogue of Voltage-Gated Channels. **2013**.
- (118) Toimil-Molares, M. E. Characterization and Properties of Micro- and Nanowires of Controlled Size, Composition, and Geometry Fabricated by Electrodeposition and Ion-Track Technology. *Beilstein J. Nanotechnol.* **2012**, *3*, 860–883.
- (119) Smeets, R. M. M. R. M. M.; Keyser, U. F. U. F.; Krapf, D.; Wu, M. Y. M. Y.; Nynke, H.; Dekker, C.; Dekker, N. H.; Dekker, C. Salt-Dependence of Ion Transport and DNA Translocation through Solid-State Nanopores. *Nano Lett.* **2006**, *6*, 89–95.
- (120) Nguyen, G.; Howorka, S.; Siwy, Z. S. DNA Strands Attached inside Single Conical Nanopores: Ionic Pore Characteristics and Insight into DNA Biophysics. *J Membr. Biol.* **2011**, *239*, 105–113.
- (121) Pietschmann, J.-F.; Wolfram, M.-T.; Burger, M.; Trautmann, C.; Nguyen, G.; Pevarnik, M.; Bayer, V.; Siwy, Z. Rectification Properties of Conically Shaped Nanopores: Consequences of Miniaturization. *Phys. Chem. Chem. Phys.* **2013**, *15*, 16917–16926.
- (122) Vlasiouk, I.; Smimov, S.; Siwy, Z. Nanofluidic Ionic Diodes. Comparison of Analytical and Numerical Solutions. *ACS Nano* **2008**, *2*, 1589–1602.
- (123) Yang, J.; Ellinor, P. T.; Sather, W. a; Zhang, J. F.; Tsien, R. W. Molecular Determinants of Ca²⁺ Selectivity and Ion Permeation in L-Type Ca²⁺ Channels. *Nature* **1993**, *366*, 158–161.
- (124) Boehm, H. The First Observation of Carbon Nanotubes. *Carbon N. Y.* **1997**, *35*, 581–584.
- (125) Monthieux, M.; Kuznetsov, V. L. Who Should Be given the Credit for the Discovery of Carbon Nanotubes? *Carbon N. Y.* **2006**, *44*, 1621–1623.
- (126) Oberlin, a.; Endo, M.; Koyama, T. Filamentous Growth of Carbon through Benzene Decomposition. *J. Cryst. Growth* **1976**, *32*, 335–349.
- (127) Iijima, S. Helical Microtubules of Graphitic Carbon. *Nature* **1991**, *354*, 56–58.
- (128) Corry, B. Designing Carbon Nanotube Membranes for Efficient Water Desalination. *J. Phys. Chem. B* **2008**, *112*, 1427–1434.
- (129) Upadhyayula, V. K. K.; Deng, S.; Mitchell, M. C.; Smith, G. B. Application of Carbon

- Nanotube Technology for Removal of Contaminants in Drinking Water: A Review. *Sci. Total Environ.* **2009**, *408*, 1–13.
- (130) Das, R.; Ali, M. E.; Hamid, S. B. A.; Ramakrishna, S.; Chowdhury, Z. Z. Carbon Nanotube Membranes for Water Purification: A Bright Future in Water Desalination. *Desalination* **2014**, *336*, 97–109.
- (131) Coleman, J. N.; Khan, U.; Blau, W. J.; Gun'ko, Y. K. Small but Strong: A Review of the Mechanical Properties of Carbon Nanotube-Polymer Composites. *Carbon N. Y.* **2006**, *44*, 1624–1652.
- (132) Koziol, K.; Vilatela, J.; Moisala, A.; Motta, M.; Cunniff, P.; Sennett, M.; Windle, A. High-Performance Carbon Nanotube Fiber. *Science* **2007**, *318*, 1892–1895.
- (133) Zhang, M.; Fang, S.; Zakhidov, A. A.; Lee, S. B.; Aliev, A. E.; Williams, C. D.; Atkinson, K. R.; Baughman, R. H. Strong, Transparent, Multifunctional, Carbon Nanotube Sheets. *Science* **2005**, *309*, 1215–1219.
- (134) Raychowdhury, A.; Mukhopadhyay, S.; Roy, K. A Circuit-Compatible Model of Ballistic Carbon Nanotube Field-Effect Transistors. *IEEE Trans. Comput. Des. Integr. Circuits Syst.* **2004**, *23*, 1411–1420.
- (135) Franklin, A. D.; Luisier, M.; Han, S. J.; Tulevski, G.; Breslin, C. M.; Gignac, L.; Lundstrom, M. S.; Haensch, W. Sub-10 Nm Carbon Nanotube Transistor. *Nano Lett.* **2012**, *12*, 758–762.
- (136) Allen, B. L.; Kichambare, P. D.; Star, A. Carbon Nanotube Field-Effect-Transistor-Based Biosensors. *Adv. Mater.* **2007**, *19*, 1439–1451.
- (137) Liu, Z.; Tabakman, S. M.; Chen, Z.; Dai, H. Preparation of Carbon Nanotube Bioconjugates for Biomedical Applications. *Nat. Protoc.* **2009**, *4*, 1372–1382.
- (138) Yang, W. R.; Thordarson, P.; Gooding, J. J.; Ringer, S. P.; Braet, F. Carbon Nanotubes for Biological and Biomedical Applications. *Nanotechnology* **2007**, *18*, 412001.
- (139) Sinha, N.; Ma, J.; Yeow, J. T. W. Carbon Nanotube-Based Sensors. *J. Nanosci. Nanotechnol.* **2006**, *6*, 573–590.
- (140) Wang, X.; Li, Q.; Xie, J.; Jin, Z.; Wang, J.; Li, Y.; Jiang, K.; Fan, S. Fabrication of Ultralong and Electrically Uniform Single-Walled Carbon Nanotubes on Clean Substrates. *Nano Lett.* **2009**, *9*, 3137–3141.
- (141) A, B.; Hummer, G.; Rasaiah, J. C.; Noworyta, J. P. Water Conduction through the Hydrophobic Channel of a Carbon Nanotube. **2001**, *414*, 188–190.
- (142) Pascal, T. a; Goddard, W. a; Jung, Y. Entropy and the Driving Force for the Filling of Carbon Nanotubes with Water. *Proc. Natl. Acad. Sci. U. S. A.* **2011**, *108*, 11794–11798.
- (143) Fornasiero, F.; Park, H. G.; Holt, J. K.; Stadermann, M.; Grigoropoulos, C. P.; Noy, A.; Bakajin, O. Ion Exclusion by Sub-2-Nm Carbon Nanotube Pores. *Proc. Natl. Acad. Sci. U. S. A.* **2008**, *105*, 17250–17255.
- (144) Majumder, M.; Chopra, N.; Hinds, B. J. Effect of Tip Functionalization on Transport

- through Vertically Oriented Carbon Nanotube Membranes. *J. Am. Chem. Soc.* **2005**, *127*, 9062–9070.
- (145) Holt, J. K.; Park, H. G.; Wang, Y.; Stadermann, M.; Artyukhin, A. B.; Grigoropoulos, C. P.; Noy, A.; Bakajin, O. Fast Mass Transport Through Sub-2-Nanometer Carbon Nanotubes. *Science (80-.)*. **2006**, *312*, 1034–1038.
- (146) Majumder, M.; Chopra, N.; Andrews, R.; Hinds, B. J. Enhanced Flow in Carbon Nanotubes. *Nature* **2005**, *438*, 43–44.
- (147) Dellago, C.; Naor, M. M.; Hummer, G. Proton Transport through Water-Filled Carbon Nanotubes. *Phys. Rev. Lett.* **2003**, *90*, 105902.
- (148) Gao, H.; Kong, Y.; Cui, D.; Ozkan, C. S. Spontaneous Insertion of DNA Oligonucleotides into Carbon Nanotubes. *Nano Lett.* **2003**, *3*, 471–473.
- (149) Pang, P.; He, J.; Park, J. H.; Krstić, P. S.; Lindsay, S. Origin of Giant Ionic Currents in Carbon Nanotube Channels. *ACS Nano* **2011**, *5*, 7277–7283.
- (150) Park, J. H.; He, J.; Gyrfas, B.; Lindsay, S.; Krstić, P. S. DNA Translocating through a Carbon Nanotube Can Increase Ionic Current. *Nanotechnology* **2012**, *23*, 455107.
- (151) Lee, C. Y.; Choi, W.; Han, J.-H.; Strano, M. S. Coherence Resonance in a Single-Walled Carbon Nanotube Ion Channel. *Science* **2010**, *329*, 1320–1324.
- (152) Choi, W.; Ulissi, Z. W.; Shimizu, S. F. E.; Bellisario, D. O.; Ellison, M. D.; Strano, M. S. Diameter-Dependent Ion Transport through the Interior of Isolated Single-Walled Carbon Nanotubes. *Nat. Commun.* **2013**, *4*, 1–8.
- (153) Cao, D.; Pang, P.; He, J.; Luo, T.; Park, J. H.; Krstic, P.; Nuckolls, C.; Tang, J.; Lindsay, S. Electronic Sensitivity of Carbon Nanotubes to Internal Water Wetting. *ACS Nano* **2011**, *5*, 3113–3119.
- (154) Balasubramanian, K.; Burghard, M. Chemically Functionalized Carbon Nanotubes. *Small* **2005**, *1*, 180–192.
- (155) Odom, T. W.; Huang, J. L.; Kim, P.; Lieber, C. M. Atomic Structure and Electronic Properties of Single-Walled Carbon Nanotubes. *Nature* **1998**, *391*, 62–64.
- (156) Myers, T. G. Why Are Slip Lengths so Large in Carbon Nanotubes? *Microfluid. Nanofluidics* **2011**, *10*, 1141–1145.
- (157) He, Z.; Zhou, J.; Lu, X.; Corry, B. Ice-like Water Structure in Carbon Nanotube (8,8) Induces Cationic Hydration Enhancement. *J. Phys. Chem. C* **2013**, *117*, 11412–11420.
- (158) Winarto; Takaiwa, D.; Yamamoto, E.; Yasuoka, K. Structures of Water Molecules in Carbon Nanotubes under Electric Fields. *J. Chem. Phys.* **2015**, *142*, 124701.
- (159) Dougherty, D. a. The Cation- π Interaction. *Acc. Chem. Res.* **2013**, *46*, 885–893.
- (160) Gygi, F. Qbox, a Scalable Implementation of First Principles Molecular Dynamics.
- (161) Perdew, J.; Burke, K.; Ernzerhof, M. Generalized Gradient Approximation Made Simple. *Phys. Rev. Lett.* **1996**, *77*, 3865–3868.

- (162) Vanderbilt, D. Optimally Smooth Norm-Conserving Pseudopotentials. *Phys. Rev. B* **1985**, *32*, 8412–8415.
- (163) Shao, Q.; Huang, L. L.; Zhou, J.; Lu, L. H.; Zhang, L. Z.; Lu, X. H.; Jiang, S. Y.; Gubbins, K. E.; Shen, W. F. Molecular Simulation Study of Temperature Effect on Ionic Hydration in Carbon Nanotubes. *Phys. Chem. Chem. Phys.* **2008**, *10*, 1896–1906.
- (164) Jorgensen, W. L.; Maxwell, D. S.; Tirado-Rives, J. Development and Testing of the OPLS All-Atom Force Field on Conformational Energetics and Properties of Organic Liquids. *J. Am. Chem. Soc.* **1996**, *118*, 11225–11236.
- (165) Berendsen, H. J. C.; Grigera, J. R.; Straatsma, T. P. The Missing Term in Effective Pair Potentials. *J. Phys. Chem.* **1987**, *91*, 6269–6271.
- (166) Lamoureux, G.; Harder, E.; Vorobyov, I. V.; Roux, B.; MacKerell, A. D. A Polarizable Model of Water for Molecular Dynamics Simulations of Biomolecules. *Chem. Phys. Lett.* **2006**, *418*, 245–249.
- (167) Yu, H.; Whitfield, T. W.; Harder, E.; Lamoureux, G.; Vorobyov, I.; Anisimov, V. M.; MacKerell, A. D.; Roux, B. Simulating Monovalent and Divalent Ions in Aqueous Solution Using a Drude Polarizable Force Field. *J. Chem. Theory Comput.* **2010**, *6*, 774–786.
- (168) Orabi, E. A.; Lamoureux, G. Cation- π and π - π Interactions in Aqueous Solution Studied Using Polarizable Potential Models. *J. Chem. Theory Comput.* **2012**, *8*, 182–193.
- (169) Dresselhaus, M. S.; Dresselhaus, G.; Saito, R.; Jorio, A. Raman Spectroscopy of Carbon Nanotubes. *Phys. Rep.* **2005**, *409*, 47–99.
- (170) Shimizu, S.; Ellison, M.; Aziz, K.; Wang, Q. H.; Ulissi, Z.; Gunther, Z.; Bellisario, D.; Strano, M. Stochastic Pore Blocking and Gating in PDMS–Glass Nanopores from Vapor–Liquid Phase Transitions. *J. Phys. Chem. C* **2013**, *117*, 9641–9651.
- (171) Lee, C.; Joly, L.; Siria, A.; Biance, A. Large Apparent Electric Size of Solid-State Nanopores Due to Spatially Extended Surface Conduction. **2012**.
- (172) Lander, E. S. Initial Impact of the Sequencing of the Human Genome. *Nature* **2011**, *470*, 187–197.
- (173) Collins, F. S.; McKusick, V. a. Implications of the Human Genome Project for Medical Science. *JAMA* **2001**, *285*, 540–544.
- (174) Howorka, S.; Siwy, Z. Nanopore Analytics: Sensing of Single Molecules. *Chem. Soc. Rev.* **2009**, *38*, 2360–2384.